

¹ **Searches for Supersymmetry using the α_T**
² **variable with the CMS detector at the LHC**

³ Darren Burton

⁴ Imperial College London
⁵ Department of Physics

⁶ A thesis submitted to Imperial College London
⁷ for the degree of Doctor of Philosophy

Abstract

10

Declaration

11

I, the author of this thesis, declare that the work presented within this
document to be my own. The work presented in Chapters 3.4.1, 4 and 5
is a result of the authors own work or that of which I have been a major
contributor unless explicitly stated otherwise, and is carried out within the
context of the Imperial College London and CERN SUSY groups, itself a
subsection of the greater CMS collaboration. All figures and studies taken
from external sources are referenced appropriately throughout this document.

18

Darren Burton

19

Acknowledgements

20

Of the many people who deserve thanks, some are particularly prominent....

Preface

Contents

23	List of Figures	viii
24	List of Tables	xii
25	1. Introduction	2
26	2. A Theoretical Overview	5
27	2.1. The Standard Model	5
28	2.1.1. Gauge Symmetries of the SM	7
29	2.1.2. The Electroweak Sector and Electroweak Symmetry Breaking	9
30	2.2. Motivation for Physics Beyond the Standard Model	13
31	2.3. Supersymmetry Overview	15
32	2.3.1. R-Parity	16
33	2.4. Experimental signatures of SUSY at the LHC	17
34	2.4.1. Simplified Models	18
35	3. The LHC and the CMS Detector	20
36	3.1. The LHC	20
37	3.2. The CMS detector	23
38	3.2.1. Detector Subsystems	23
39	3.2.2. Tracker	24
40	3.2.3. Electromagnetic Calorimeter	25
41	3.2.4. Hadronic Calorimeter	26
42	3.2.5. Muon Systems	28
43	3.3. Event Reconstruction and Object Definition	28
44	3.3.1. Jets	28
45	3.3.2. B-tagging	30
46	3.4. Triggering System	32
47	3.4.1. The Level-1 Trigger	34

48	3.4.2. L1 Trigger Jet Algorithm	35
49	3.4.3. Measuring L1 Jet Trigger Efficiencies	36
50	3.4.4. Effects of the L1 Jet Seed	38
51	3.4.5. Robustness of L1 Jet Performance against Pile-up	41
52	3.4.6. Summary	43
53	4. SUSY searches in Hadronic Final States	45
54	4.1. An introduction to the α_T search	46
55	4.1.1. The α_T variable	48
56	4.2. Search Strategy	50
57	4.2.1. Physics Objects	53
58	4.2.2. Event Selection	55
59	4.2.3. Control Sample Definition	58
60	4.2.4. Estimating the QCD background multi-jet background	65
61	4.3. Trigger Strategy	67
62	4.4. A method to determine MC yields with higher statistical precision	69
63	4.5. Measuring MC normalisation factors via H_T sidebands	69
64	4.6. Systematic Uncertainties on Transfer Factors	69
65	4.7. Searches for Natural SUSY with B-tag templates.	69
66	5. Results	70
67	5.1. Statistical Interpretation	70
68	5.2. Interpretation in Simplified Signal Models	70
69	A. Miscellaneous	71
70	A.1. Noise Filters	71
71	A.2. Primary Vertices	72
72	B. L1 Jets	73
73	B.1. Jet matching efficiencies	73
74	B.2. Leading Jet Energy Resolution	74
75	B.3. Resolution for Energy Sum Quantities	77
76	C. Additional material on background estimation methods	82
77	C.1. Determination of k_{QCD}	82
78	Bibliography	84

⁷⁹ List of Figures

⁸⁰ 2.1.	One loop quantum corrections to the Higgs squared mass parameter m_h^2 due to a fermion.	⁸¹ 14
⁸² 2.2.	Two example simplified model decay chains.	⁸³ 19
⁸³ 3.1.	A top down layout of the LHC, with the position of the four main detectors labelled.	⁸⁴ 21
⁸⁵ 3.2.	The total integrated luminosity delivered to and collected by Compact Muon Solenoid (CMS) during the 2012 8 TeV pp runs	⁸⁶ 22
⁸⁷ 3.3.	A pictorial depiction of the CMS detector.	⁸⁸ 24
⁸⁸ 3.4.	Illustration of the CMS Electromagnetic CALorimeter (ECAL).	⁸⁹ 26
⁸⁹ 3.5.	Schematic of the CMS Hadronic CALorimeter (HCAL).	⁹⁰ 27
⁹⁰ 3.6.	Combined Secondary Vertex (CSV) algorithm discriminator values in enriched $t\bar{t}$ and inclusive multi jet samples	⁹¹ 31
⁹² 3.7.	Data/MC b-tag scale factors derived using the Combined Secondary Vertex Medium Working Point (CSVM) tagger.	⁹³ 32
⁹⁴ 3.8.	Data/MC mis-tag scale factors derived using the CSVM tagger.	⁹⁵ 33
⁹⁵ 3.9.	The CMS Level 1 Trigger (L1) Trigger system.	⁹⁶ 34
⁹⁶ 3.10.	Illustration of the Level-1 jet finding algorithm.	⁹⁷ 36
⁹⁷ 3.11.	L1 jet efficiency turn-on curves as a function of the offline CaloJet and PFJet E_T	⁹⁸ 38
⁹⁹ 3.12.	L1 jet efficiency turn-on curves as a function of the offline CaloJet E_T for the 2012 run period B and C.	¹⁰⁰ 39

101	3.13. Trigger cross section for the L1HTT150 trigger path.	40
102	3.14. L1 H_T efficiency turn-on curves as a function of the offline CaloJet H_T	41
103	3.15. L1 jet efficiency turn-on curves as a function of the leading offline E_T Calo (left) and PF (right) jet, for low, medium and high pile-up conditions.	42
105	3.16. Fit values from an Exponentially Modified Gaussian (EMG) function fitted to the resolution plots of leading Calo jet E_T measured as a function of $\frac{(L1\ E_T - Offline\ E_T)}{Offline\ E_T}$ for low, medium and high pile-up conditions.	43
108	3.17. Fit values from an EMG function fitted to the resolution plots of leading PF jet E_T measured as a function of $\frac{(L1\ E_T - Offline\ E_T)}{Offline\ E_T}$ for low, medium and high pile-up conditions.	44
111	4.1. Reconstructed offline H_T for 11.7fb^{-1} of data after a basic pre-selection.	48
112	4.2. The event topologies of background QCD dijet events (right) and a generic SUperSYmmetry (SUSY) signature with genuine Z_T (left).	48
114	4.3. The α_T distributions for the low 2-3 (left) and high ≥ 4 (right) jet multiplicities after a full analysis selection and shown for $H_T > 375$	50
116	4.4. Pictorial depiction of the analysis strategy employed by the α_T search to increase sensitivity to a wide spectra of SUSY models.	52
118	4.5. Data/MC comparisons of key variables for the hadronic signal region.	58
119	4.6. Data/MC comparisons of key variables for the $\mu + \text{jets}$ selection.	61
120	4.7. Data/MC comparisons of key variables for the $\mu\mu + \text{jets}$ selection.	63
121	4.8. Data/MC comparisons of key variables for the $\gamma + \text{jets}$ selection.	64
122	4.9. QCD sideband regions, used for determination of k_{QCD}	66
123	B.1. Leading jet matching efficiency as a function of the offline CaloJet E_T	73
124	B.2. Resolution plots of the leading offline Calo E_T measured as a function of $\frac{(L1\ E_T - Offline\ E_T)}{Offline\ E_T}$ for low (a), medium (b) and high (c) pile-up conditions.	75
126	B.3. Resolution plots of the leading off-line PF E_T measured as a function of $\frac{(L1\ E_T - Offline\ E_T)}{Offline\ E_T}$ for low (a), medium (b) and high (c) pile-up conditions.	77

128	B.4. $\sum E_T$ resolution parameters in bins of Calo $\sum E_T$ measured for the defined low, medium and high pile up conditions.	78
130	B.5. $\sum E_T$ resolution parameters in bins of PF $\sum E_T$ measured for the defined low, medium and high pile up conditions.	78
132	B.6. \cancel{E}_T resolution parameters in bins of Calo \cancel{E}_T measured for the defined low, medium and high pile up conditions.	79
134	B.7. \cancel{E}_T resolution parameters in bins of PF \cancel{E}_T measured for the defined low, medium and high pile up conditions.	79
136	B.8. H_T resolution parameters in bins of Calo H_T measured for the defined low, medium and high pile up conditions.	80
138	B.9. H_T resolution parameters in bins of PF H_T measured for the defined low, medium and high pile up conditions.	80
140	B.10. \cancel{H}_T resolution parameters in bins of Calo \cancel{H}_T measured for the defined low, medium and high pile up conditions.	81
142	B.11. \cancel{H}_T resolution parameters in bins of PF \cancel{H}_T measured for the defined low, medium and high pile up conditions.	81
144	C.1. $R_{\alpha_T}(H_T)$ and exponential fits for each of the data sideband regions. Fit is conducted between the H_T region $275 < H_T < 575$	82
145		

¹⁴⁶ List of Tables

¹⁴⁷	2.1. The fundamental particles of the Standard Model (SM), with spin, charge and mass displayed.	6
¹⁴⁸		
¹⁴⁹	3.1. Results of a cumulative EMG function fit to the turn-on curves for L1 single jet triggers in 2012 Run Period C.	38
¹⁵⁰		
¹⁵¹	3.2. Results of a cumulative EMG function fit to the turn-on curves for L1 single jet triggers in the 2012 run period B and C.	39
¹⁵²		
¹⁵³	3.3. Results of a cumulative EMG function fit to the turn-on curves for H_T in 2012 run period B and C.	40
¹⁵⁴		
¹⁵⁵	3.4. Results of a cumulative EMG function fit to the efficiency turn-on curves for L1 single jet triggers in the 2012 run period C, for low,medium and high pile-up conditions.	41
¹⁵⁶		
¹⁵⁷		
¹⁵⁸	3.5. Results of a cumulative EMG function fit to the efficiency turn-on curves for Level-1 single jet triggers in the 2012 run period C, for low,medium and high pile-up conditions.	42
¹⁵⁹		
¹⁶⁰		
¹⁶¹	4.1. A summary of the Simplified Model Spectra (SMS) models interpreted in this analysis, involving both direct (D) and gluino-induced (G) production of squarks and their decays.	46
¹⁶²		
¹⁶³		
¹⁶⁴	4.2. Jet Identification criteria for the “loose” CaloJet ID used with the analysis.	53
¹⁶⁵		
¹⁶⁶	4.3. Muon Identification criteria used within the analysis for selection/veto purposes in the muon control/signal selections.	54
¹⁶⁷		
¹⁶⁸	4.4. Photon Identification criteria used within the analysis for selection/veto purposes in the $\gamma +$ jets control/signal selections.	54

169	4.5. Electron Identification criteria used within the analysis for veto purposes.	55
170	4.6. Jet thresholds used in the three H_T regions of the analysis.	56
171	4.7. Best fit values for the parameters k_{QCD} obtained from sideband regions	
172	B,C ₁ ,C ₂ ,C ₃	67
173	4.8. Measured efficiencies of the H_T and α_T legs of the HT and HT_alphaT	
174	triggers in independent analysis bins.	68
175	B.1. Results of a cumulative EMG function fit to the turn-on curves for the	
176	matching efficiency of the leading jet in an event to a Level-1 jet in run	
177	2012C and 2012B data.	74

178 Acronyms

179	ALICE	A Large Ion Collider Experiment
180	ATLAS	A Toroidal LHC ApparatuS
181	APD	Avalanche Photo-Diodes
182	BSM	Beyond Standard Model
183	CERN	European Organization for Nuclear Research
184	CMS	Compact Muon Solenoid
185	CMSSM	Compressed Minimal SuperSymmetric Model
186	CSC	Cathode Stripe Chamber
187	CSV	Combined Secondary Vertex
188	CSVM	Combined Secondary Vertex Medium Working Point
189	DT	Drift Tube
190	ECAL	Electromagnetic CALorimeter
191	EB	Electromagnetic CALorimeter Barrel
192	EE	Electromagnetic CALorimeter Endcap
193	ES	Electromagnetic CALorimeter pre-Shower
194	EMG	Exponentially Modified Gaussian
195	EPJC	European Physical Journal C
196	EWK	Electroweak Sector
197	GCT	Global Calorimeter Trigger
198	GMT	Global MuonTrigger
199	GT	Global Trigger
200	HB	Hadron Barrel
201	HCAL	Hadronic CALorimeter

202	HE	Hadron Endcaps
203	HF	Hadron Forward
204	HLT	Higher Level Trigger
205	HO	Hadron Outer
206	HPD	Hybrid Photo Diode
207	LUT	Look Up Table
208	L1	Level 1 Trigger
209	LHC	Large Hadron Collider
210	LHCb	Large Hadron Collider Beauty
211	LSP	Lightest Supersymmetric Partner
212	POGs	Physics Object Groups
213	PS	Proton Synchrotron
214	QED	Quantum Electro-Dynamics
215	QCD	Quantum Chromo-Dynamics
216	QFT	Quantum Field Theory
217	RPC	Resistive Plate Chamber
218	RCT	Regional Calorimeter Trigger
219	RMT	Regional Muon Trigger
220	SUSY	SUperSYmmetry
221	SM	Standard Model
222	SMS	Simplified Model Spectra
223	SPS	Super Proton Synchrotron
224	TF	Transfer Factor
225	VEV	Vacuum Expectation Value
226	VPT	Vacuum Photo-Triodes

227 **WIMP** Weakly Interacting Massive Particle

²²⁸

“The Universe is about 1,000,000 years old.”

— Matthew Kenzie, 1987-present : Discoverer of the Higgs Boson.

²²⁹

Chapter 1.

²³⁰ Introduction

²³¹ During the 20th century great advances have been made in our understanding of the
²³² universe, where it comes from, where it is going and what it is made of. The Standard
²³³ Model (**SM**) first formulated in the 1960's is one of the crowning achievements in science's
²³⁴ quest to explain the most fundamental processes and interactions that make up our
²³⁵ universe. It has provided a highly successful explanation of a wide range of phenomena
²³⁶ in Particle Physics and has stood up to extensive experimental scrutiny [1].

²³⁷ Despite it's successes it is not a complete theory, with significant questions remaining
²³⁸ unanswered. It describes only three of the four known forces with gravity not incorpo-
²³⁹ rated within the framework of the **SM**. Cosmological experiments infer that just $\sim 4\%$
²⁴⁰ of the observable universe exists as matter, with elusive "Dark Matter" accounting for a
²⁴¹ further $\sim 23\%$ [2]. However no particle predicted by the **SM** is able to account for it. At
²⁴² higher energy scales and small distances the (non-)unification of the fundamental forces
²⁴³ point to problems with the **SM** at least at higher energies not yet probed experimentally.

²⁴⁴ Many theories exist as extensions to the **SM** and predict a range of observables
²⁴⁵ that can be detected at the Large Hadron Collider (**LHC**) of which SUperSYmmetry
²⁴⁶ (**SUSY**) is one such example. It predicts a new symmetry of nature in which all current
²⁴⁷ particles in the **SM** would have a corresponding supersymmetric partner. Common to
²⁴⁸ most Supersymmetric theories is a stable, weakly interacting Lightest Supersymmetric
²⁴⁹ Partner (**LSP**), which has the properties of a possible dark matter candidate. The **SM**
²⁵⁰ and the main principles of Supersymmetric theories are outlined in Chapter 2, with
²⁵¹ emphasis on placed on how experimental signatures of **SUSY** may reveal themselves at
²⁵² the **LHC**.

253 The experimental goal of the **LHC** is to further test the framework of the **SM**,
254 exploring the TeV mass scale for the first time, and to seek a connection between the
255 particles produced in proton collisions and dark matter. The first new discovery by
256 this extraordinary machine was announced on the 4th of July 2012. The long-awaited
257 discovery was the culmination decades of experimental endeavours in the search for the
258 Higgs boson, providing an answer to the mechanism of electroweak symmetry breaking
259 within the **SM** [3][4].

260 This discovery was made possible through data taken by the two multi purpose
261 detectors (**CMS** and A Toroidal LHC ApparatuS (**ATLAS**)) located on the **LHC** ring.
262 An experimental description of the **CMS** detector and the **LHC** is described in Chapter 3,
263 including some of the object reconstruction used by **CMS** in searches for **SUSY** signatures.
264 The performance of the **CMS** Level-1 calorimeter trigger, benchmarked by the author is
265 also included within this chapter.

266 The analysis conducted by the author is detailed within Chapter 4. This chapter
267 contains a description of the search for evidence of the production of Supersymmetric
268 particles at the **LHC**. The main basis of the search centres around the kinematic
269 dimensionless α_T variable, which provides strong rejection of backgrounds with fake
270 missing energy signatures whilst maintaining good sensitivity to a variety of **SUSY**
271 topologies. The author's work as an integral part of the analysis group is documented in
272 detail, which has culminated in numerous publications over the past two years. The latest
273 of which was published in the European Physical Journal C (**EPJC**) [5] and contains the
274 results which are discussed within this and the sequential Chapter.

275 The author in particular has played a major role in the extension of the α_T analysis into
276 the additional b-tagged and jet multiplicity dimensions increasing the sensitivity of the
277 analysis to a range of **SUSY** topologies. Additionally the author has worked extensively
278 in both increasing the statistical precision of electroweak predictions measured from
279 simulation through analytical techniques, and the derivation of a data driven systematic
280 uncertainty through the establishment of closure tests within the control samples of the
281 analysis.

282 Also included within this Chapter is a method to search for **SUSY** signatures which
283 are rich in top and bottom flavoured jet final states. A parametrisation of the b-tagging
284 distribution for different Electroweak processes is used to establish templates, which
285 are then used to estimate the expected number of 3 or 4 b-tagged jet events from **SM**

286 processes. The α_T search is used as a cross check for this template method to establish
287 it's functionality.

288 Finally the interpretation of such results within the framework of a variety of Simplified
289 Model Spectra (**SMS**), which describe an array of possible **SUSY** event topologies is
290 documented in Chapter 5. A description of the statistical model used to derive these
291 interpretations and the possible implications of the results presented in this thesis is
292 discussed within this Chapter. Natural units are used throughout this thesis in which \hbar
293 = c = 1.

Chapter 2.

²⁹⁴ A Theoretical Overview

²⁹⁵ Within this chapter, a brief introduction and background to the **SM** is given. Its success
²⁹⁶ as a rigorously tested and widely accepted theory is discussed as well as the deficiencies
²⁹⁷ with this theory that hint there this theory is not a complete description of our universe.
²⁹⁸ The motivations for new physics at the TeV scale and in particular Supersymmetric
²⁹⁹ theories are outlined within Section (2.3), with the chapter concluding with how an
³⁰⁰ experimental signature of such theories can be produced and observed at the **LHC**,
³⁰¹ Section (2.4).

³⁰² 2.1. The Standard Model

³⁰³ The **SM** is the name given to the relativistic Quantum Field Theory (**QFT**), where
³⁰⁴ particles are represented as excitations of fields, which describes the interactions and
³⁰⁵ properties of all the known elementary particles [6][7][8][9]. It is a renormalisable field
³⁰⁶ theory which contains three symmetries: $SU(3)$ for colour charge, $SU(2)$ for weak isospin
³⁰⁷ and $U(1)$ relating to weak hyper charge, which require its Lagrangian \mathcal{L}_{SM} to be invariant
³⁰⁸ under local gauge transformation.

³⁰⁹ Within the **SM** theory, matter is composed of spin $\frac{1}{2}$ fermions, which interact with each
³¹⁰ other via the exchange of spin-1 gauge bosons. A summary of the known fundamental
³¹¹ fermions and bosons is given in Table 2.1.

³¹² Fermions are separated into quarks and leptons of which only quarks interact with
³¹³ the strong nuclear force. Quarks unlike leptons are not seen as free particles in nature,
³¹⁴ but rather exist only within baryons, composed of three quarks with an overall integer

Particle	Symbol	Spin	Charge	Mass (GeV)
First Generation Fermions				
Electron Neutrino	ν_e	$\frac{1}{2}$	0	$< 2.2 \times 10^{-6}$
Electron	e	$\frac{1}{2}$	-1	0.51×10^{-3}
Up Quark	u	$\frac{1}{2}$	$\frac{2}{3}$	$2.3^{+0.7}_{-0.5} \times 10^{-3}$
Down Quark	d	$\frac{1}{2}$	$-\frac{1}{3}$	$4.8^{+0.7}_{-0.3} \times 10^{-3}$
Second Generation Fermions				
Muon Neutrino	ν_μ	$\frac{1}{2}$	0	-
Muon	μ	$\frac{1}{2}$	-1	1.05×10^{-3}
Charm Quark	c	$\frac{1}{2}$	$\frac{2}{3}$	1.275 ± 0.025
Strange Quark	s	$\frac{1}{2}$	$-\frac{1}{3}$	$95 \pm 5 \times 10^{-3}$
Third Generation Fermions				
Tau Neutrino	ν_τ	$\frac{1}{2}$	0	-
Tau	τ	$\frac{1}{2}$	-1	1.77
Top Quark	t	$\frac{1}{2}$	$\frac{2}{3}$	173.5 ± 0.8
Bottom Quark	b	$\frac{1}{2}$	$-\frac{1}{3}$	4.65 ± 0.03
Gauge Bosons				
Photon	γ	1	0	0
W Boson	W^\pm	1	± 1	80.385 ± 0.015
Z Boson	Z	1	0	91.187 ± 0.002
Gluons	g	1	0	0
Higgs Boson	H	0	0	125.3 ± 0.5 [4]

Table 2.1.: The fundamental particles of the SM, with spin, charge and mass displayed. Latest mass measurements taken from [1].

charge, and quark-anti-quark pairs called mesons. Both leptons and quarks are grouped into three generations which have the same properties, but with ascending mass in each subsequent generation.

The gauge bosons mediate the interactions between fermions. The field theories of Quantum Electro-Dynamics (QED) and Quantum Chromo-Dynamics (QCD), yield massless mediator bosons, the photon and eight coloured gluons which are consequences of the gauge invariance of those theories, detailed in Section (2.1.1).

The unification of the electromagnetic and weak-nuclear forces into the current Electroweak theory yield the weak gauge bosons, W^\pm and Z through the mixing of the associated gauge fields. The force carriers of this theory were experimentally detected by

325 the observation of weak neutral current, discovered in 1973 in the Gargamelle bubble
 326 chamber located at European Organization for Nuclear Research (**CERN**) [10], with the
 327 masses of and the weak gauge bosons measured by the UA1 and U2 experiments at the
 328 Super Proton Synchrotron (**SPS**) collider in 1983 [11][12].

329 2.1.1. Gauge Symmetries of the SM

330 Symmetries are of fundamental importance in the description of physical phenomena.
 331 Noether's theorem states that for a dynamical system, the consequence of any symmetry
 332 is an associated conserved quantity [13]. Invariance under translations, rotations, and
 333 Lorentz transformations in physical systems lead to conservation of momentum, energy
 334 and angular momentum.

335 In the **SM**, a quantum theory described by Lagrangian formalism, the weak, strong and
 336 electromagnetic interactions are described in terms of “gauge theories”. A gauge theory
 337 possesses invariance under a set of “local transformations”, which are transformations
 338 whose parameters are space-time dependent. The requirement of gauge invariance within
 339 the **SM** necessitates the introduction of force-mediating gauge bosons and interactions
 340 between fermions and the bosons themselves. Given the nature of the topics covered by
 341 this thesis, the formulation of Electroweak Sector (**EWK**) within the **SM** Lagrangian is
 342 reviewed within this section.

343 The simplest example of the application of the principle of local gauge invariance
 344 within the **SM** is in Quantum Electro-Dynamics (**QED**), the consequences of which
 345 require a massless photon field [14][15].

346 Starting from the free Dirac Lagrangian written as

$$\mathcal{L} = \bar{\psi}(i\gamma^\mu \partial_\mu - m)\psi, \quad (2.1)$$

347 where ψ represents a free non interacting fermionic field, with the matrices $\gamma^\mu, \mu \in$
 348 $0, 1, 2, 3$ defined by the anti commutator relationship $\gamma^\mu \gamma^\nu + \gamma^\nu \gamma^\mu = 2\eta^{\mu\nu} I_4$ where $\eta^{\mu\nu}$ is
 349 the flat space-time metric $(+, -, -, -)$ and I_4 is the 4×4 identity matrix.

350 Under a local U(1) abelian gauge transformation in which ψ transforms as:

$$\psi(x) \rightarrow \psi'(x) = e^{i\theta(x)}\psi(x) \quad \bar{\psi}(x) \rightarrow \bar{\psi}'(x) = e^{i\theta(x)}\bar{\psi}(x) \quad (2.2)$$

351 the kinetic term of the Lagrangian does not remain invariant, due to the partial
352 derivative interposed between the $\bar{\psi}$ and ψ yielding,

$$\partial_\mu \psi \rightarrow e^{i\theta(x)} \partial_\mu \psi + i e^{i\theta(x)} \psi \partial_\mu \theta. \quad (2.3)$$

353 To ensure that \mathcal{L} remains invariant, a modified derivative, D_μ , that transforms
354 covariantly under phase transformations is introduced. In doing this a vector field A_μ
355 with transformation properties that cancel out the unwanted term in (2.3) must also be
356 included,

$$D_\mu \equiv \partial_\mu - ieA_\mu, \quad A_\mu \rightarrow A_\mu + \frac{1}{e} \partial_\mu \theta. \quad (2.4)$$

357 Invariance of the Lagrangian is then achieved by replacing ∂_μ by D_μ :

$$\begin{aligned} \mathcal{L} &= i\bar{\psi}\gamma^\mu D_\mu \psi - m\bar{\psi}\psi \\ &= \bar{\psi}(i\gamma^\mu \partial_\mu - m)\psi + e\bar{\psi}\gamma^\mu \psi A_\mu \end{aligned} \quad (2.5)$$

358 An additional interaction term is now present in the Lagrangian, coupling the Dirac
359 particle to this vector field, which is interpreted as the photon in QED. To regard this
360 new field as the physical photon field, a term corresponding to its kinetic energy must be
361 added to the Lagrangian from Equation (2.5). Since this term must also be invariant
362 under the conditions of Equation (2.4), it is defined in the form $F_{\mu\nu} = \partial^\mu A^\nu - \partial^\nu A^\mu$.

363 This then leads to the Lagrangian of QED:

$$\mathcal{L}_{QED} = \underbrace{i\bar{\psi}\gamma^\mu\partial_\mu\psi - \frac{1}{4}F_{\mu\nu}F^{\mu\nu}}_{\text{kinetic term}} + \underbrace{m\bar{\psi}\psi}_{\text{mass term}} + \underbrace{e\bar{\psi}\gamma^\mu\psi A_\mu}_{\text{interaction term}} \quad (2.6)$$

364 Within the Lagrangian there remains no mass term of the form $m^2A_\mu A^\mu$, which is
 365 prohibited by gauge invariance. This implies that the gauge particle, the photon, must
 366 be massless.

367 2.1.2. The Electroweak Sector and Electroweak Symmetry 368 Breaking

369 The same application of gauge symmetry and the requirement of local gauge invariance
 370 can be used to unify QED and the Weak force in the Electroweak Sector (EWK).
 371 The nature of EWK interactions is encompassed within a Lagrangian invariant under
 372 transformations of the group $SU(2)_L \times U(1)_Y$.

373 The weak interactions from experimental observation [16], are known to violate parity
 374 and are therefore not symmetric under interchange of left and right helicity fermions.
 375 Thus within the SM the left and right handed parts of these fermion fields are treated
 376 separately. A fermion field is then split into two left and right handed chiral components,
 377 $\psi = \psi_L + \psi_R$, where $\psi_{L/R} = (1 \pm \gamma^5)\psi$.

378 The $SU(2)_L$ group is the special unitary group of 2×2 matrices U satisfying $UU^\dagger = I$
 379 and $\det(U) = 1$. It may be written in the form $U = e^{-i\omega_i T_i}$, with the generators of the
 380 group $T_i = \frac{1}{2}\tau_i$ where τ_i , $i \in 1,2,3$ being the 2×2 Pauli matrices

$$\tau_1 = \begin{pmatrix} 0 & 1 \\ 1 & 0 \end{pmatrix} \quad \tau_2 = \begin{pmatrix} 0 & -i \\ i & 0 \end{pmatrix} \quad \tau_3 = \begin{pmatrix} 1 & 0 \\ 0 & -1 \end{pmatrix}, \quad (2.7)$$

381 which form a non Abelian group obeying the commutation relation $[T^a, T^b] \equiv$
 382 $if^{abc}T^c \neq 0$. The gauge fields that accompany this group are represented by $\hat{W}_\mu =$
 383 $(\hat{W}_\mu^1, \hat{W}_\mu^2, \hat{W}_\mu^3)$ and act only on the left handed component of the fermion field ψ_L .

³⁸⁴ One additional generator Y which represents the hypercharge of the particle under
³⁸⁵ consideration is introduced through the $U(1)_Y$ group acting on both components of the
³⁸⁶ fermion field, with an associated vector boson field \hat{B}_μ .

³⁸⁷ The $SU(2)_L \times U(1)_Y$ transformations of the left and right handed components of ψ
³⁸⁸ are summarised by,

$$\begin{aligned}\chi_L &\rightarrow \chi'_L = e^{i\theta(x) \cdot T + i\theta(x)Y} \chi_L, \\ \psi_R &\rightarrow \psi'_R = e^{i\theta(x)Y} \psi_R,\end{aligned}\tag{2.8}$$

³⁸⁹ where the left handed fermions form isospin doubles χ_L and the right handed fermions
³⁹⁰ are isosinglets ψ_R . For the first generation of leptons and quarks this represents

$$\begin{aligned}\chi_L &= \begin{pmatrix} \nu_e \\ e \end{pmatrix}_L, \quad \begin{pmatrix} u \\ d \end{pmatrix}_L \\ \psi_R &= e_R, \quad u_R, d_R\end{aligned}\tag{2.9}$$

³⁹¹ Imposing local gauge invariance within \mathcal{L}_{EWK} is once again achieved by modifying
³⁹² the covariant derivative

$$D_\mu = \partial_\mu - \frac{ig}{2} \tau^i W_\mu^i - \frac{ig'}{2} Y B_\mu,\tag{2.10}$$

³⁹³ where g and g' are the coupling constant of the $SU(2)_L$ and $U(1)_Y$ groups respectively.
³⁹⁴ Taking the example of the first generation of fermions defined in Equation.(2.9), with input
³⁹⁵ hypercharge values of -1 and -2 for χ_L and e_R respectively, would lead to a Lagrangian
³⁹⁶ \mathcal{L}_1 of the form,

$$\begin{aligned}\mathcal{L}_1 = &\bar{\chi}_L \gamma^\mu [i\partial_\mu - g \frac{1}{2} \tau \cdot W_\mu - g' (-\frac{1}{2}) B_\mu] \chi_L \\ &+ \bar{e}_R \gamma^\mu [i\partial_\mu - g' (-1) B_\mu] e_R - \frac{1}{4} W_{\mu\nu} \cdot W^{\mu\nu} - \frac{1}{4} B_{\mu\nu} B^{\mu\nu}.\end{aligned}\tag{2.11}$$

³⁹⁷ As in **QED**, these additional gauge fields introduce field strength tensors $B_{\mu\nu}$ and
³⁹⁸ $W_{\mu\nu}$,

$$\hat{B}_{\mu\nu} = \partial_\mu \hat{B}_\nu - \partial_\nu \hat{B}_\mu \quad (2.12)$$

$$\hat{W}_{\mu\nu} = \partial_\mu \hat{W}_\nu - \partial_\nu \hat{W}_\mu - g \hat{W}_\mu \times \hat{W}_\nu \quad (2.13)$$

³⁹⁹ corresponding to the kinetic energy and self coupling of the W_μ fields and the kinetic
⁴⁰⁰ energy term of the B_μ field.

⁴⁰¹ None of these gauge bosons are physical particles, and instead linear combinations of
⁴⁰² these gauge bosons make up γ and the W and Z bosons, defined as

$$W^\pm = \frac{1}{\sqrt{2}} (W_\mu^1 \mp i W_\mu^2) \quad \begin{pmatrix} Z_\mu \\ A_\mu \end{pmatrix} = \begin{pmatrix} \cos\theta_W & -\sin\theta_W \\ \sin\theta_W & \cos\theta_W \end{pmatrix} \begin{pmatrix} W_\mu^3 \\ B_\mu \end{pmatrix} \quad (2.14)$$

⁴⁰³ where the mixing angle, $\theta_w = \tan^{-1} \frac{g'}{g}$, relates the coupling of the neutral weak and
⁴⁰⁴ electromagnetic interactions.

⁴⁰⁵ As in the case of the formulation of the **QED** Lagrangian there remains no mass term
⁴⁰⁶ for the photon. However this is also the case for the W, Z and fermions in the Lagrangian,
⁴⁰⁷ contrary to experimental measurement. Any explicit introduction of mass terms would
⁴⁰⁸ break the symmetry of the Lagrangian and instead mass terms can be introduced through
⁴⁰⁹ spontaneous breaking of the **EWK** symmetry via the Higgs mechanism.

⁴¹⁰ The Higgs mechanism induces spontaneous symmetry breaking through the introduc-
⁴¹¹ tion of a complex scalar SU(2) doublet field ϕ which attains a non-zero Vacuum
⁴¹² Expectation Value (**VEV**) [17][18][19][20].

$$\phi = \begin{pmatrix} \phi^+ \\ \phi^0 \end{pmatrix} \quad \text{with} \quad \begin{aligned} \phi^+ &\equiv (\phi_1 + i\phi_2)/\sqrt{2} \\ \phi^0 &\equiv (\phi_3 + i\phi_4)/\sqrt{2} \end{aligned} \quad (2.15)$$

413 The Lagrangian defined in Equation (2.11) attains an additional term \mathcal{L}_{Higgs} of the
414 form

$$\mathcal{L}_{Higgs} = \overbrace{(D_\mu \phi)^\dagger (D^\mu \phi)}^{\text{kinetic}} - \overbrace{\mu^2 \phi^\dagger \phi - \lambda (\phi^\dagger \phi)^2}^{\text{potential } V(\phi)} \quad (\mu^2, \lambda) > 0 \in \mathbb{R},$$

$$\mathcal{L}_{SM} = \mathcal{L}_{EWK} + \mathcal{L}_{Higgs}, \quad (2.16)$$

415 where the covariant derivative D_μ is that defined in Equation (2.10). The last two
416 terms of \mathcal{L}_{Higgs} correspond to the Higgs potential, in which positive real positive values
417 of μ^2 and λ are required to ensure the generation of masses for the bosons and leptons.
418 The minimum of this potential is found at $\phi^\dagger \phi = \frac{1}{2}(\phi_1^2 + \phi_2^2 + \phi_3^2 + \phi_4^2) = \mu^2/\lambda = v^2$,
419 where v represents the **VEV**.

420 Defining the ground state of the ϕ field to be consistent with the $V(\phi)$ minimum, and
421 then expanding around a ground state chosen to maintain an unbroken electromagnetic
422 symmetry thus preserving a zero photon mass [21] leads to

$$\phi_0 = \sqrt{\frac{1}{2}} \begin{pmatrix} 0 \\ v \end{pmatrix}, \quad \phi(x) = e^{i\tau \cdot \theta(x)/v} \sqrt{\frac{1}{2}} \begin{pmatrix} 0 \\ v + h(x) \end{pmatrix}, \quad (2.17)$$

423 where the fluctuations from the vacuum ϕ_0 are parametrized in terms of four real
424 fields, $\theta_1, \theta_2, \theta_3$ and $h(x)$.

425 Choosing to gauge away the three massless Goldstone boson fields by setting $\theta(x)$ to
426 zero and substituting $\phi(x)$ back into kinetic term of \mathcal{L}_{Higgs} from Equation (2.16) leads to
427 mass terms for the W^\pm and Z bosons

$$(D_\mu \phi)^\dagger (D^\mu \phi) = \frac{1}{2}(\partial_\mu h)^2 + \frac{g^2 v^2}{2} W_\mu^+ W^{-\mu} + \frac{v^2 g^2}{8 \cos^2 \theta_w} Z_\mu Z^\mu + 0 A_\mu A^\mu, \quad (2.18)$$

428 where the relations between the physical and electroweak gauge fields from Equation
429 (2.14) are used. The W^\pm and Z bosons can then be determined to be

$$M_W = \frac{1}{2}gv \quad M_Z = \frac{1}{2} \frac{gv}{\cos \theta_w}. \quad (2.19)$$

430 This mechanism is also used to generate fermion masses by introducing a Yukawa
 431 coupling between the fermions and the ϕ field [22], with the coupling strength of a particle
 432 to the ϕ field governing its mass. Additionally a scalar boson h with mass $m_h = v\sqrt{\frac{\lambda}{2}}$, is
 433 also predicted as a result of this spontaneous symmetry breaking and became known as
 434 the Higgs boson. Its discovery by the CMS and ATLAS experiments in 2012 is concrete
 435 evidence to support this method of mass generation within the SM.

436 2.2. Motivation for Physics Beyond the Standard 437 Model

438 As has been described, the SM has proved to be a very successful theory, predicting the
 439 existence of the W^\pm and Z bosons and the top quark long before they were experimentally
 440 observed. However the theory does not accurately describe all observed phenomena and
 441 has some fundamental theoretical flaws that hint at the need for additional extensions to
 442 the current theory.

443 On a theoretical level, the SM is unable to incorporate the gravitational interactions
 444 of fundamental particles within the theory. Whilst at the electroweak energy scales the
 445 relative strength of gravity is negligible compared to the other three fundamental forces,
 446 at much higher energy scales $M_{planck} \sim 10^{18} GeV$ quantum gravitational effects become
 447 increasingly dominant. The failure to reconcile gravity within the SM, demonstrates that
 448 the SM must become invalid at some higher energy scale.

449 Some other deficiencies with the SM include the fact that the predicted rate of
 450 Charge-Parity violation does not account for the matter dominated universe which we
 451 inhabit, and the SM prediction of zero neutrino mass conflicts with the observation of
 452 neutrino flavour mixing, attributed to mixing between neutrino mass eigenstates [23][24].

453 Perhaps one of the most glaring gaps in the predictive power of the SM is that there
 454 exists no candidate to explain the cosmic dark matter observed in galactic structures
 455 through indirect techniques including gravitational lensing and measurement of the
 456 orbital velocity of stars in galactic edges. Any such candidate must be very weakly

457 interacting which must also be stable, owing to the lack of direct detection of the decay
458 products of such an process. Providing a dark matter candidate is of the prime goals
459 which be tackled by any Beyond Standard Model (**BSM**) physics model.

460 The recent discovery of the Higgs boson whilst a significant victory for the predictive
461 power of the **SM**, brings with it still unresolved questions. This issue is commonly
462 described as the “hierarchy problem”.

463 In the absence of new physics between the TeV and Planck scale, calculating beyond
464 tree-level contributions to the Higgs mass term given by its self interaction, result in
465 divergent terms that push the Higgs mass up to the planck mass M_{planck} .

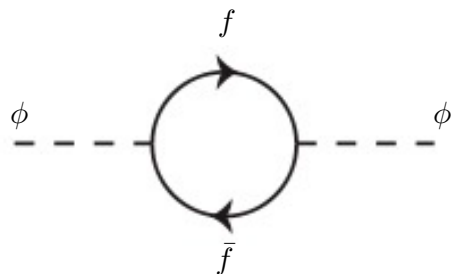


Figure 2.1.: One loop quantum corrections to the Higgs squared mass parameter m_h^2 due to a fermion.

466 This can be demonstrated by considering the one loop quantum correction to the
467 Higgs mass with a fermion f , shown in Figure 2.1 with mass m_f . The Higgs field couples
468 to f with a term in the Lagrangian $-\lambda_f h \bar{f} f$, yielding a correction of the form [25],

$$\delta m_h^2 = -\frac{|\lambda_f|^2}{8\pi^2} \Lambda^2 + \dots, \quad (2.20)$$

469 where λ_f represents the coupling strength for each type of fermion $\propto m_f$, and Λ the
470 cutoff energy scale at which the **SM** ceases to be a valid theory.

471 To recover the mass of the now discovered Higgs boson would require a fine-tuning of
472 the parameters to cancel out these mass corrections the the Higgs mass to the scale of
473 30 orders of magnitude. This appears as an unnatural solution to physicists and it is
474 this hierarchy problem that provides one of the strongest motivations for the theory of
475 SUperSYmmetry (**SUSY**).

⁴⁷⁶ 2.3. Supersymmetry Overview

⁴⁷⁷ Supersymmetry provides potential solutions to many of the issues raised in the previous
⁴⁷⁸ section. It provides a dark matter candidate, can explain baryogenesis in the early
⁴⁷⁹ universe and also provides an elegant solution to the hierarchy problem [26][27][28][29].
⁴⁸⁰ At its heart it represents a new space-time symmetry that relates fermions and bosons.
⁴⁸¹ This symmetry converts bosonic states into fermionic states, and vice versa, see Equation
⁴⁸² (2.21) ,

$$Q|Boson\rangle = |Fermion\rangle \quad Q|Fermion\rangle = |Boson\rangle, \quad (2.21)$$

⁴⁸³ where the operator Q is the generator of these transformations. Quantum field theories
⁴⁸⁴ which are invariant under such transformations are called supersymmetric.

⁴⁸⁵ This symmetry operator therefore acts upon a particles spin altering it by a half integer
⁴⁸⁶ value. The consequences of the introduction of this additional space-time symmetry
⁴⁸⁷ introduce a new rich phenomenology. For example in supersymmetric theories, both
⁴⁸⁸ the left handed $SU(2)$ doublet and right handed singlet of fermions will have a spin-0
⁴⁸⁹ superpartner, containing the same electric charge, weak isospin, and colour as its **SM**
⁴⁹⁰ partner. In the case of the leptons $(\nu_l, l)_L$ will have two superpartners, a sneutrino $\tilde{\nu}_l{}_L$
⁴⁹¹ and a slepton \tilde{l}_L , whilst the singlet l_R also has a superpartner slepton \tilde{l}_R .

⁴⁹² Each particle in a supersymmetric theory is paired together with their superpartners
⁴⁹³ as a result of this supersymmetric transformations in a so called supermultiplet. These
⁴⁹⁴ superpartners will then consequently also contribute to the corrections to the Higgs mass.
⁴⁹⁵ Bosonic and fermionic loops contributing to the correction appear with opposite signs,
⁴⁹⁶ and therefore cancellation of these divergent terms will stabilise the Higgs mass, solving
⁴⁹⁷ the hierarchy problem [30][31].

⁴⁹⁸ One of the simplest forms of **SUSY** would predict a whole set of supersymmetric
⁴⁹⁹ partners to their **SM** counterparts with the same mass and interactions. However the
⁵⁰⁰ currently lack of any experimental evidence for the predicted sparticle spectrum implies
⁵⁰¹ **SUSY** must be a broken symmetry in which any sparticle masses must be greater than
⁵⁰² their SM counterparts.

⁵⁰³ There exist many techniques which can induce supersymmetric breaking [32][33][34].
⁵⁰⁴ Of particular interest to experimental physicists are those at which the breaking scale

505 is of an order that is experimentally accessible to the LHC i.e. \sim TeV scale. Whilst
 506 there is no requirement for supersymmetric breaking to occur at this energy scale, for
 507 supersymmetry to provide a solution to the hierarchy problem, it is necessary for this
 508 scale to not differ too drastically from the EWK scale [35][36].

509 2.3.1. R-Parity

510 Some supersymmetric theories also present a solution to the dark matter problem. Such
 511 theories can contain a Lightest Supersymmetric Partner (LSP), which matches the criteria
 512 of a Weakly Interacting Massive Particle (WIMP) required by cosmological observation
 513 if R-parity is conserved.

514 Baryon (B) and Lepton (L) number conservation is forbidden in the SM by renor-
 515 malisability requirements. The violation of Baryon or Lepton number would result in
 516 the proton lifetime much shorter than those set by experimental limits [37]. Another
 517 symmetry called R-parity is then often introduced to SUSY theories to maintain baryon
 518 and lepton conservation.

519 R-parity is described by the equation

$$R_P = (-1)^{3(B-L)+2s}, \quad (2.22)$$

520 where s represents the spin of the particles. $B = \pm \frac{1}{3}$ for quarks/antiquarks and $B = 0$
 521 for all others, $L = \pm 1$ for leptons/antileptons, $L = 0$ for all others.

522 R-parity ensures the stability of the proton in SUSY models, and also has other
 523 consequences for the production and decay of supersymmetric particles. At particle
 524 colliders supersymmetric particles can only be pair produced, and similarly the decay
 525 of any produced supersymmetric particle is restricted to a SM particle and a lighter
 526 supersymmetric particle as allowed by conservation laws. A further implication of R-
 527 parity is that once a supersymmetric particle has decayed to the LSP it remains stable,
 528 unable to decay into a SM particle.

529 A LSP would not interact in a detector at a particle collider, leaving behind a missing
 530 energy \cancel{E}_T signature. The assumption of R-parity and its consequences are used to
 531 determine the physical motivation and search strategies for SUSY model at the LHC.

532 2.4. Experimental signatures of SUSY at the LHC

533 Should strongly interacting sparticles be within the experimental reach of the LHC, then
534 it is expected that they can be produced in a variety of ways.

- 535 • squark/anti-squark and gluino pairs can be produced via both gluon fusion and
536 quark/anti-quark scattering.
- 537 • a gluino and squark produced together via quark-gluon scattering
- 538 • squark pairs produced via quark-quark scattering

539 Whilst most SUSY searches invoke the requirement of R-parity to explore parameter
540 phase space, there still exist a whole plethora of possible SUSY model topologies which
541 could be discovered at the LHC.

542 During the 2011 run period at a $\sqrt{s} = 7$ TeV particular models were used to benchmark
543 performance and experimental reach of both CMS searches and previous experiments.
544 The Compressed Minimal SuperSymmetric Model (CMSSM) was initially chosen for a
545 number of reasons [38]. One of the most compelling being the reduction from the up to
546 105 new parameters introduced by SUSY in addition to the existing 19 of the SM to that
547 of just 5 free extra free parameters. It was this simplicity, combined with the theory not
548 requiring any fine tuning of particle masses to produce the experimentally verified SM
549 that made it an attractive model to interpret physics results.

550 However recent results from the LHC now strongly disfavour large swathes of CMSSM
551 parameter space [39][40][41]. In the face of such results a more pragmatic model indepen-
552 dent search strategy is now applied across most SUSY searches at the LHC, see Section
553 (2.4.1).

554 As previously stated, a stable LSP that exhibits the properties of a dark matter would
555 be weakly interacting and therefore will not be directly detected in a detector environment.
556 Additionally the cascade decays of supersymmetric particles to the LSP would also result
557 in significant hadronic activity. These signatures can then be characterised through
558 large amounts of hadronic jets (see Section (3.3.1)), leptons and a significant amount of
559 missing energy dependent upon the size of the mass splitting between the LSP and the
560 supersymmetric particle it has decayed from.

561 Whilst the SM contains processes which can exhibit a similar event topology to that
562 described above. The largest contribution of which comes in from the general QCD

563 environment of a hadron collider. A multitude of different analytical techniques are used
564 by experimental physicists to reduce or estimate any reducible or irreducible backgrounds,
565 allowing a possible **SUSY** signature to be extracted. The techniques employed within
566 this thesis are described in great detail within Section (4.1).

567 **2.4.1. Simplified Models**

568 With such a variety of different ways for a **SUSY** signal to manifest itself, it is necessary
569 to be able to interpret experimental reach through the masses of gluinos and squarks
570 which can excluded by experimental searches rather than on a model specific basis.

571 This is accomplished through **SMS** models, which are defined by a set of hypothetical
572 particles and a sequence of their production and decay [42][43]. In the **SMS** models
573 considered within this thesis, only the production process for the two primary particles
574 are considered. Each primary particle can undergo a direct or a cascade decay through
575 an intermediate new particle. At the end of each decay chain there remains a neutral,
576 undetected **LSP** particle, denoted $\tilde{\chi}_{LSP}$ which can represent a neutralino or gravitino.
577 Essentially it is easier to consider each **SMS** with branching ratios set to 100% The
578 masses of the primary particle and the **LSP** remain as free parameters, in which the
579 absolute value and relative difference between the primary and **LSP** particle alter the
580 kinematics of the event.

581 Different **SMS** models are denoted with a T-prefix, with a summary of the types
582 interpreted within this thesis listed below [44].

- 583 • **T1,T1xxxx**, models represent a simplified version of gluino pair production with
584 each gluino (superpartner to the gluon) undergoing a three-body decay to a quark-
585 antiquark pair and the **LSP** (i.e. $\tilde{g} \rightarrow q\bar{q}\tilde{\chi}_{LSP}$). The resultant final state from this
586 decay is typically 4 jets + \cancel{E}_T in the absence of initial/final state radiation and
587 detector effects. xxxx denotes models in which the quarks are of a specific flavour,
588 typically t or b quark-antiquarks.
- 589 • **T2,T2xx**, models represent a simplified version of squark anti-squark production
590 with each squark undergoing a two-body decay into a light-flavour quark and **LSP**
591 (i.e. $\tilde{q} \rightarrow q\tilde{\chi}_{LSP}$). This results in final states with less jets than gluino mediated
592 production, typically 2 jets + \cancel{E}_T when again ignoring the effect of initial/final state
593 radiation and detector effects. xx models again represent decays in which both the
594 quark and the squark within the decay is of a specific flavour, typically \tilde{t}/t or \tilde{b}/b .

Models rich in b and t quarks are interpreted within this thesis as they remain of particular interest within “Natural SUSY” scenarios [45][46]. The largest contribution to the quadratic divergence in the Higgs mass parameter comes from a loop of top quarks via the Yukawa coupling. Cancellation of these divergences can be achieved in supersymmetric theories by requiring a light right handed top squark, \tilde{t}_R , and left-handed double $SU(2)_L$ doublet containing top and bottom squarks, $(\tilde{\frac{t}{b}})_L$ [47].

These theories therefore solve the hierarchy problem by predicting light \sim EWK scale third generation sleptons, to be accessible at the LHC. Search strategies involving the requirement of b-tagging (see Section (3.3.2)) are used to give sensitivity to these type of SUSY scenarios and are discussed in greater detail within Chapter 5.

Two example decay chains are shown in Figure 2.2; the pair production of gluinos (T1) and the pair production of squarks (T2) decaying into SM particles and LSP’s.

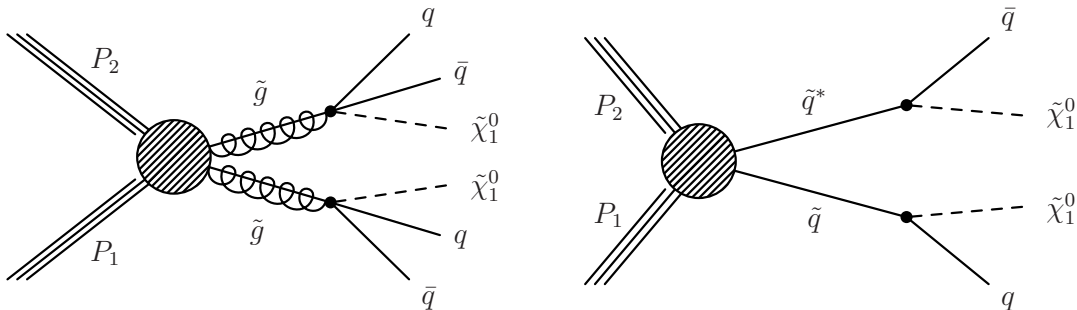


Figure 2.2.: Two example SMS model decays (T1 (left), T2 (right)), which are used in interpretations of physics reach by CMS.

Chapter 3.

⁶⁰⁷ The LHC and the CMS Detector

⁶⁰⁸ Probing the SM for signs of new physics would not be possible without the immensely
⁶⁰⁹ complex electronics and machinery that makes the TeV energy scale accessible for the
⁶¹⁰ first time. This chapter will cover the LHC based at European Organization for Nuclear
⁶¹¹ Research (CERN) and the Compact Muon Solenoid (CMS) detector, being the experiment
⁶¹² the author is a member of. Section (3.2) serves to introduce an overview of the different
⁶¹³ components of the CMS detector, with more detail spent on those that are relevant in
⁶¹⁴ the search for Supersymmetric particles. Section (3.3) will focus on event and object
⁶¹⁵ reconstruction again with more emphasis on jet level quantities which are most relevant
⁶¹⁶ to the author's analysis research. Finally Section (3.4) will cover work performed by
⁶¹⁷ the author, as service to the CMS Collaboration, in measuring the performance of the
⁶¹⁸ Global Calorimeter Trigger (GCT) component of the L1 trigger during the 2012-2013
⁶¹⁹ run period.

⁶²⁰ 3.1. The LHC

⁶²¹ The LHC is a storage ring, accelerator, and collider of circulating beams of protons or
⁶²² ions. Housed in the tunnel dug for the Large Electron-Positron collider (LEP), it is
⁶²³ approximately 27 km in circumference, 100 m underground, and straddles the border
⁶²⁴ between France and Switzerland outside of Geneva. It is currently the only collider
⁶²⁵ in operation that is able to study physics at the TeV scale. A double-ring circular
⁶²⁶ synchrotron, it was designed to collide both proton-proton (pp) and heavy ion (PbPb)
⁶²⁷ with a centre of mass energy $\sqrt{s} = 14$ TeV at a final design luminosity of $10^{34}\text{cm}^{-2}\text{s}^{-1}$.

⁶²⁸

These counter-circulating beams of protons/Pb ions are merged in four sections around the ring to enable collisions of the beams, with each interaction point being home to one of the four major experiments; A Large Ion Collider Experiment (**ALICE**) [48], A Toroidal LHC ApparatuS (**ATLAS**) [49], Compact Muon Solenoid (**CMS**) [50] and Large Hadron Collider Beauty (**LHC-B**) [51] which record the resultant collisions. The layout of the **LHC** ring is shown in Figure 3.1. The remaining four sections contain acceleration, collimation and beam dump systems. In the eight arc sections, the beams are steered by magnetic fields of up to 8 T provided by super conduction dipole magnets, which are maintained at temperatures of 2 K using superfluid helium. Additional magnets for focusing and corrections are also present in straight sections within the arcs and near the interaction regions where the detectors are situated.

640

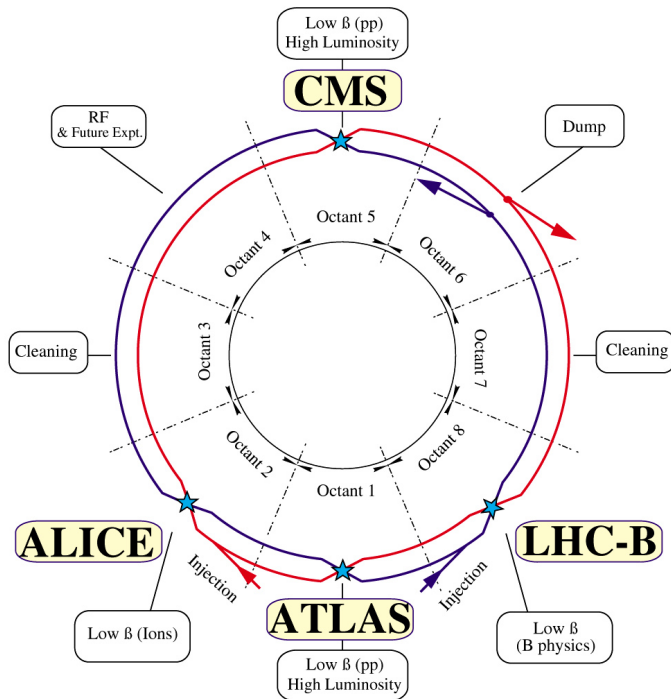


Figure 3.1.: A top down layout of the LHC. [52], with the position of the four main detectors labelled.

Proton beams are formed inside the Proton Synchrotron (**PS**) from bunches of protons 50 ns apart with an energy of 26 GeV. The protons are then accelerated in the Super Proton Synchrotron (**SPS**) to 450 GeV before being injected into the **LHC**. These **LHC** proton beams consists of many “bunches” i.e. approximately 1.1×10^{11} protons localized into less than 1 ns in the direction of motion. Before collision the beams are ramped to 4

646 TeV (2012) per beam in a process involving increasing the current passing through the
 647 dipole magnets. Once the desired \sqrt{s} energy is reached then the beams are allowed to
 648 collide at the interaction points. The luminosity falls regularly as the run progresses as
 649 protons are lost in collisions, and eventually the beam is dumped before repeating the
 650 process again.

651

652 Colliding the beams produced an instantaneous luminosity of approximately $5 \times$
 653 $10^{33} \text{ cm}^{-2}\text{s}^{-1}$ during the 2012 run. The high number of protons in each bunch increases
 654 the likelihood of multiple interactions with each crossing of the counter-circulating
 655 beams. This leads to isotropic energy depositions within the detectors positioned at these
 656 interaction points, increasing the energy scale of the underlying event. This is known as
 657 pile-up and the counteracting of it's effects are important to the many measurements
 658 performed at the LHC.

659 In the early phase of prolonged operation after the initial shutdown the machine
 660 operated in 2010-2011 at 3.5 TeV per beam, $\sqrt{s} = 7 \text{ TeV}$, delivering 6.13 fb^{-1} of data
 661 [53]. During the 2012-2013 run period, data was collected at an increased $\sqrt{s} = 8 \text{ TeV}$
 662 improving the sensitivity of searches for new physics. Over the whole run period 23.3
 663 fb^{-1} of data was delivered of which 21.8 fb^{-1} was recorded by the CMS detector as shown
 664 in Figure 3.2 [53]. A total of 12 fb^{-1} of 8 TeV certified data was collected by October
 665 2012, and it is this data which forms the basis of the results discussed within this thesis.

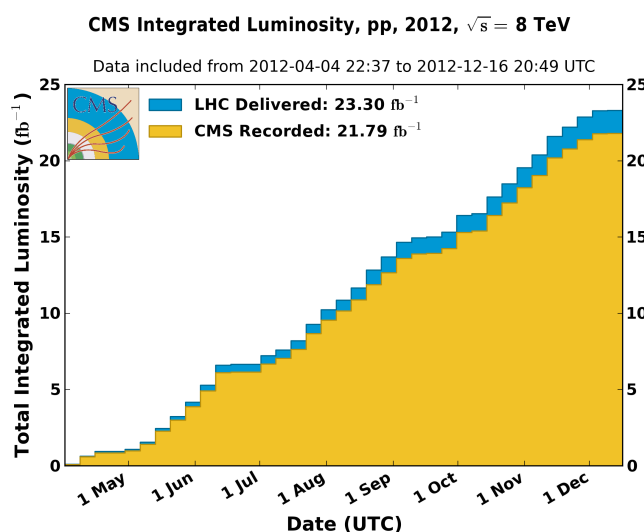


Figure 3.2.: The total integrated luminosity delivered to and collected by CMS during the 2012 8 TeV pp runs.

666 3.2. The CMS detector

667 The Compact Muon Solenoid (**CMS**) detector is one of two general purpose detectors
 668 at the **LHC** designed to search for new physics. The detector is designed to provide
 669 efficient identification and measurement of many physics objects including photons,
 670 electrons, muons, taus, and hadronic showers over wide ranges of transverse momentum
 671 and direction. Its nearly 4π coverage in solid angle allows for accurate measurement of
 672 global transverse momentum imbalance. These design factors give **CMS** the ability to
 673 search for direct production of **SUSY** particles at the TeV scale, making the search for
 674 Supersymmetric particles one of the highest priorities among the wide range of physics
 675 programmes at **CMS**.

676

677 **CMS** uses a right-handed Cartesian coordinate system with the origin at the interaction
 678 point and the z-axis pointing along the beam axis, the x-axis points radially inwards to
 679 the centre of the collider ring, with the y-axis points vertically upward. The azimuthal
 680 angle, ϕ ranging between $[-\pi, \pi]$ is defined in the x-y plane starting from the x-axis. The
 681 polar angle θ is measured from the z axis. The common convention in particle physics is
 682 to express an out going particle in terms of ϕ and its pseudorapidity defined as

$$\eta = -\log \tan \left(\frac{\theta}{2} \right). \quad (3.1)$$

683 The variable $\Delta R = \sqrt{\Delta\phi^2 + \Delta\eta^2}$ is commonly used to define angular distance
 684 between objects within the detector and additionally energy and momentum is typically
 685 measured in the transverse plane perpendicular to the beam line. These values are
 686 calculated from the x and y components of the object and are denoted as $E_T = E \sin \theta$
 687 and $p_T = \sqrt{p_x^2 + p_y^2}$.

688 3.2.1. Detector Subsystems

689 As the range of particles produced in pp collisions interact in different ways with mat-
 690 ter, **CMS** is divided into subdetector systems, which perform complementary roles to
 691 identify the identity, mass and momentum of the different physics objects present in
 692 each event. These detector sub-systems contained inside **CMS** are wrapped in layers

693 around a central 13 m long 4 T super conducting solenoid as shown in Figure 3.3. With
 694 the endcaps closed , CMS is a cylinder of length 22 m, diameter 15 m, and mass 12.5
 695 kilotons. A more detailed complete description of the detector can be found elsewhere [50].
 696

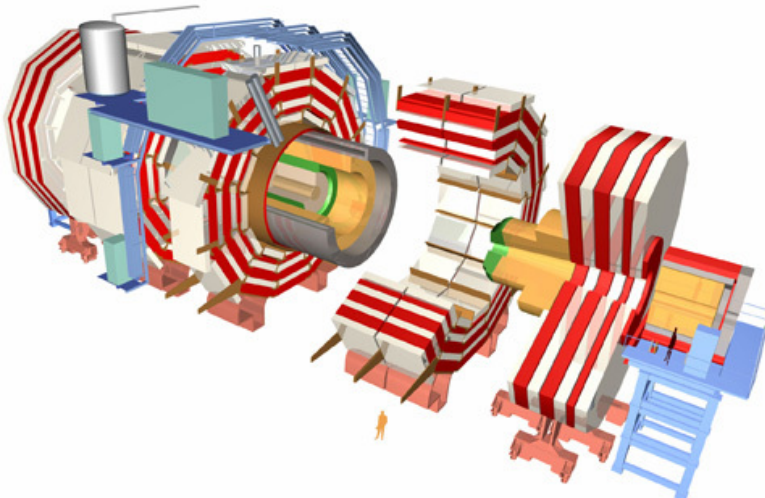


Figure 3.3.: A pictorial depiction of the CMS detector with the main detector subsystems labelled. [54]

697 3.2.2. Tracker

698 The inner-most subdetector of the barrel is the multi-layer silicon tracker, formed of a
 699 pixel detector component encased by layers of silicon strip detectors. The pixel detector
 700 consists of three layers of silicon pixel sensors providing measurements of the momentum,
 701 position coordinates of the charged particles as they pass, and the location of primary
 702 and secondary vertices between 4cm and 10cm transverse to the beam. Outside the pixel
 703 detector, ten cylindrical layers of silicon strip detectors extend the tracking system out to
 704 a radius of 1.20m from the beam line. The tracking system provides efficient and precise
 705 determination of the charges, momenta, and impact parameters of charged particles with
 706 the geometry of the tracker extending to cover a rapidity range up to $|\eta| < 2.5$.
 707

708 The tracking system also plays a crucial part in the identification of jets originating
 709 from b-quarks through measurement of displaced secondary vertices, which is covered in
 710 more detail in Section (3.3.2). The identification of b-jets is important in many searches

711 for natural SUSY models and forms an important part of the inclusive search strategy
712 described within Section (4.2).

713 **3.2.3. Electromagnetic Calorimeter**

714 Immediately outside of the tracker, but still within the magnet core, sits the Electromag-
715 netic CALorimeter (**ECAL**). Covering a pseudorapidity up to $|\eta| < 3$ and comprising
716 of over 75,000 PbWO₄ (lead tungstate) crystals that scintillate as particles deposit energy,
717 the **ECAL** provides high resolution measurements of the electromagnetic showers from
718 photons, electrons in the detector.

719

720 Lead tungstate is used because of its short radiation length ($X_0 \sim 0.9\text{cm}$) and small
721 Molieré radius ($\sim 2.1\text{cm}$) leading to high granularity and resolution. It's fast scintillation
722 time ($\sim 25\text{ns}$) reduces the effects of pile-up due to energy from previous collisions still
723 being read out, and its radiation hardness gives it longevity. The crystals are arranged
724 in modules which surround the beam line in a non-projective geometry, angled at 3°
725 with respect to the interaction point to minimise the risk of particles escaping down the
726 cracks between the crystals.

727

728 The **ECAL** is primarily composed of two sections, the Electromagnetic CALorime-
729 ter Barrel (**EB**) which extends in pseudo-rapidity to $|\eta| < 1.479$ with a crystal front
730 cross section of $22 \times 22 \text{ mm}^2$ and a length of 230 mm corresponding to 25.8 radia-
731 tion lengths, and the Electromagnetic CALorimeter Endcap (**EE**) covering a rapidity
732 range of $1.479 < |\eta| < 3.0$, which consists of two identical detectors on either side of
733 the **EB**. A lead-silicon sampling ‘pre-shower’ detector Electromagnetic CALorimeter
734 pre-Shower (**ES**) is placed before the endcaps to aid in the identification of neutral pions.
735 Their arrangement are shown in Figure 3.4.

736

737 Scintillation photons from the lead tungstate crystals are instrumented with Avalanche
738 Photo-Diodes (**APD**) and Vacuum Photo-Triodes (**VPT**) located in the **EB** and **EE**
739 respectively, converting the scintillating light into an electric signal which is consequently
740 used to determine the amount of energy deposited within the crystal . These instruments
741 are chosen for their resistance under operation to the strong magnetic field of **CMS**. The
742 scintillation of the **ECAL** crystals as well as the response of the **APDs** varies as a function

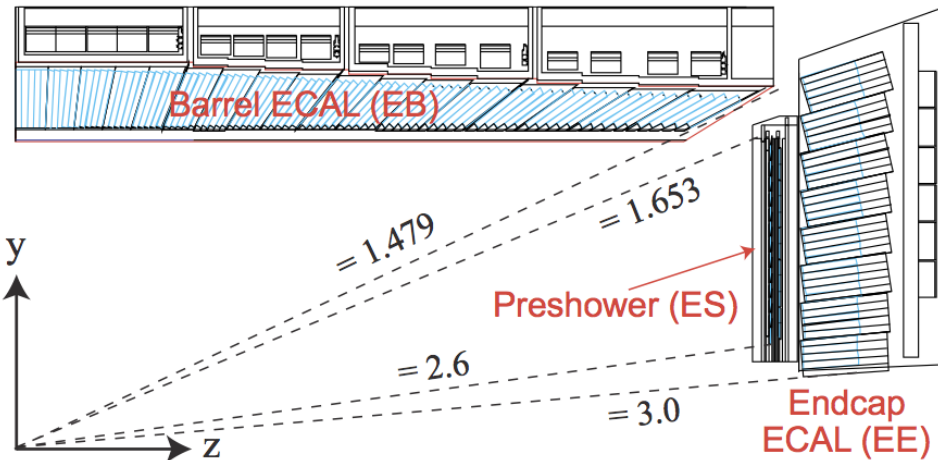


Figure 3.4.: Illustration of the CMS ECAL showing the arrangement of the lead tungstate crystals in the EB and EE. The ES is also shown and is located in front of the EE [55].

743 of temperature and so cooling systems continually maintain an overall constant ECAL
 744 temperature $\pm 0.05^\circ C$.

745 3.2.4. Hadronic Calorimeter

746 Beyond the ECAL lies the Hadronic CALorimeter (HCAL) which is responsible for
 747 the accurate measurement of hadronic showers, crucial for analyses involving jets or
 748 missing energy signatures. The HCAL is a sampling calorimeter which consists of al-
 749 ternating layers of brass absorber and plastic scintillator, except in the hadron forward
 750 ($3.0 < |\eta| < 5.0$) region in which steel absorbers and quartz fibre scintillators are used
 751 because of their increased radiation tolerance. Hadron showers are initiated in the
 752 absorber layers inducing scintillation in the plastic scintillator tiles. These scintillation
 753 photons are converted by wavelength shifting fibres for read-out by hybrid photodiodes.
 754

755 The HCAL's size is constrained to a compact size by the presence of the solenoid,
 756 requiring the placement of an additional outer calorimeter on the outside of the solenoid
 757 to increase the sampling depth of the HCAL. A schematic of the HCAL can be seen in
 758 Figure 3.5.

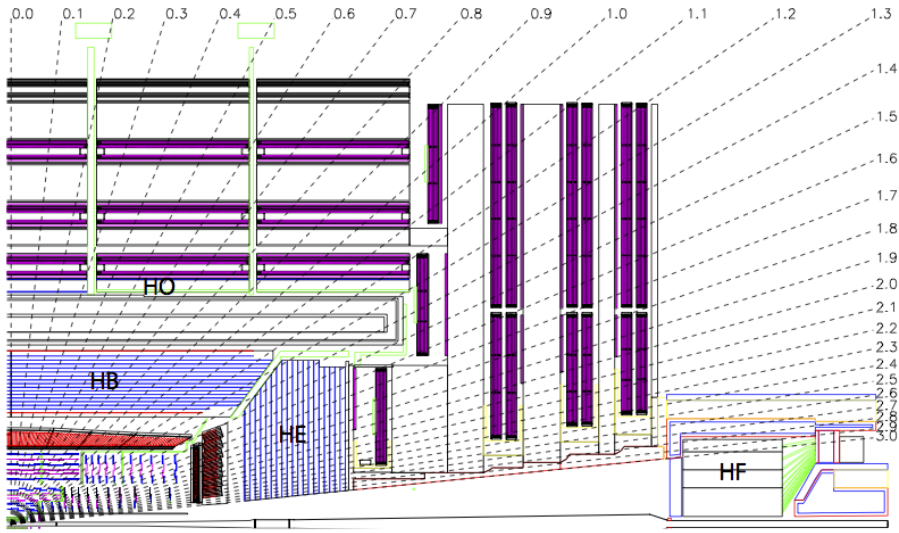


Figure 3.5.: Schematic of the hadron calorimeters in the r-z plane, showing the locations of the **HCAL** components and the **HF**. [50].

760 The **HCAL** covers the range $|\eta| < 5$ and consists of four subdetectors: the Hadron
 761 Barrel (**HB**) $|\eta| < 1.3$, the Hadron Outer (**HO**), the Hadron Endcaps (**HE**) $1.3 < |\eta| < 3.0$
 762 and the Hadron Forward (**HF**). The **HB** is contained between the outer edge of the **ECAL**
 763 and the inner edge of the solenoid, formed of 36 azimuthal wedges it is split between
 764 two half-barrel segments. Each wedge is segmented into four azimuthal angle (ϕ) sectors,
 765 and each half-barrel is further segmented into 16 η towers. The electronic readout chain,
 766 channels the light from the active scintillator layers from one ϕ -segment and all η -towers
 767 of a half-barrel to a Hybrid Photo Diode (**HPD**).

768 The relatively short number of interaction lengths (λ_l , the distance a hadron will
 769 travel through the absorber material before it has lost $\frac{1}{e}$ of its energy) within the **HB**,
 770 the lowest being $\lambda_l = 5.82$ for $|\eta| = 0$, facilitates the need for the ‘tail catching’ **HO**
 771 to increase the sampling depth in the central barrel rapidity region $|\eta| < 1.3$ to 11
 772 interaction lengths . Significant fractions of the hadrons energy will be deposited in the
 773 **ECAL** as it passed through the detector. Therefore measurements of hadron energies
 774 in the central regions $|\eta| < 3.0$ use both the **ECAL** and **HCAL** to reconstruct the true
 775 energy from showering hadrons.

776 **3.2.5. Muon Systems**

777 Muons being too massive to radiate away energy via Bremsstrahlung, interact little in
778 the calorimeters and mostly pass through the detector until they reach the system of
779 muon detectors which forms the outer most part of the **CMS** detector.

780 Outside of the superconducting solenoid are four muon detection layers interleaved
781 with the iron return yokes which measure the muons energy via ionisation of gas within
782 detector elements. Three types of gaseous chamber are used. The Drift Tube (**DT**),
783 Cathode Stripe Chamber (**CSC**), and Resistive Plate Chamber (**RPC**) systems provide
784 efficient detection of muons with pseudo-rapidity $|\eta| < 2.4$. The best reconstruction
785 performance is obtained when the muon chamber is combined with the inner tracking
786 information to determine muon trajectories and their momenta [56].

787

788 **3.3. Event Reconstruction and Object Definition**

789 The goal of event reconstruction is to take the raw information recorded by the detector
790 and to compute from it higher-level quantities which can be used at an analysis level.
791 These typically correspond to an individual particle’s energy and momenta, or groups of
792 particles which shower in a narrow cone and the overall global energy and momentum
793 balance of the event. The reconstruction of these objects are described in great detail in
794 [57], however covered below are brief descriptions of those which are most relevant to the
795 analysis detailed in Chapter 4.

796 **3.3.1. Jets**

797 Quarks and gluons are produced copiously at the LHC in the hard scattering of partons.
798 As these quarks and gluons fragment, they hadronise and decay into a group of strongly
799 interactive particles and their decay products. These streams of particles travel in the
800 same direction, as they have been “boosted” by the momentum of the primary hadron.
801 These collections of decay products are reconstructed and identified together as a “jet”.

802 At **CMS** jets are reconstructed from energy deposits in the detector using the anti-kt
803 algorithm [58] with size parameter $\Delta R = 0.5$. The anti-kt jet algorithm clusters jets by
804 defining a distance between hard (high p_T) and soft (low p_T) particles such that soft

805 particles are preferentially clustered with hard particles before being clustered between
806 themselves. This produces jets which are robust to soft particle radiation from the pile-up
807 conditions experienced at the **LHC**.

808

809 There are two main type of jet reconstruction used at **CMS**, Calorimeter (Calo) and
810 Particle Flow (PF) jets [59]. Calorimeter jets are reconstructed using both the **ECAL**
811 and **HCAL** cells, combined into calorimeter towers . These calorimeter towers consist of
812 geometrically matched **HCAL** cells and **ECAL** crystals. Electronics noise is suppressed by
813 applying a threshold to the calorimeter cells, with pile-up effects reduced by a requirement
814 placed on the tower energy [60]. Calorimter jets are the jets used within the analyses
815 described in this thesis.

816 PF jets are formed from combining information from all of the **CMS** subdetectors
817 systems to determine which final state particles are present in the event. Generally,
818 any particle is expected to produce some combination of a track in the silicon tracker,
819 a deposit in the calorimeters, or a track in the muon system. The PF jet momentum
820 and spatial resolutions are greatly improved with respect to calorimeter jets, as the use
821 of the tracking detectors and of the high granularity of **ECAL** allows resolution and
822 measurement of charged hadrons and photons inside a jet, which together constitute \sim
823 85% of the jet energy [61].

824 The jets reconstructed by the clustering algorithm in **CMS** typically have an energy
825 that differs to the ‘true’ energy measured by a perfect detector. This stems from the
826 non-linear and nonuniform response of the calorimeters as well as other residual effects
827 including pile-up and underlying events, and therefore additional corrections are applied
828 to recover a uniform relative response as a function of pseudo-rapidity. These are applied
829 as separate sub corrections [62].

- 830 • A PU correction is first applied to the jet. It subtracts the average extra energy
831 deposited in the jet that comes from other vertices present in the event and is
832 therefore not part of the hard jet itself.
- 833 • p_T and η dependant corrections derived from Monte Carlo simulations are used to
834 account for the non-uniform response of the detector.
- 835 • p_T and η residual corrections are applied to data only to correct for difference
836 between data and Monte Carlo. The residual is derived from QCD dijet samples
837 and the p_T residual from $\gamma+$ jet and $Z+$ jets samples in data.

838 3.3.2. B-tagging

839 The decays of b quarks are suppressed by small CKM matrix elements. As a result, the
840 lifetimes of b-flavoured hadrons, produced in the fragmentation of b quarks, are relatively
841 long; \mathcal{O} 1ps. The identification of jets origination from b quarks is very important for
842 searches for new physics and for measurements of standard model processes.

843

844 Many different algorithms developed by CMS select b-quark jets based on variables
845 such as the impact parameters of the charged-particle tracks, the properties of recon-
846 structed decay vertices, and the presence or absence of a lepton, or combinations thereof
847 [63]. One of the most efficient of which is the Combined Secondary Vertex (CSV) which
848 operates based on secondary vertex and track-based lifetime information, benchmarked
849 in ‘Loose’, ‘Medium’ and ‘Tight’ working points, of which the medium point is the tagger
850 used within the α_T search detailed in Section (4.1).

851 Using the CSV tagger, a likelihood-based discriminator distinguishes between jets
852 from b-quarks, and those from charm or light quarks and gluons, which is shown in Figure
853 3.6. The minimum thresholds on the discriminator for each working point correspond to
854 the misidentification probability for light-parton jets of 10%, 1%, and 0.1%, respectively,
855 in jets with an average p_T of about 80 GeV.

856 The b-tagging performance is evaluated to measure the b-jet tagging efficiency ϵ_b ,
857 and the misidentification probability of charm ϵ_c and light-parton jets ϵ_s . The tagging
858 efficiencies for each of these three jet flavours are compared between data and MC
859 simulation, from which a series of p_T and $|\eta|$ binned jet corrections are determined,

$$SF_{b,c,s} = \frac{\epsilon_{b,c,s}^{data}}{\epsilon_{b,c,s}^{MC}}. \quad (3.2)$$

860 These are collectively named ‘Btag Scale Factors’ and allow MC simulation to accu-
861 rately reflect the running conditions and performance of the tagging algorithm in data.
862 Understanding of the b-tagging efficiency is essential in order to minimise systematic
863 uncertainties in physics analyses that employ b-tagging.

864

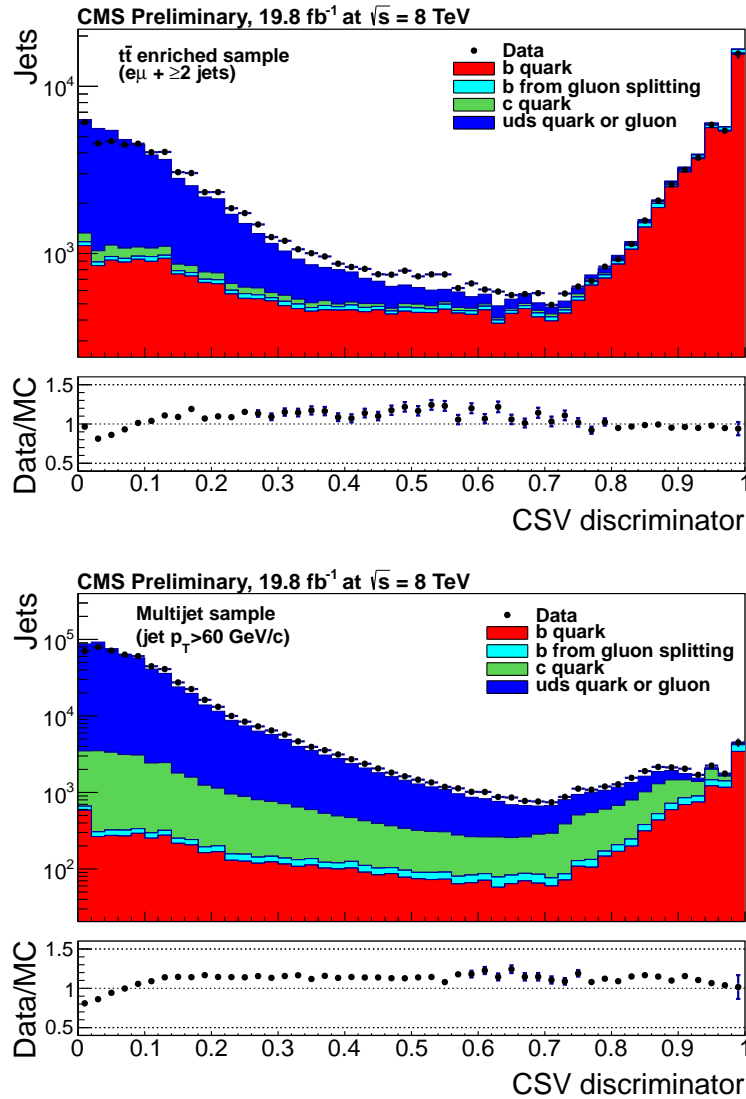


Figure 3.6.: CSV algorithm discriminator values in enriched $t\bar{t}$ bar (top) and inclusive multi jet samples (bottom) for b,c and light flavoured jets [64]. Working points are determined from the misidentification probability for light-parton jets to be tagged as a b-jet and are given as 0.244, 0.679 and 0.898 for L,M and T working points respectively.

865 The b-tagging efficiency is measured in data using several methods applied to multi
 866 jet events, primarily based on a sample of jets enriched in heavy flavour content. One
 867 method requires the collection of events with a soft muon within a cone $\Delta R < 0.4$ around
 868 the jet axis. Because the semileptonic branching fraction of b hadrons is significantly
 869 larger than that for other hadrons, these jets are more likely to arise from b quarks than
 870 from another flavour, with the resultant momentum component of the muon transverse
 871 to the jet axis larger for muons from b-hadron decays than from light or charm jets.

872 Additionally the performance of the tagger can also be benchmarked in $t\bar{t}$ events where
 873 in the SM, the top quark is expected to decay to a W boson and a b quark about 99.8%
 874 of the time [1]. Further selection criteria is applied to these events to further enrich the
 875 b quark content of these events. The methods to identify b-jets in data are discussed
 876 in great detail at [65]. The jet flavours are determined in simulation using truth level
 877 information and are compared to data to determine the correction scale factors (SF_b),
 878 which are displayed for the CSVM tagger in Figure 3.7.

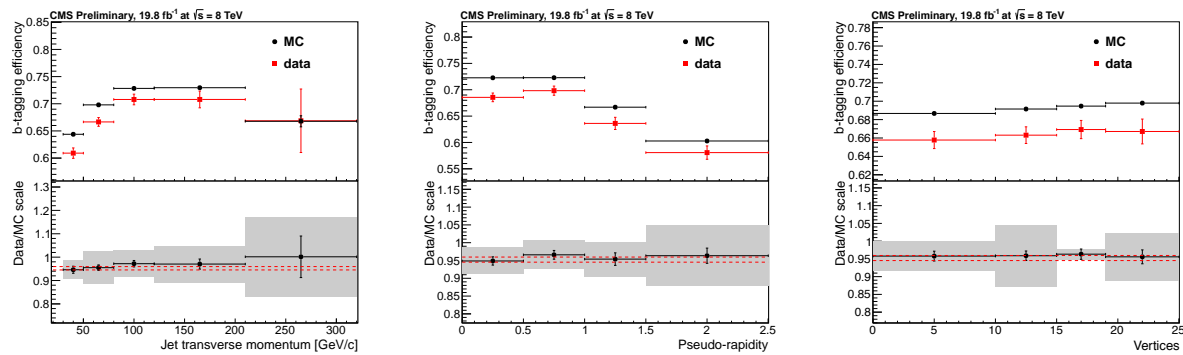


Figure 3.7.: Measured in $t\bar{t} \rightarrow \text{di-lepton}$ events using the CSVM tagger: (upper panels) b-tagging efficiencies and (lower panels) data/MC scale factor SF_b as a function of (left) jet p_T , (middle) jet $|\eta|$ and (right) number of primary vertices. In the lower panels, the grey filled areas represent the total statistical and systematic uncertainties, whereas the dotted lines are the average SF_b values within statistical uncertainties.

879 The measurement of the misidentification probability for light-parton jets relies on
 880 the inversion of tagging algorithms, selecting non-b jets using the same variables and
 881 techniques used in benchmarking the b-tagging efficiency. The scale factors (SF_s) to be
 882 applied to MC are shown in Figure 3.8 for the CSVM tagger.

883 3.4. Triggering System

884 With bunch crossings separated by just 25 ns, the rate at which data from all collisions
 885 would have to be written out and processed would be unfeasible. A two-tiered triggering
 886 system is applied at CMS in order to cope with the high collision rate of protons. The
 887 CMS trigger is designed to use limited information from each event to determine whether
 888 to record the event, reducing the rate of data taking to manageable levels whilst ensuring
 889 a high efficiency of interesting physics object events are selected.

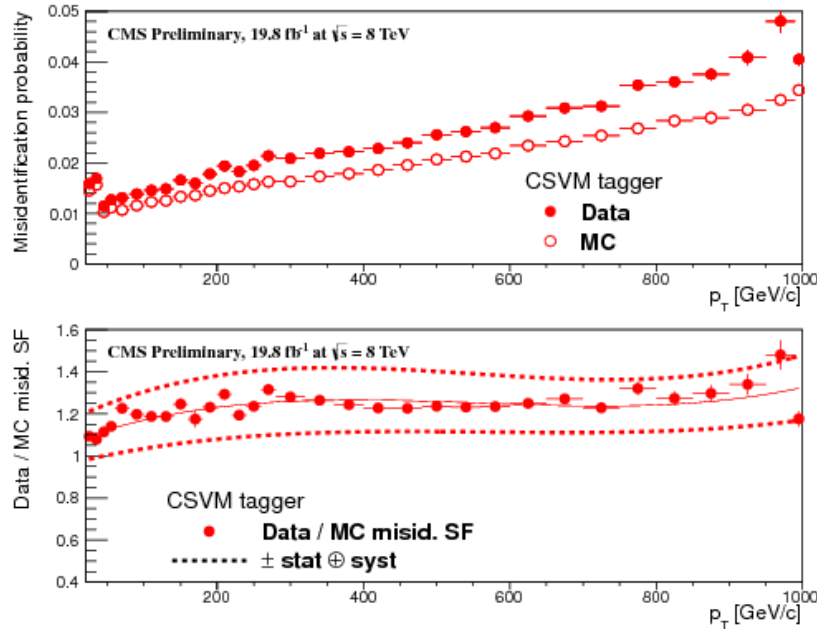


Figure 3.8.: For the **CSVM** tagging criterion: (top) misidentification probability in data (filled circles) and simulation (open circles); (bottom) scale factor for the misidentification probability. The last p_T bin in each plot includes all jets with $p_T > 1000$ GeV. The solid curve is the result of a polynomial fit to the data points. The dashed curves represent the overall statistical and systematic uncertainties on the measurements.

890 The **L1** is a pipelined, dead-timeless system based on custom-built electronics [66],
 891 and is a combination of several sub systems which is shown pictorially in Figure 3.9. The
 892 L1 system is covered in more detail within the following section along with a description
 893 of the service work undertaken by the author to benchmark the performance of the L1
 894 calorimeter trigger during the 2012 8 TeV run period.

895 The Higher Level Trigger (**HLT**) is a large farm of commercial computers [67]. The
 896 **HLT** processes events with software reconstruction algorithms that are more detailed,
 897 giving performance more similar to the reconstruction used offline. The **HLT** reduces
 898 the event rate written to disk by a factor of ~ 500 (~ 200 Hz). The recorded events are
 899 transferred from **CMS** to the **CERN** computing centre, where event reconstruction is
 900 performed, and then distributed to **CMS** computing sites around the globe for storage
 901 and analysis.

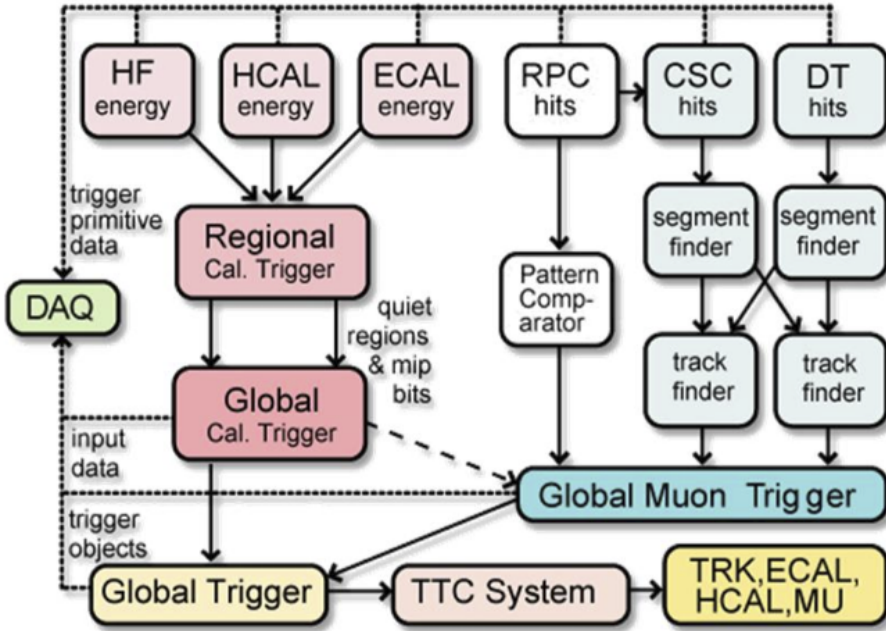


Figure 3.9.: The CMS L1 Trigger system.

3.4.1. The Level-1 Trigger

The L1 trigger reduces the rate of events collected from 40 MHz to ~ 100 kHz using information from the calorimeters and muon chambers, but not the tracker. A tree system of triggers is used to decide whether to pass on an event to the HLT for further reconstruction. Firstly the calorimeter and muon event information is kept separate, with local reconstruction of objects ($\mu, e, \gamma, \text{jets}$) performed by the Regional Calorimeter Trigger (RCT) and Regional Muon Trigger (RMT) respectively. The RCT generates up to 72 isolated and non-isolated electromagnetic objects. These are sorted by rank, which is equivalent to transverse energy E_T , with the four highest ranked electromagnetic objects being passed via the Global Calorimeter Trigger (GCT) and Global MuonTrigger (GMT) to the Global Trigger (GT).

In the L1 GCT, coarse measurements of the energy deposited in the electromagnetic and hadronic calorimeters are combined and by using sophisticated algorithms the following physics objects are formed:

- isolated and non-isolated electromagnetic objects (e and γ);
- hadronic jets in the central and forward sections of the hadronic calorimeters;

- hadronically decaying tau leptons;
- total transverse energy (E_T), the scalar sum of the energy measured at L1, and missing transverse energy (\cancel{E}_T), defined as the vector sum of the energy of L1 objects;
- total transverse jet energy (H_T), the scalar sum of the energy of all L1 jet objects, and missing transverse jet energy (\cancel{H}_T), defined as the vector sum of the energy of L1 jets, are calculated from uncorrected L1 jets.

In addition quantities suitable for triggering minimum bias events, forward physics and beam background events are calculated. Additionally relevant muon isolation information is also passed on to the **GMT** for decisions involving the muon triggers where it is combined with information from across the three muon sub-systems. The resultant final accept/reject decision at **L1** is then performed by the **GT** based on the objects received from the **GCT** and **GMT** (e/γ , μ , jets, E_T , \cancel{E}_T , H_T).

The L1 trigger is therefore of upmost importance to the functioning of the detector. Without a high-performing trigger and a good understanding of its performance, there would be no data to analyse. Observations of how the L1 trigger performance is affected by changing **LHC** running conditions over the 2012 run period and also the introduction of a jet seed threshold to the L1 jet trigger algorithm is presented in the following Sections (3.4.2 - 3.4.6).

3.4.2. L1 Trigger Jet Algorithm

The L1 jet trigger uses the transverse energy sums computed in the calorimeter (both hadronic and electromagnetic) trigger regions. Each region consists of 4×4 trigger tower windows, spanning a region of $\Delta\eta \times \Delta\phi = 0.087 \times 0.087$ in pseudorapidity-azimuth. The jet trigger uses a 3×3 calorimeter region (112 trigger towers) sliding window technique which spans the full (η, ϕ) coverage of the **CMS** calorimeter as shown in Figure 3.10.

In forming a L1 jet is it required that the central region to be higher than the eight neighbouring regions $E_{T\text{central}} > E_{T\text{surround}}$. Additionally a minimum threshold of 5 GeV on $E_{T\text{central}}$ was introduced during the 2012 run period to suppress noise from pile-up, the effects of which are shown in Section (3.4.4).

The L1 jets are characterised by the E_T , summed over the 3×3 calorimeter regions, which corresponds to 12×12 trigger towers in barrel and endcap or 3×3 larger **HF**

949 towers in the **HF**. The ϕ size of the jet window is the same everywhere, whilst the η
950 binning gets somewhat larger at high η due to calorimeter and trigger tower segmentation.
951 The jets are labelled by (η, ϕ) indexes of the central calorimeter region.

952 Jets with $|\eta| > 3.0$ are classified as forward jets, whereas those with $|\eta| < 3.0$ are
953 classified as central. The four highest energy central, forward and τ jets in the calorimeter
954 are passed through Look Up Table (**LUT**)'s, which apply a programmable η -dependent
955 jet energy scale correction. These are then used to make L1 trigger decisions.

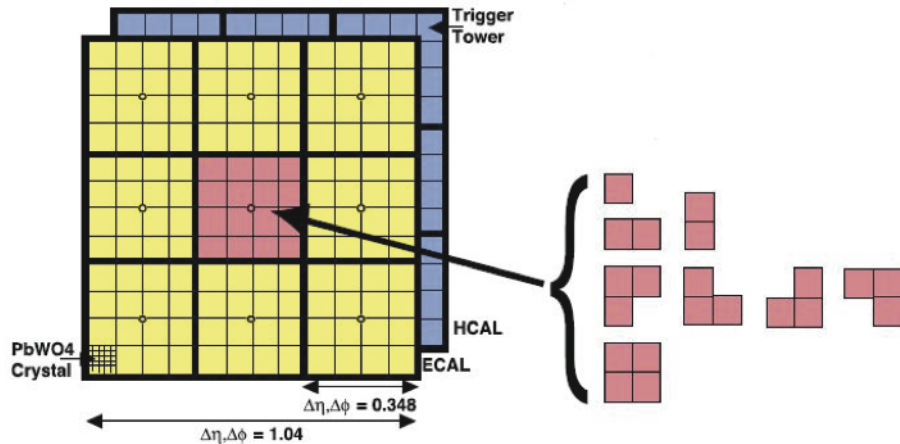


Figure 3.10.: Illustration of the Level-1 jet finding algorithm.

956 The performance of the L1 jets is evaluated with respect to offline jets, which are
957 taken from the standard Calo jet and the PF jet reconstruction algorithms of **CMS**.
958 Jets are corrected for pile-up and detector effects as described in [3.3.1](#). A moderate
959 level of noise rejection is applied to the offline jets by selecting jets passing the “loose
960 identification criteria for both Calo and PF. These criteria are summarised in Appendix
961 ([A.1](#)).

962 3.4.3. Measuring L1 Jet Trigger Efficiencies

963 The L1 jet efficiency is defined as the fraction of leading offline jets which were matched
964 with a L1 tau or central jet above a certain trigger threshold, divided by all the leading
965 offline jets in the event. This quantity is then plotted as a function of the offline jet E_T ,
966 η and ϕ .

967 The efficiency is determined by matching the L1 and reconstructed offline jets spatially
968 in $\eta - \phi$ space. This is done by calculating the minimum separation in ΔR between the

969 highest offline reconstructed jet in E_T ($E_T > 10$ GeV, $|\eta| < 3$) and any L1 jet. A jet will
970 be matched if this value is found to be < 0.5 . Should more than one jet satisfy this, the
971 jet closest in ΔR is taken as the matched jet. The matching efficiency is close to 100%,
972 above ? 30(45) GeV for run 2012B(C) data (see Appendix (??)).

973 Each efficiency curve is fitted with a function which is the cumulative distribution
974 function of an Exponentially Modified Gaussian (EMG) distribution:

$$\text{f}(x; \mu, \sigma, \lambda) = \frac{\lambda}{2} \cdot e^{\frac{\lambda}{2}(2\mu + \lambda\sigma^2 - 2x)} \cdot \text{erfc}\left(\frac{\mu + \lambda\sigma^2 - x}{\sqrt{2}\sigma}\right) \quad (3.3)$$

where erfc is the complementary error function defined as:

$$\text{erfc}(x) = 1 - \text{erf}(x) = \frac{2}{\sqrt{\pi}} \int_x^\infty e^{-t^2} dt.$$

976 In this functional form, the parameter μ determines the point of 50% of the plateau
977 efficiency and the σ gives the resolution. This parametrisation is used to benchmark
978 the efficiency at the plateau, the turn-on points and resolution for each L1 Jet trigger.
979 The choice of function is purely empirical. Previous studies used the error function
980 alone, which described the data well at high threshold values but could not describe the
981 efficiencies well at lower thresholds [68].

982 The efficiency turn-on curves for various L1 jet thresholds are evaluated as a function
983 of the offline reconstructed jet E_T for central jets with $|\eta| < 3$. These are measured using
984 single isolated μ triggers which have high statistics, and are orthogonal and therefore
985 unbiased to the hadronic triggers under study. The efficiency is calculated with respect to
986 offline Calo and PF Jets in Figure 3.11. Table 3.1 shows the values of these parameters,
987 calculated for three example L1 single jet triggers taken from 2012 8 TeV data.

988 The results from the L1 single jet triggers shows good performance for both Calo and
989 PF jets. A better resolution for Calo jets with respect to L1 jets quantities is observed.
990 This effect is due to Calo jet reconstruction using the same detector systems as in L1 jets,
991 whereas with PF jet construction using tracker and muon information, a more smeared
992 resolution when compared to L1 is expected.

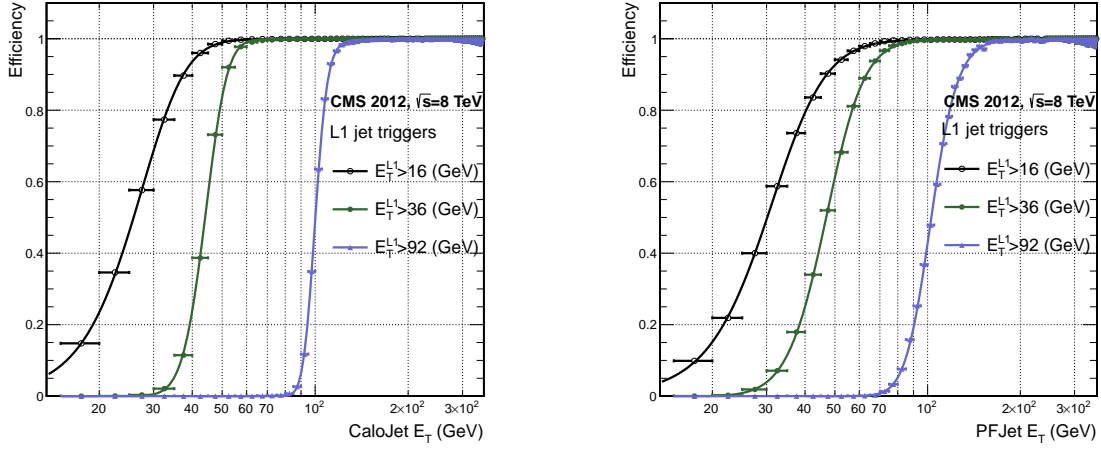


Figure 3.11.: L1 jet efficiency turn-on curves as a function of the offline CaloJet E_T (left) and PFJet E_T (right), measured in 2012 Run Period C data and collected with an isolated single μ data sample.

Trigger	Calo		PF	
	μ	σ	μ	σ
L1_SingleJet16	21.09 ± 0.03	7.01 ± 0.02	22.17 ± 0.04	7.83 ± 0.03
L1_SingleJet36	41.15 ± 0.05	5.11 ± 0.02	39.16 ± 0.06	8.04 ± 0.03
L1_SingleJet92	95.36 ± 0.13	5.62 ± 0.03	90.85 ± 0.19	11.30 ± 0.10

Table 3.1.: Results of a cumulative EMG function fit to the turn-on curves for L1 single jet triggers in run 2012 Run Period C, measured in an isolated μ data sample. The turn-on point, μ , and resolution, σ , of the L1 jet triggers are measured with respect to offline Calo Jets (left) and PF Jets (right).

3.4.4. Effects of the L1 Jet Seed

Between run period B and C of the 2012 data taking period, a jet seed threshold was introduced into the L1 trigger jet algorithm. There was previously no direct requirement made on the energy deposited in the central region. The introduction of a jet seed threshold required that the central region have $E_T \geq 5\text{GeV}$, and was introduced to counteract the effects of high pile up running conditions which create a large number of soft non-collimated jets, that are then added to the jets from the primary interaction or other soft jets from other secondary interactions [69]. This in turn causes a large increase in trigger rate due to the increase in the likelihood that the event causes the L1 trigger to fire. This was implemented to maintain trigger thresholds by cutting the rate of events recorded without significant reduction in the efficiency of physics events of interest.

1004 The effect of the introduction of this jet seed threshold between these two run periods
 1005 is benchmarked through a comparison of the efficiency of the L1 jet triggers with respect
 1006 to offline Calo jets shown in Figure 3.12, and the L1 H_T trigger efficiency in Figure 3.14
 1007 which is compared to offline H_T constructed from Calo jets with $E_T \geq 40\text{GeV}$.

1008 To negate any effects from different pile-up conditions in the run periods, the efficiencies
 1009 are measured in events which contain between 15 and 20 primary vertices as defined in
 1010 Appendix (A.2).

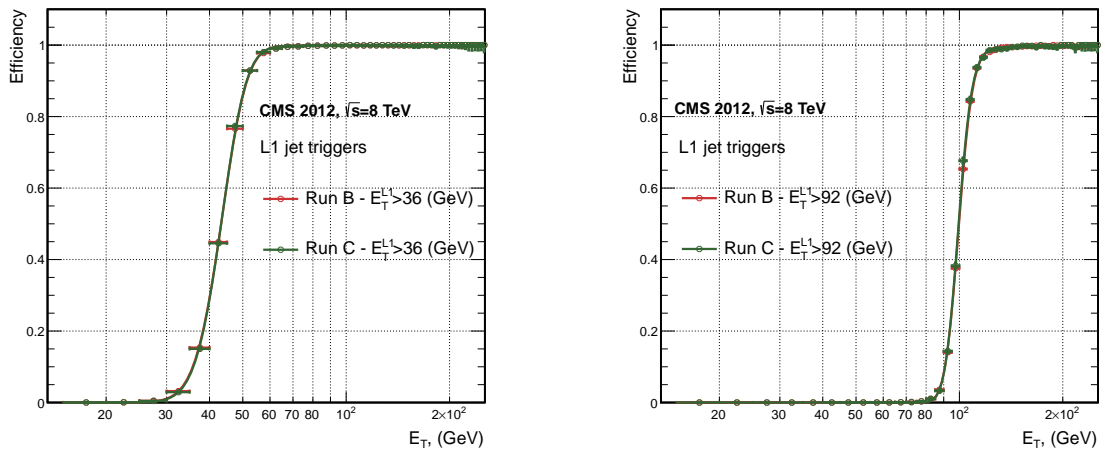


Figure 3.12.: L1 jet efficiency turn-on curves as a function of the offline CaloJet E_T , measured for the L1 SingleJet 36 and 92 trigger in 2012 run period B and C collected with an isolated single μ' sample.

1011 It can be seen that the performance of the $E_T > 36, 92$ single jet are almost identical,
 1012 with the jet seed having no measurable effect on these triggers as shown in Table 3.2 .

Trigger	2012B		2012C	
	μ	σ	μ	σ
L1_SingleJet36	40.29 ± 0.04	5.34 ± 0.02	40.29 ± 0.11	5.21 ± 0.05
L1_SingleJet92	94.99 ± 0.09	5.93 ± 0.06	94.82 ± 0.29	5.74 ± 0.18

Table 3.2.: Results of a cumulative EMG function fit to the turn-on curves for L1 single jet triggers in the 2012 run period B and C, preselected on an isolated muon trigger. The turn-on point μ and resolution σ of the L1 jet triggers are measured with respect to offline Calo Jets in run B (left) and run C (right).

1013 For the H_T triggers, a large increase in rate during high pile-up conditions is expected.
 1014 This is due to the low energy threshold required for a jet to be added to the L1 H_T sum,

which is compiled from all uncorrected L1 jets formed in the RCT. The introduction of the jet seed threshold removes the creation of many of these soft low E_T jets, thus lowering the H_T calculation at L1. The effect on the trigger cross section for L1 H_T 150 trigger can be seen in Figure 3.13.

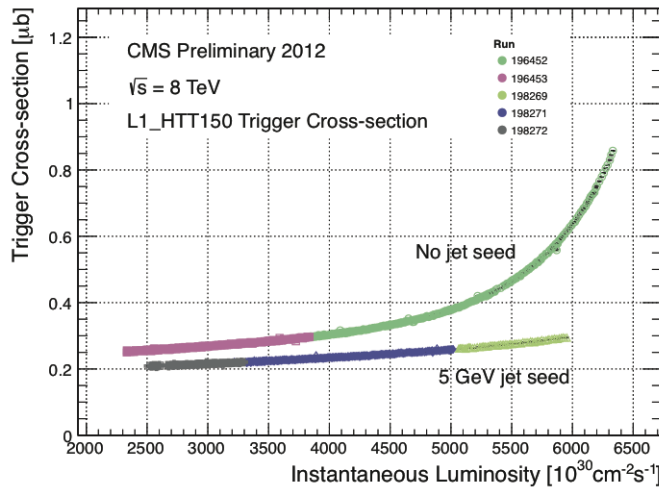


Figure 3.13.: Trigger cross section for the L1HTT150 trigger path. Showing that a 5 GeV jet seed threshold dramatically reduces the dependance of cross section on the instantaneous luminosity for L1 H_T triggers [70].

Different behaviours for the trigger turn ons between these run periods are therefore expected. The turn on point is observed to shift to higher H_T values after the introduction of the jet seed threshold, whilst having a sharper resolution due to less pile-up jets being included the H_T sum, the results are shown in Table 3.3.

Trigger	2012B		2012C	
	μ	σ	μ	σ
L1 HT-100	157.5 ± 0.08	32.9 ± 0.08	169.8 ± 0.08	28.7 ± 0.03
L1 H1-150	230.9 ± 0.02	37.3 ± 0.01	246.4 ± 0.16	31.8 ± 0.05

Table 3.3.: Results of a cumulative EMG function fit to the turn-on curves for H_T in run 2012 B and C, preselected on an isolated single μ trigger. The turn-on point μ , resolution σ of the L1 H_T triggers are measured with respect to offline H_T formed from CaloJets with a $E_T \geq 40$ in run period B (left) and C (right).

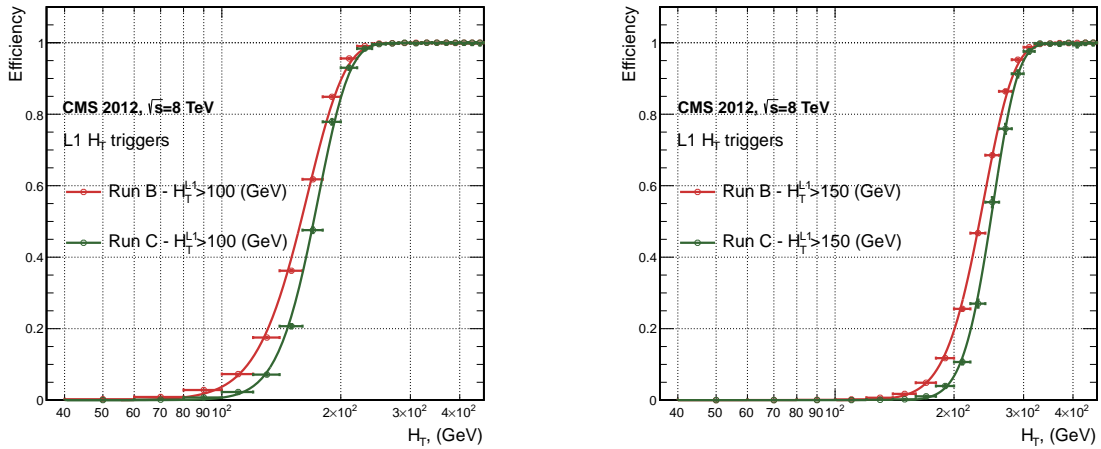


Figure 3.14.: L1 H_T efficiency turn-on curves as a function of the offline CaloJet H_T , measured for the L1 H_T 100 and 150 trigger during the run 2012 B and C collected using an isolated single μ triggered sample.

1023 3.4.5. Robustness of L1 Jet Performance against Pile-up

1024 The performance of the L1 single jet triggers is evaluated in different pile-up conditions
1025 to benchmark any dependence on pile-up. Three different pile-up bins of 0-10, 10-20 and
1026 >20 vertices are defined, reflecting the low, medium and high pile-up running conditions
1027 at CMS in 2012. This is benchmarked relative to Calo and PF jets for the run 2012 C
1028 period where the jet seed threshold is applied, with L1 single jet thresholds of 16, 36 and
1029 92 GeV, shown in Figure 3.15. The results of fits to these efficiency turn-on curves are
1030 given in Table 3.4 and Table 3.5 for Calo and PF jets respectively.

Vertices	0-10		11-20		> 20	
	μ	σ	μ	σ	μ	σ
L1_SingleJet16	19.9 ± 0.1	6.1 ± 0.3	20.8 ± 0.1	6.5 ± 0.1	22.3 ± 0.2	7.5 ± 0.1
L1_SingleJet36	41.8 ± 0.1	4.6 ± 0.1	40.9 ± 0.1	5.1 ± 0.1	40.6 ± 0.6	5.9 ± 0.2
L1_SingleJet92	95.9 ± 0.2	5.4 ± 0.1	95.2 ± 0.2	5.6 ± 0.1	94.5 ± 0.6	6.2 ± 0.3

Table 3.4.: Results of a cumulative EMG function fit to the efficiency turn-on curves for L1 single jet triggers in the 2012 run period C, measured from isolated μ triggered data. The turn-on point, μ , and resolution, σ , of the L1 jet triggers are measured with respect to offline Calo jets in low (left), medium (middle) and high (right) pile-up conditions.

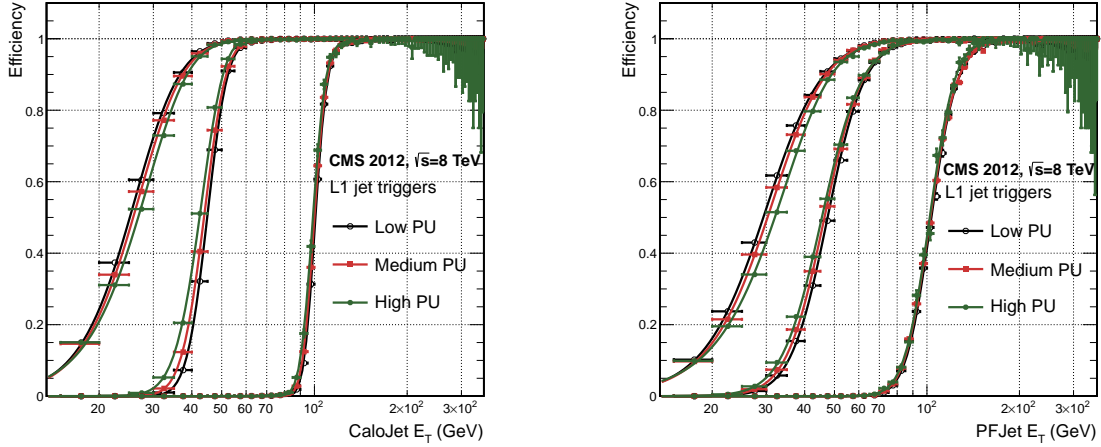


Figure 3.15.: L1 jet efficiency turn-on curves as a function of the leading offline E_T Calo (left) and PF (right) jet, for low, medium and high pile-up conditions.

Vertices	0-10		11-20		> 20	
	μ	σ	μ	σ	μ	σ
L1_SingleJet16	21.1 ± 0.1	7.16 ± 0.05	22.34 ± 0.1	7.9 ± 0.1	24.6 ± 0.2	9.5 ± 0.1
L1_SingleJet36	39.6 ± 0.1	7.4 ± 0.1	38.4 ± 0.1	7.4 ± 0.1	37.1 ± 0.2	7.5 ± 0.1
L1_SingleJet92	91.6 ± 0.3	11.3 ± 0.2	90.4 ± 0.3	11.2 ± 0.1	92.0 ± 0.9	12.1 ± 0.4

Table 3.5.: Results of a cumulative EMG function fit to the efficiency turn-on curves for Level-1 single jet triggers in the 2012 run period C, measured from isolated μ triggered data. The turn-on point, μ , and resolution, σ , of the L1 jet triggers are measured with respect to offline PF jets in low (left), medium (middle) and high (right) pile-up conditions.

1031 No significant drop in efficiency is observed in the presence of a high number of
 1032 primary vertices. The increase in hadronic activity in higher pile-up conditions, combined
 1033 with the absence of pile-up subtraction for L1 jets, results in the expected observation of
 1034 a decrease in the μ value of the efficiency turn-ons as a function of pile-up, while the
 1035 resolution, σ of the turn-ons are found to gradually worsen as expected with increasing
 1036 pile-up.

1037 These features are further emphasised when shown as a function of

$$\frac{(L1 E_T - Offline E_T)}{Offline E_T} \quad (3.4)$$

in bins of matched leading offline jet E_T , of which the individual fits can be found in Appendix (B.2). Each of these distributions are fitted with an EMG function as defined in Equation (3.3).

The μ , σ and λ values extracted for the low, medium and high pile-up conditions are shown for Calo and PF jets in Figure 3.16 and Figure 3.17 respectively. The central value of $\frac{(L1 E_T - \text{Offline } E_T)}{\text{Offline } E_T}$ is observed to increases as a function of jet E_T , whilst the resolution is also observed to improve at higher offline jet E_T .

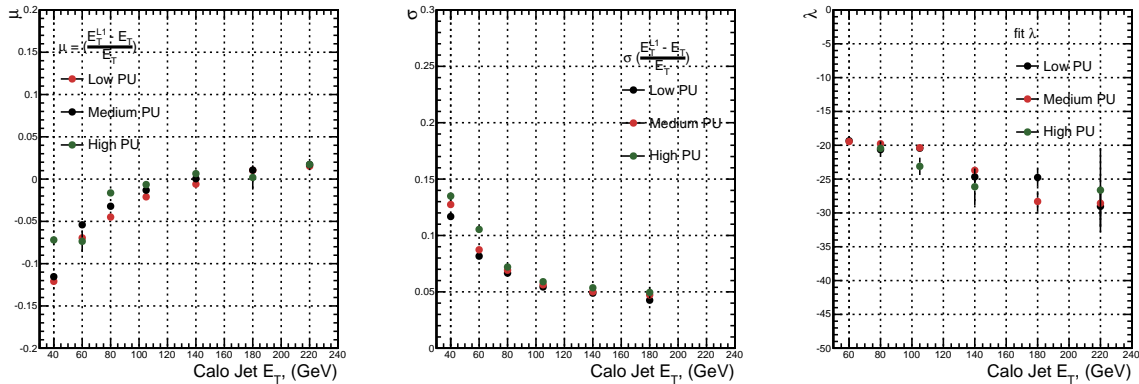


Figure 3.16.: Fit values from an EMG function fitted to the resolution plots of leading Calo jet E_T measured as a function of $\frac{(L1 E_T - \text{Offline } E_T)}{\text{Offline } E_T}$ for low, medium and high pile-up conditions. The plots show the mean μ (left), resolution σ (middle) of the Gaussian as well as the decay term λ (right) of the exponential.

The resolution of other L1 energy sum quantities, H_T , \not{E}_T and $\sum E_T$ parameterised as in Equation (3.4), can be found in Appendix (B.3). The same behaviour observed for the single jet triggers is also found for these quantities, where in the presence of higher pile-up the μ values are shifted to higher values, with a worsening resolution, σ again due to the increase in soft pile-up jets and the absence of pile-up subtraction at L1.

3.4.6. Summary

The performance of the CMS Level-1 Trigger has been studied and evaluated for jets and energy sum quantities using data collected during the 2012 LHC 8TeV run. These studies include the effect of introduction of a 5 GeV jet seed threshold into the jet algorithm configuration, the purpose of which is to mitigate the effects of pile-up on the rate of L1 triggers whilst not adversely affecting the efficiency of these triggers. No significant

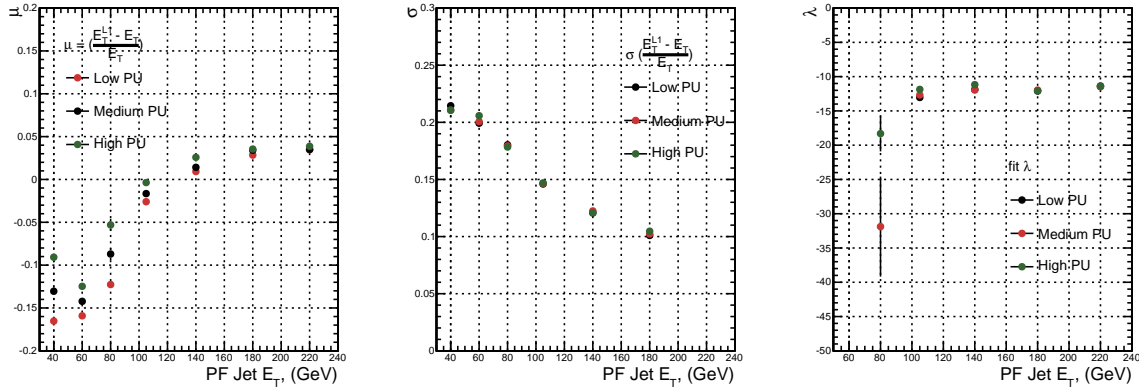


Figure 3.17.: Fit values from an **EMG** function fitted to the resolution plots of leading PF jet E_T measured as a function of $\frac{(L1\ E_T - \text{Offline}\ E_T)}{\text{Offline}\ E_T}$ for low and medium pile-up conditions. The plots show the mean μ (left), resolution σ (middle) of the Gaussian as well as the decay term λ (right) of the exponential.

1056 change in performance is observed with this change and good performance is observed
 1057 for a range of L1 quantities.

Chapter 4.

¹⁰⁵⁸ SUSY searches in Hadronic Final

¹⁰⁵⁹ States

¹⁰⁶⁰ In this chapter a model independent search for **SUSY** in hadronic final states with \cancel{E}_T
¹⁰⁶¹ using the α_T variable and b-quark multiplicity is introduced and described in detail. The
¹⁰⁶² results presented are based on a data sample of pp collisions collected in 2012 at $\sqrt{s} = 8$
¹⁰⁶³ TeV, corresponding to an integrate luminosity of $11.7 \pm 0.5 \text{ fb}^{-1}$.

¹⁰⁶⁴ The kinematic variable α_T is motivated as a variable to provide strong rejections
¹⁰⁶⁵ of QCD backgrounds, whilst maintaining sensitivity to possible a **SUSY** signal within
¹⁰⁶⁶ Section (4.1). The search and trigger strategy in addition to the event reconstruction
¹⁰⁶⁷ and selection are outlined within Sections (4.2-4.2.2).

¹⁰⁶⁸ The method in which the **SM** background is estimated using an analytical technique
¹⁰⁶⁹ to improve statistical precision at higher b-tag multiplicities is detailed within Section
¹⁰⁷⁰ (4.4), with a discussion on the impact of b-tagging and mis-tagging scale factors between
¹⁰⁷¹ data and MC on any background predictions. Finally a description of the formulation of
¹⁰⁷² appropriate systematic uncertainties applied to the background predictions to account for
¹⁰⁷³ theoretical uncertainties and limitations in the simulation modelling of event kinematics
¹⁰⁷⁴ and instrumental effects is covered in Section (4.6).

¹⁰⁷⁵ In addition to the α_T search, a complimentary technique is discussed as a means to
¹⁰⁷⁶ predict the distribution of 3 and 4 reconstructed b-quark jets in an event in Section
¹⁰⁷⁷ (4.7). The recent discovery of the Higgs boson has made third-generation “Natural **SUSY**”
¹⁰⁷⁸ models attractive, given that light top and bottom squarks are a candidate to stabilise
¹⁰⁷⁹ divergent loop corrections to the Higgs boson mass.

Using the α_T search as a base, a simple templated fit is employed to estimate the SM background in higher b-tag multiplicities (3-4) from a region of a low number of reconstructed b-jets (0-2). The predictions using this technique are first tested in simulation before being compared to the SM background predictions obtained from the α_T search.

The experimental reach of the analysis discussed within this thesis is interpreted in two classes of SMS models, the topologies of which are detailed in Section (2.4.1). The SMS models considered in this analysis are summaries in Table 4.1. For each model, the LSP is assumed to be the lightest neutralino.

Within Table 4.1 is also defined reference points, parameterised in terms of parent gluino/squark and LSP sparticle masses, m_{parent} and m_{LSP} , respectively, which are used within the following two chapters to demonstrate potential yields within the signal region of the search. The masses are chosen to reflect parameter space which is within the expect sensitivity reach of the search.

Model	Production/decay mode	Reference model	
		m_{parent}	m_{LSP}
G1 (T1)	$pp \rightarrow \tilde{g}\tilde{g}^* \rightarrow q\bar{q}\tilde{\chi}_1^0 q\bar{q}\tilde{\chi}_1^0$	700	300
G2 (T1bb)	$pp \rightarrow \tilde{g}\tilde{g}^* \rightarrow b\bar{b}\tilde{\chi}_1^0 b\bar{b}\tilde{\chi}_1^0$	900	500
G3 (T1tt)	$pp \rightarrow \tilde{g}\tilde{g}^* \rightarrow t\bar{t}\tilde{\chi}_1^0 t\bar{t}\tilde{\chi}_1^0$	850	250
D1 (T2)	$pp \rightarrow \tilde{q}\tilde{q}^* \rightarrow q\tilde{\chi}_1^0 \bar{q}\tilde{\chi}_1^0$	600	250
D2 (T2bb)	$pp \rightarrow \tilde{b}\tilde{b}^* \rightarrow b\tilde{\chi}_1^0 \bar{b}\tilde{\chi}_1^0$	500	150
D3 (T2tt)	$pp \rightarrow \tilde{t}\tilde{t}^* \rightarrow t\tilde{\chi}_1^0 \bar{t}\tilde{\chi}_1^0$	400	0

Table 4.1.: A summary of the SMS models interpreted in this analysis, involving both direct (D) and gluino-induced (G) production of squarks and their decays. Reference models are also defined in terms of parent and LSP sparticle mass

4.1. An introduction to the α_T search

The experimental signature of SUSY signal in the hadronic channel would manifest as a final state containing energetic jets and \cancel{E}_T . The search focuses on topologies where new heavy supersymmetric, R-parity conserving particles are pair-produced in pp collisions. These particles decaying to a LSP escape the detector undetected, leading to significant missing energy and missing hadronic transverse energy,

$$\mathcal{H}_T = \left| \sum_{i=1}^n p_T^{jet_i} \right|, \quad (4.1)$$

1100 defined as the vector sum of the transverse energies of jets selected in an event.
1101 Energetic jets produced in the decay of these supersymmetric particles also can produce
1102 significant visible transverse energy,

$$H_T = \sum_{i=1}^n E_T^{jet_i}, \quad (4.2)$$

1103 defined as the scalar sum of the transverse energies of jets selected in an event.

1104 A search within this channel is greatly complicated in a hadron collider environment,
1105 where the overwhelming background comes from inherently balanced multi-jet (“QCD”)
1106 events which are produced with an extremely large cross section as demonstrated within
1107 Figure 4.1. \cancel{E}_T can appear in such events with a substantial mis-measurement of jet
1108 energy or missed objects due to detector miscalibration or noise effects.

1109 Additional **SM** background from **EWK** processes with genuine \cancel{E}_T from escaping
1110 neutrinos comprise the irreducible background within this search and come mainly from:

- 1111 • $Z \rightarrow \nu\bar{\nu}$ + jets,
- 1112 • $W \rightarrow l\nu$ + jets in which a lepton falls outside of detector acceptance, or the lepton
1113 decays hadronically $\tau \rightarrow \text{had}$,
- 1114 • $t\bar{t}$ with at least one leptonic W decay,
- 1115 • small background contributions from DY, single top and Diboson (WW,ZZ,WZ)
1116 processes.

1117 The search is designed to have a strong separation between events with genuine and
1118 “fake” \cancel{E}_T which is achieved primarily through the dimensionless kinematic variable, α_T
1119 [71][72].

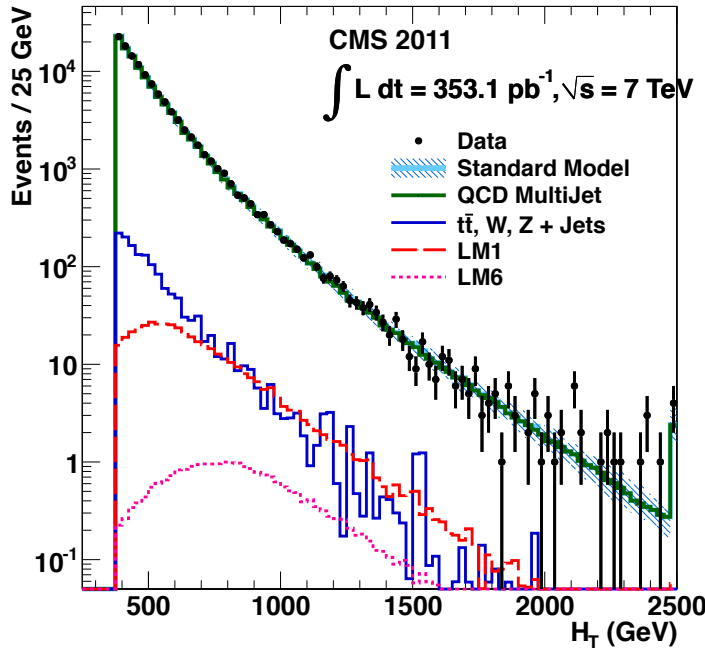


Figure 4.1.: Reconstructed offline H_T for 11.7fb^{-1} of data after a basic pre-selection. Sample is collected from prescaled H_T triggers. Overlaid are expectations from MC simulation of EWK processes as well as a reference signal model (labelled D2 from Table 4.1).

1120 4.1.1. The α_T variable

1121 For a perfectly measured di-jet QCD event, conservation laws dictate that they must be
 1122 produced back-to-back and of equal magnitude. However in di-jet events with real \cancel{E}_T ,
 both of these jets are produced independently of one another, depicted in Figure 4.2.

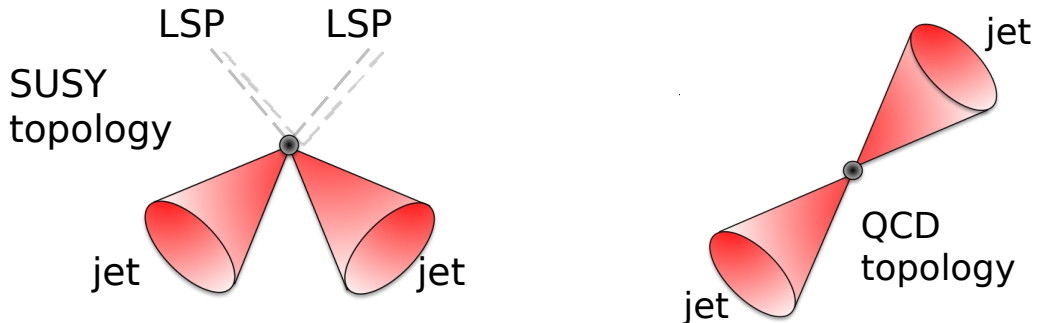


Figure 4.2.: The event topologies of background QCD dijet events (right) and a generic SUSY signature with genuine \cancel{E}_T (left).

1124 Exploiting this feature leads to the formulation of α_T in di-jet systems defined as,

$$\alpha_T = \frac{E_T^{j2}}{M_T}, \quad (4.3)$$

1125 where E_T^{j2} is the transverse energy of the least energetic of the two jets and M_T
1126 defined as:

$$M_T = \sqrt{\left(\sum_{i=1}^2 E_T^{ji}\right)^2 - \left(\sum_{i=1}^2 p_x^{ji}\right)^2 - \left(\sum_{i=1}^2 p_y^{ji}\right)^2} \equiv \sqrt{H_T^2 - \cancel{H}_T^2}. \quad (4.4)$$

1127 A perfectly balanced di-jet event i.e. $E_T^{j1} = E_T^{j2}$ would give an $\alpha_T = 0.5$, where as
1128 events with jets which are not back-to-back, for example in events in which a W or Z
1129 recoils off a system of jets, α_T can achieve values in excess of 0.5.

1130 α_T can be extended to apply to any arbitrary number of jets, undertaken by modelling
1131 a system of n jets as a di-jet system, through the formation of two pseudo-jets [73].
1132 The two pseudo-jets are built by merging the jets present in the event such that the 2
1133 pseudo-jets are chosen to be as balanced as possible, i.e the $\Delta H_T \equiv |E_T^{pj1} - E_T^{pj2}|$ is
1134 minimised between the two pseudo jets. Using Equation (4.4), α_T can be rewritten as,

$$\alpha_T = \frac{1}{2} \frac{H_T - \Delta H_T}{\sqrt{H_T^2 - \cancel{H}_T^2}} = \frac{1}{2} \frac{1 - \Delta H_T/H_T}{\sqrt{1 - (\cancel{H}_T/H_T)^2}}. \quad (4.5)$$

1135 The distribution of α_T for the two jet categories used within this analysis, 2,3 and
1136 ≥ 4 jets, is shown in the Figure 4.3, demonstrating the ability of the α_T variable to
1137 discriminate between multi jet events and EWK processes with genuine \cancel{E}_T in the final
1138 state.

1139 The α_T requirement used within the search is chosen to be $\alpha_T > 0.55$ to ensure
1140 that the QCD multijet background is negligible even in the presence of moderate jet
1141 mis-measurement. There still remains other effects which can cause multijet events to
1142 artificially have a large α_T value, which are discussed in detail in Section (4.2.2).

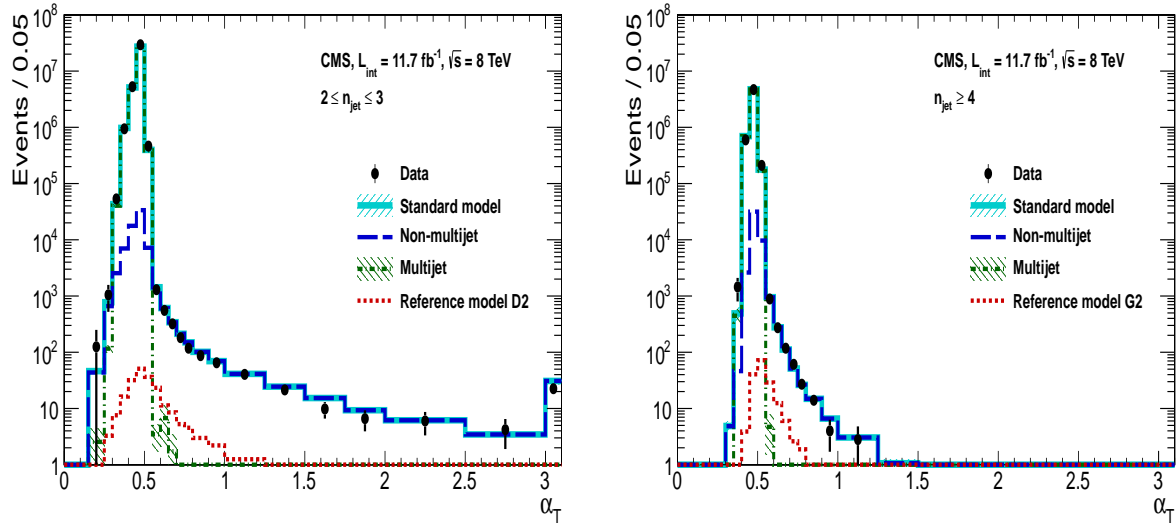


Figure 4.3.: The α_T distributions for the low 2-3 (left) and high ≥ 4 (right) jet multiplicities after a full analysis selection and shown for $H_T > 375$. Data is collected using both prescaled H_T triggers and dedicated α_T triggers for below and above $\alpha_T = 0.55$ respectively. . Expected yields as given by simulation are also shown for multijet events (green dash-dotted line), EWK backgrounds with genuine \cancel{E}_T (blue long-dashed line), the sum of all SM processes (cyan solid line) and the reference signal model D2 (left, red dotted line) or G2 (right, red dotted line).

1143 4.2. Search Strategy

1144 The aim of the analysis presented in this thesis is to identify an excess of events in data
 1145 over the SM background expectation in multi-jet final states and significant \cancel{E}_T . The
 1146 essential suppression of the dominant QCD background for such a search is addressed by
 1147 the α_T variable described in the previous section. For estimation of the remaining EWK
 1148 backgrounds, three independent data control samples are used to predict the different
 1149 processes that compose the background :

- 1150 • $\mu + \text{jets}$ to determine $W + \text{jets}$, $t\bar{t}$ and single top backgrounds,
- 1151 • $\gamma + \text{jets}$ to determine the irreducible $Z \rightarrow \nu\bar{\nu} + \text{jets}$ background,
- 1152 • $\mu\mu + \text{jets}$ to determine the irreducible $Z \rightarrow \nu\bar{\nu} + \text{jets}$ background.

1153 These control samples are chosen to both be rich in specific EWK processes, be free of
 1154 QCD multi-jet events and to also be kinematically similar to the hadronic signal region
 1155 that they are estimating the backgrounds of, see Section (4.2.3).

1156 To remain inclusive to a large range of possible **SUSY** models, the signal region is
1157 binned in the following categories to allow for increased sensitivity in the interpretation
1158 of results for different **SUSY** topologies:

1159 **Sensitivity to a range of SUSY mass splittings**

1160 The hadronic signal region is defined by $H_T > 275$, divided into eight bins in H_T .

- 1161 – Two bins of width 50 GeV in the range $275 < H_T < 375$ GeV,
1162 – five bins of width 100 GeV in the range $375 < H_T < 875$ GeV,
1163 – and a final open bin, $H_T > 875$ GeV.

1164 The choice at low H_T is driven primarily by trigger constraints. The mass difference
1165 between the **LSP** and the particle that it decays from is an important factor in the
1166 amount of hadronic activity in the event.

1167 A large mass splitting will lead to hard high p_T jets which contribute to the H_T
1168 sum. From Figure 4.1 it can be seen that the **SM** background falls sharply at high
1169 H_T values, therefore a large number of H_T bins will lead to easier identification
1170 of such signals. Conversely smaller mass splittings lead to softer jet p_T 's which will
1171 subsequently fall into the lower H_T range.

1172 **Sensitivity to production method of SUSY particles**

1173 The production mechanism of any potential **SUSY** signal can lead to different event
1174 topologies. One such way to discriminate between gluino ($g\tilde{g}$ - “high multiplicity”),
1175 and direct squark ($q\tilde{q}$ - “low multiplicity”) induced production of **SUSY** particles is
1176 realised through the number of reconstructed jets in the final state.

1177 The analysis is thus split into two jet categories : 2-3 jets , ≥ 4 jets to give sensitivity
1178 to both of these mechanisms.

1179 **Sensitivity to “Natural SUSY” via tagging jets from b-quarks**

1180 Jets originating from bottom quarks (b-jets) are identified through vertices that
1181 are displaced with respect to the primary interaction. The algorithm used to tag
1182 b-jets is the Combined Secondary Vertex Medium Working Point (**CSV**) tagger,
1183 described within Section (3.3.2). A cut is placed on the discriminator variable of
1184 > 0.679 , leading to a gluon/light-quark mis-tag rate of 1% and a jet p_T dependant
1185 b-tagging efficiency of 60-70% [64].

1186 Natural **SUSY** models would be characterised through final-state signatures rich
 1187 in bottom quarks. A search relying on methods to identify jets originating from
 1188 bottom quarks through b-tagging, will significantly improve the sensitivity to this
 1189 class of signature.

1190 This is achieved via the binning of events in the signal region according to the
 1191 number of b-tagged jets reconstructed in each event, in the following: 0,1,2,3, ≥ 4
 1192 b-tag categories . In the highest ≥ 4 b-tag category due to a limited number of
 1193 expected signal and background, just three H_T bins are employed: 275-325 GeV,
 1194 325-375 GeV, ≥ 375 GeV.

1195 This characterisation is identically mirrored in all control samples, with the infor-
 1196 mation from all samples and b-tag categories used simultaneously in the likelihood
 1197 model (see Chapter 5) in order to interpret the results in a coherent and powerful
 1198 way.

1199 The combination of the H_T , jet multiplicity and b-tag categorisation of the signal
 1200 region as described above, resultantly leads to 67 different bins in which the analysis is
 1201 interpreted in, which is depicted in Figure 4.4.

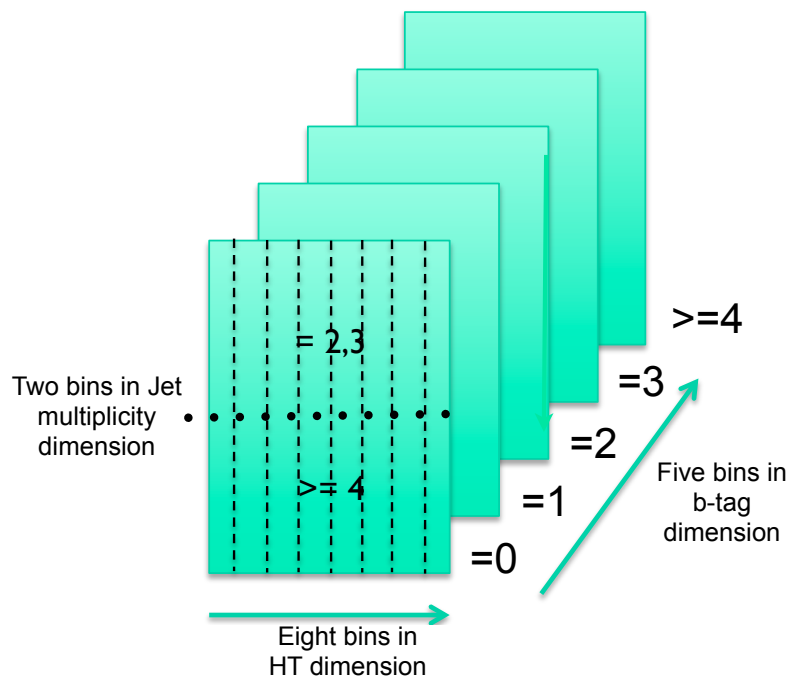


Figure 4.4.: Pictorial depiction of the analysis strategy employed by the α_T search to increase sensitivity to a wide spectra of **SUSY** models.

1202 **4.2.1. Physics Objects**

1203 The physics objects used in the analysis defined below, follow the recommendation of
1204 the various CMS Physics Object Groups ([POGs](#)).

1205 • **Jets**

1206 The jets used in this analysis are CaloJets, reconstructed as described in Section
1207 ([3.3.1](#)) using the anti- k_T jet clustering algorithm.

1208 To ensure the jet object falls within the calorimeter systems a pseudo-rapidity
1209 requirement of $|\eta| < 3$ is applied. Each jet must pass a “loose” identification criteria
1210 to reject jets resulting from unphysical energy, the criteria of which are detailed in
1211 Table [4.2](#) [[74](#)].

Variable	Definition
$f_{HPD} < 0.98$	Fraction of jet energy contributed from “hottest” HPD , which rejects HCAL noise.
$f_{EM} > 0.01$	Noise from the HCAL is further suppressed by requiring a minimal electromagnetic component to the jet f_{EM} .
$N_{hits}^{90} \geq 2$	Jets that have $> 90\%$ of its energy from a single channel are rejected, to serve as a safety net that catches jets arising from undiagnosed noisy channels.

Table 4.2.: Jet Identification criteria for the “loose” CaloJet ID, used to reject reconstructed jets resulting from fake calorimeter deposits representing unphysical energy.

1212 • **Muons**

1213 Muons are selected in the $\mu +$ jets and $\mu\mu +$ jets control samples, and vetoed in
1214 the signal region. The same cut based identification criteria is applied to muons in
1215 both search regions and is summarised in Table [4.3](#) [[75](#)].

1216 Additionally muons are required to be within the acceptance of the muon tracking
1217 systems. For the muon control samples, trigger requirements necessitate a $|\eta| <$
1218 2.1 for the selection of muons. In the signal region where muons are vetoed these
1219 conditions are relaxed to $|\eta| < 2.5$ and a minimum threshold of $p_T > 10$ GeV is
1220 required of muon objects.

1221 • **Photons**

Categories	Criteria
Global Muon	True
PFMuon	True
χ^2	< 10
Muon chamber hits	> 0
Muon station hits	> 1
Transvere impact d_{xy}	< 0.2mm
Longitudinal distance d_z	< 0.5mm
Pixel hits	> 0
Track layer hits	> 5
PF Isolation (DeltaB corrected)	<0.12

Table 4.3.: Muon Identification criteria used within the analysis for selection/veto purposes in the muon control/signal selections.

1222 Photons are selected within the $\gamma +$ jets control sample and vetoed in all other
1223 selections. Photons are identified in both cases according to the cut based criteria
1224 listed in Table 4.4 [76].

Variable	Definition
$H/E < 0.05$	The ratio of hadronic energy in the HCAL tower directly behind the ECAL super-cluster and the ECAL super-cluster itself.
$\sigma_{in\eta} < 0.011$	The log energy weighted width (σ), of the extent of the shower in the η dimension.
$R9 < 1.0$	The ratio of the energy of the 3×3 crystal core of the super-cluster compared to the total energy stored in the 5×5 super-cluster.
Combined Isolation < 6 GeV	The photons are required to be isolated with no electromagnetic or hadronic activity within a radius $\Delta R = 0.3$ of the photon object. A combination of the pileup subtracted [77], ECAL , HCAL and tracking isolation sums are used to determine the combined total isolation value.

Table 4.4.: Photon Identification criteria used within the analysis for selection/veto purposes in the $\gamma +$ jets control/signal selections.

1225 Photon objects are also required to have a minimum momentum of $p_T > 25$ GeV.

1226 • **Electrons**

1227 Electron identification is defined for veto purposes. They are selected according to
1228 the following cut-based criteria listed in Table 4.5, utilising PF-based isolation.

Categories	Barrel	EndCap
$\Delta\eta_{In}$	0.007	0.009
$\Delta\phi_{In}$	0.15	0.10
$\sigma_{inj\eta}$	0.01	0.03
H/E	0.12	0.10
d0 (vtx)	0.02	0.02
dZ (vtx)	0.20	0.20
$ (1/E_{ECAL} - 1/p_{track}) $	0.05	0.05
PF Combined isolation/ p_T	0.15	0.15
Vertex fit probability	10^{-6}	10^{-6}

Table 4.5.: Electron Identification criteria used within the analysis for veto purposes.

1229 Electrons are required to be identified at $|\eta| < 2.5$, with a minimum $p_T > 10$ GeV
1230 threshold to ensure that the electron falls within the tracking system of the detector.

1231 • **Noise and \cancel{E}_T Filters**

1232 A series of Noise filters are applied to veto events which contain spurious non-physical
1233 jets that are not picked up by the jet id, and events which give large unphysical \cancel{E}_T
1234 values. These filters are listed within Appendix (A.1).

1235 **4.2.2. Event Selection**

1236 The selection criteria for events within the analysis are detailed below. A set of common
1237 cuts are applied to both signal (maximise acceptance to a range of SUSY signatures), and
1238 control samples (retain similar jet kinematics for background predictions), with additional
1239 selection cuts applied to each control sample to enrich the sample in a particular EWK
1240 processes, see Section (4.2.3).

1241 The jets considered in the analysis are required to have a transverse momentum $p_T >$
1242 50 GeV, with a minimum of two jets required in the event. The highest E_T jet is required
1243 to lie within the central tracker acceptance $|\eta| < 2.5$, and the two leading p_T jets must

1244 each have $p_T > 100\text{GeV}$. Any event which has a jet with $p_T > 50\text{ GeV}$ that either fails
1245 the “loose” identification criteria described in Section(4.2.1) or has $|\eta| > 3.0$, is rejected.
1246 Similarly events in which an electron, muon or photon fails object identification but pass
1247 η and p_T restrictions are identified as an “odd” lepton/photon and the event is vetoed.

1248 At low H_T , the jet threshold requirements applied to be considered as part of the
1249 analysis and enter the H_T sum are scaled downwards. These are scaled down in order to
1250 not restrict phase space, preserving jet multiplicities and background admixture in the
1251 lower H_T bins, as listed in Table 4.6.

H_T bin	minimum jet p_T	second leading jet p_T
$275 < H_T < 325$	36.7	73.3
$325 < H_T < 375$	43.3	86.6
$375 < H_T$	50.0	100.0

Table 4.6.: Jet thresholds used in the three H_T regions of the analysis.

1252 Within the signal region to suppress **SM** processes with genuine \cancel{E}_T from neutrinos,
1253 events containing isolated electrons or muons are vetoed. Furthermore to ensure a pure
1254 multi-jet topology, events are vetoed if an isolated photon is found with $p_T > 25\text{ GeV}$.

1255 An α_T requirement of > 0.55 is required to reduce the QCD multi-jet background
1256 to a negligible amount. Finally additional cleaning cuts are applied to protect against
1257 pathological deficiencies such as reconstruction failures or severe energy mis-measurements
1258 due to detector inefficiencies:

- Significant \cancel{H}_T can arise in events with no real \cancel{E}_T due to multiple jets falling below the p_T threshold used for selecting jets. This in turn leads to events which can then incorrectly pass the α_T requirements of the analysis. This effect can be negated by requiring that the missing transverse momentum reconstructed from jets alone does not greatly exceed the missing transverse momentum reconstructed from all of the detector’s calorimeter towers,

$$R_{miss} = \cancel{H}_T / \cancel{E}_T < 1.25.$$

- 1259 • Fake \cancel{E}_T and \cancel{H}_T can arise due to significant jet mis-measurements cause by a small
1260 number of non-functioning **ECAL** regions. These regions absorb electromagnetic
1261 showers which are subsequently not added to the jet energy sum. To circumvent

1262 this problem the following procedure is employed : For each jet in the event, the
1263 angular separation

$$\Delta\phi_j^* \equiv \Delta\phi(p_j^\rightarrow - \sum_{i \neq j} p_i^\rightarrow), \quad (4.6)$$

1264 is calculated where that jet is itself removed from the event. Here $\Delta\phi^*$ is a measure
1265 of how aligned the H_T of an event is with a jet, a small value is compatible with the
1266 hypothesis of an inherently balanced event in which a jet has been mis-measured.
1267 For every jet in a event with $\Delta\phi^* < 0.5$, if the ΔR distance between the selected jet
1268 and the closest dead **ECAL** region is also < 0.3 , then the event is rejected. Similarly
1269 events are rejected if the jet points within $\Delta R < 0.3$ of the **ECAL** barrel-endcap
1270 gap at $|\eta| = 1.5$.

1271 Some of the key distributions of the data used in this analysis compared to MC
1272 simulation are shown in Figure 4.5. The MC samples are normalised to a luminosity of
1273 11.7 fb^{-1} , with no requirement placed upon the number of b-tagged jets or number of
1274 jets in the events.

1275 The distributions shown are presented for purely illustrative purposes, with the MC
1276 simulation itself not used in absolute term to estimate the yields from background
1277 processes, see Sections (4.2.3,4.4). However it is nevertheless important to demonstrate
1278 that good agreement exists between simulation and observation in data.

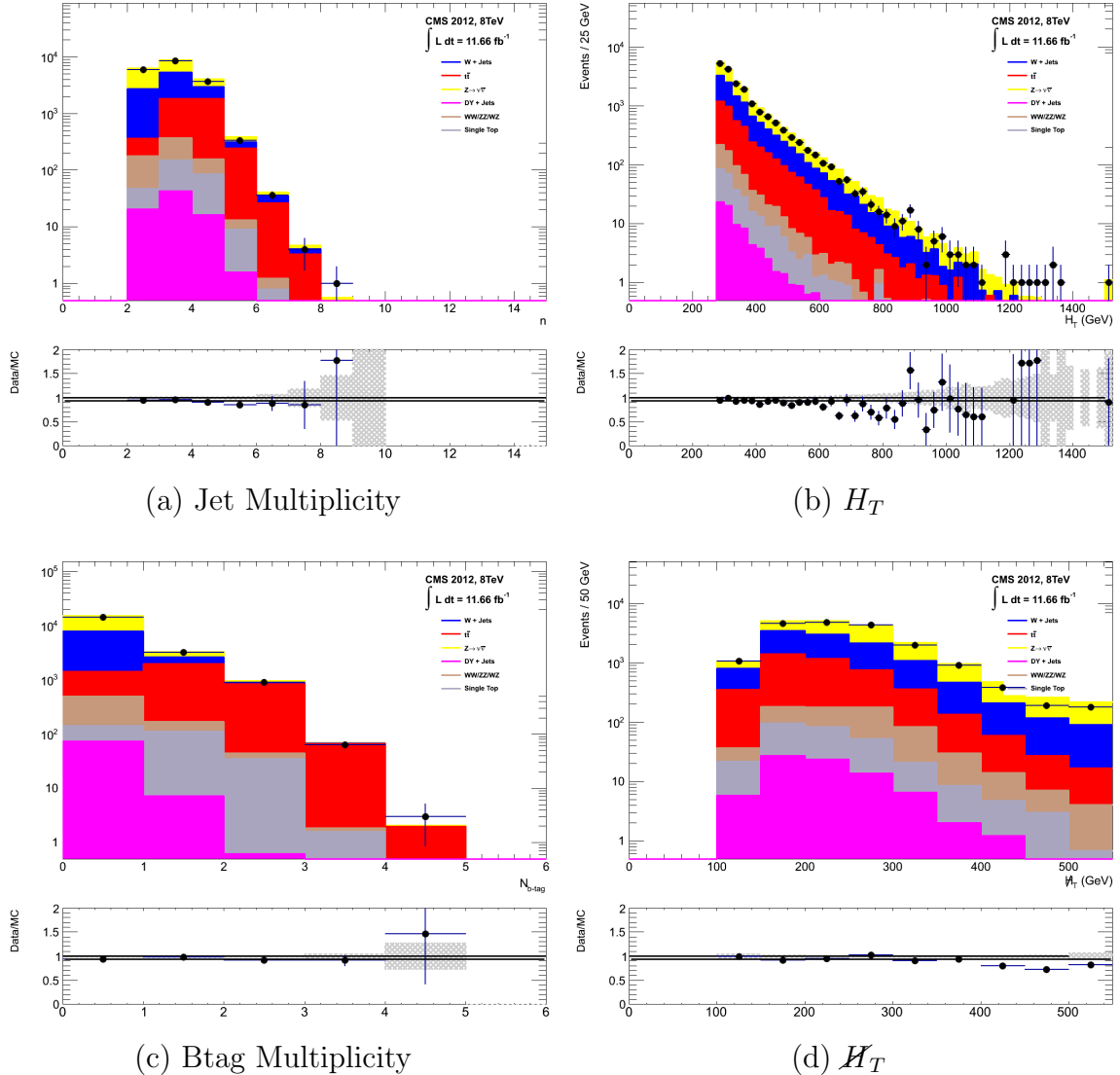


Figure 4.5.: Data/MC comparisons of key variables for the hadronic signal region, following the application of the hadronic selection criteria and the requirements of $H_T > 275$ GeV and $\alpha_T > 0.55$. Bands represent the uncertainties due to the statistical size of the MC samples. No requirement is made upon the number of b-tagged jets or jet multiplicity in these distributions.

4.2.3. Control Sample Definition

The method used to estimate the background contributions in the hadronic signal region relies on the use of a Transfer Factor (TF). This is determined from MC simulation in both the control, N_{MC}^{control} , and signal, N_{MC}^{signal} , region to transform the observed yield measured in data for a control sample, $N_{\text{obs}}^{\text{control}}$, into a background prediction, $N_{\text{pred}}^{\text{signal}}$, via Equation (4.7),

$$N_{\text{pred}}^{\text{signal}} = \frac{N_{\text{MC}}^{\text{signal}}}{N_{\text{MC}}^{\text{control}}} \times N_{\text{obs}}^{\text{control}}. \quad (4.7)$$

1286 All MC samples are normalised to the luminosity of the data samples, 11.7 fb^{-1} .
 1287 Through this method, “vanilla” predictions for the **SM** background in the signal region
 1288 can be made by considering separately the sum of the prediction from either the $\mu + \text{jets}$
 1289 and $\gamma + \text{jets}$ or $\mu + \text{jets}$ and $\mu\mu + \text{jets}$ samples. However the final background estimation
 1290 from which results are interpreted, is calculated via a fitting procedure defined formally
 1291 by the likelihood model described in Chapter 5.

1292 The sum of the expected yields from all MC processes, in each control sample enter
 1293 the denominator, $N_{\text{MC}}^{\text{control}}$, of the **TF** defined in Eq (4.7). However for the numerator
 1294 , $N_{\text{MC}}^{\text{signal}}$, only the relevant processes that the control sample is used in estimating a
 1295 background for, enter into the **TF**.

1296 For the $\mu + \text{jets}$ sample the simulated MC processes which enter the numerator of
 1297 the **TF** are,

$$N_{\text{MC}}^{\text{signal}}(H_T, n_{\text{jet}}) = N_W + N_{t\bar{t}} + N_{DY} + N_t + N_{di-boson}, \quad (4.8)$$

1298 whilst for both the $\mu\mu + \text{jets}$ and $\gamma + \text{jets}$ samples the only MC process used in the
 1299 numerator is,

$$N_{\text{MC}}^{\text{signal}}(H_T, n_{\text{jet}}) = N_{Z \rightarrow \nu\bar{\nu}}. \quad (4.9)$$

1300 The control samples and the **EWK** processes they are specifically tuned to select
 1301 are defined below, with distributions of key variables for each of the control samples
 1302 shown for illustrative purposes in Figures 4.6, 4.7 and 4.8. No requirement is placed
 1303 upon the number of b-tagged jets or jet multiplicity in the distributions shown. The
 1304 MC distributions highlight the background compositions of each control sample, where
 1305 in general, good agreement is observed between data and simulation, giving confidence

1306 that the samples are well understood. The contribution from QCD multi-jet events is
1307 expected to be negligible :

1308 **The $\mu +$ jets control sample**

1309 Events from $W +$ jets and $t\bar{t}$ processes enter into the hadronic signal sample due to
1310 unidentified leptons from acceptance or threshold effects and hadronic tau decays.
1311 These leptons originate from the decay of high p_T W bosons.

1312 The control samples specifically identifies $W \rightarrow \mu\bar{\nu}$ decays within the same phase-
1313 space of the signal region, where the muon is subsequently ignored in the calculation
1314 of event level variables, i.e. H_T , \mathcal{H}_T , α_T . All kinematic jet-based cuts are identical
1315 to those applied in the hadronic search region detailed in Section (4.2.2), with the
1316 same H_T , jet multiplicity and b-jet multiplicity binning described above.

- 1317 – Muons originating from W boson decays are selected by requiring one tightly
1318 isolated muon defined in Table 4.3, with a $p_T > 30$ GeV and $|\eta| < 2.1$. Both of
1319 these threshold arise from trigger restrictions.
- 1320 – The transverse mass of the W candidate must satisfy $M_T(\mu, \cancel{E}_T) < 30$ GeV (to
1321 suppress QCD multi-jet events).
- 1322 – Events which contain a jet overlapping with a muon $\Delta R(\mu, \text{jet}) < 0.5$ are vetoed
1323 to remove events from muons produced as part of a jet’s hadronisation process.
- 1324 – Events containing a second muon candidate which has failed id, but passed p_T
1325 and $|\eta|$ requirements, are checked to have an invariant mass that satisfies $m_Z - 25 < M_{\mu_1\mu_2} > m_Z + 25$, thus removing $Z \rightarrow \mu\mu$ contamination.

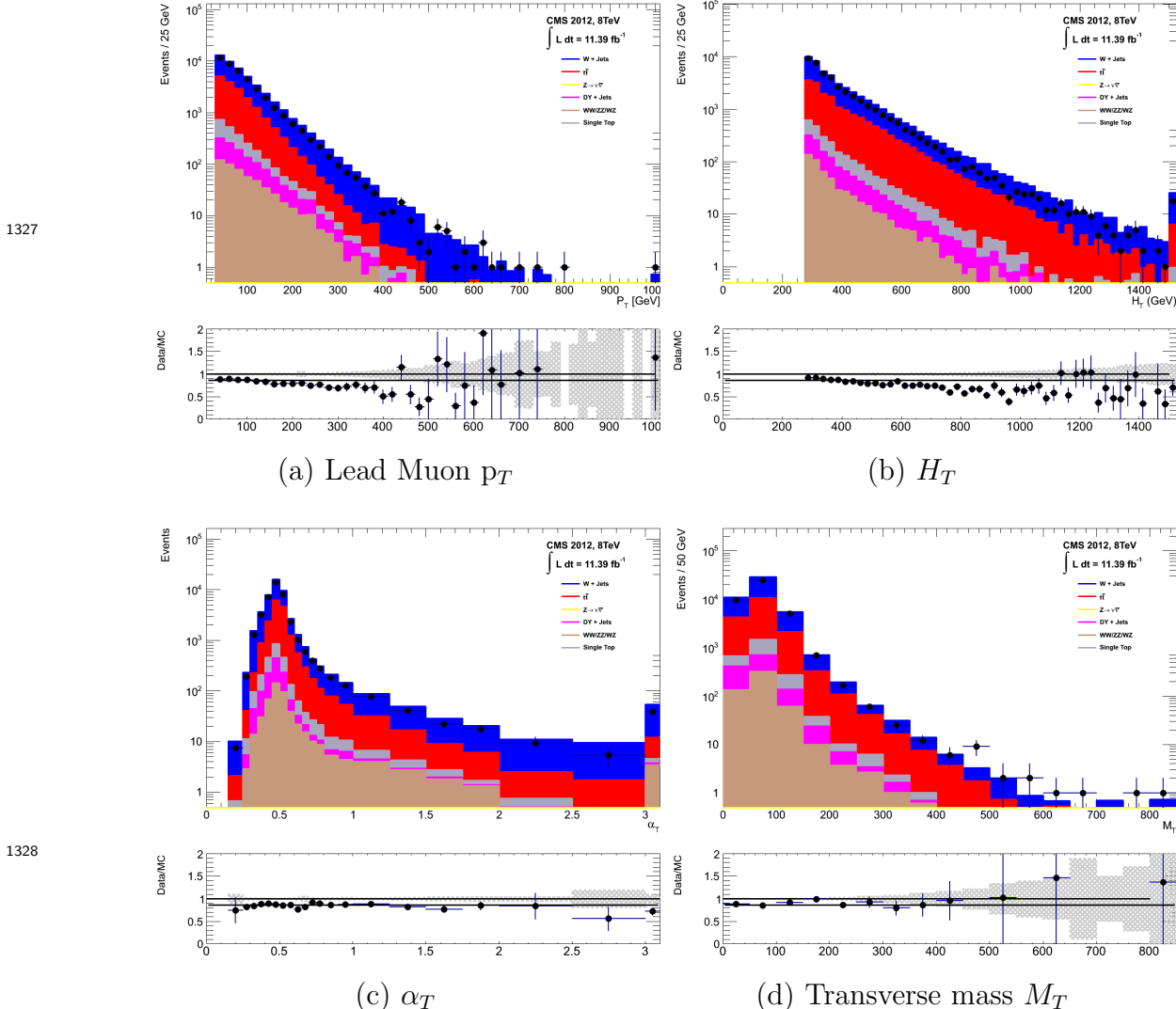


Figure 4.6.: Data/MC comparisons of key variables for the $\mu +$ jets selection, following the application of selection criteria and the requirements that $H_T > 275$ GeV. Bands represent the uncertainties due to the statistical size of the MC samples. No requirement is made upon the number of b-tagged jets or jet multiplicity in these distributions.

The $\mu\mu$ + jets control sample

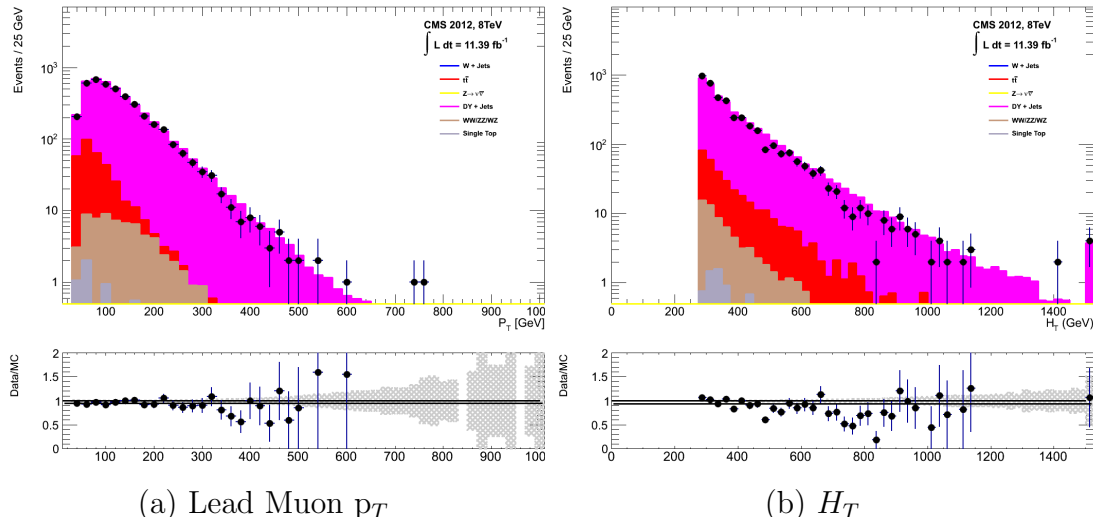
The $Z \rightarrow \nu\bar{\nu} + \text{jets}$ background enters into the signal region from genuine \cancel{E}_T from the escaping neutrinos. This background is estimated using two control samples, the first of which is the $Z \rightarrow \mu\bar{\mu} + \text{jets}$ process, which possesses identical kinematic properties, but with different acceptance and branching ratio [1].

The same acceptance requirements as the $\mu + \text{jets}$ selection for muons is applied, as defined in Table 4.3. Muons in the event are ignored for the purpose of the

calculation of event level variables. Kinematic jet-based cuts and phase space binning identical to the hadronic search region are also applied.

- Muons origination from a Z boson decay are selected requiring exactly two tightly isolated muons. Due to trigger requirements the leading muon is required to have $p_T > 30$ GeV and $|\eta| < 2.1$. The requirement of the p_T on the second muon is relaxed to 10 GeV.
- Events are vetoed if containing a jet overlapping with a muon $\Delta R(\mu, \text{jet}) < 0.5$.
- In order to specifically select two muons both originating from a single Z boson decay, the invariant mass of the two muons must satisfy $m_Z - 25 > M_{\mu_1\mu_2} < m_Z + 25$.

The $\mu\mu + \text{jets}$ sample is used to make predictions in the signal region in the two lowest H_T bins, providing coverage where the $\gamma + \text{jets}$ sample is unable to, due to trigger requirements. In higher H_T bins, the higher statistics of the $\gamma + \text{jets}$ sample is instead used to determine the $Z \rightarrow \nu\bar{\nu}$ estimation.



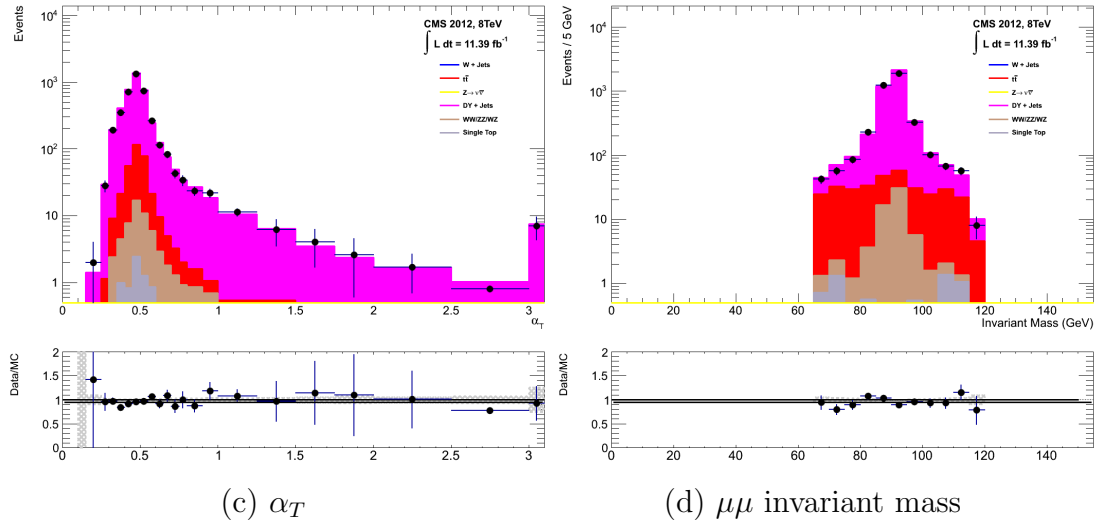


Figure 4.7.: Data/MC comparisons of key variables for the $\mu\mu + \text{jets}$ selection, following the application of selection criteria and the requirements that $H_T > 275$ GeV. Bands represent the uncertainties due to the statistical size of the MC samples. No requirement is made upon the number of b-tagged jets or jet multiplicity in these distributions.

The γ + jets control sample

The $Z \rightarrow \nu\bar{\nu} + \text{jets}$ background is also estimated from a $\gamma + \text{jets}$ control sample, which possesses a larger cross section and kinematic properties similar to those of $Z \rightarrow \mu\bar{\mu}$ events where the photon is ignored [78][79]. The photon is ignored for the purpose of the calculation of event level variables, and identical selection cuts to the hadronic signal region are applied.

- Exactly one photon is selected, satisfying identification criteria as detailed in Table 4.4, with a minimum $p_T > 165$ GeV to satisfy trigger thresholds and $|\eta| < 1.45$ to ensure the photon remains in the barrel of the detector.
 - A selection criteria of $\Delta R(\gamma, jet) < 1.0$, between the photon and all jets is applied to ensure the acceptance of only well isolated $\gamma + \text{jets}$ events.
 - Given that the photon is ignored, this control sample can only be applied in the H_T region > 375 GeV, due to the trigger thresholds on the minimum p_T of the photon, and the H_T requirement of an $\alpha_T > 0.55$ cut from Equation (4.5).

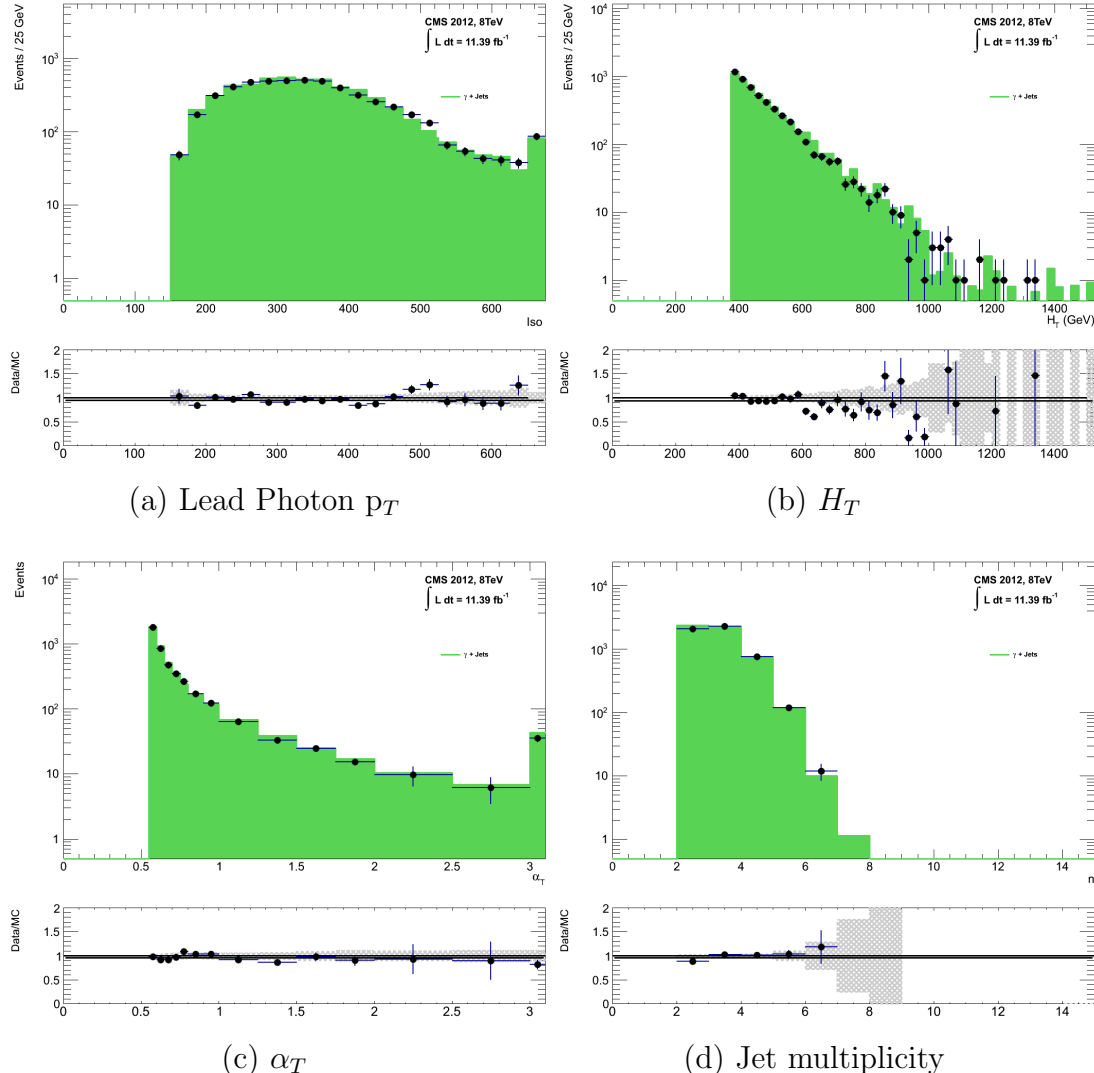


Figure 4.8.: Data/MC comparisons of key variables for the $\gamma + \text{jets}$ selection, following the application of selection criteria and the requirements that $H_T > 375 \text{ GeV}$ and $\alpha_T > 0.55$. Bands represent the uncertainties due to the statistical size of the MC samples. No requirement is made upon the number of b-tagged jets or jet multiplicity in these distributions.

The selection criteria of the three control samples are defined to ensure background composition and event kinematics mirror closely the signal region. This is done in order to minimise the reliance on MC simulation to model correctly the backgrounds and event kinematics in the control and signal samples.

However in the case of the $\mu + \text{jets}$ and $\mu\mu + \text{jets}$ samples, the α_T requirement is relaxed in the selection criteria of these samples. This is made possible as contamination from QCD multi-jet events is suppressed to a negligible level by the other kinematic selection criteria within the two control samples, to select pure EWK processes. Thus in

1375 this way, the acceptance of the two muon control samples can be significantly increased,
1376 which simultaneously improves their predictive power and further reduces the effect of
1377 any potential signal contamination.

1378 The modelling of the α_T variable is probed through a dedicated set of closure tests,
1379 described in Section (4.6), which demonstrate that the different α_T acceptances for the
1380 control and signal samples have no significant systematic bias on the prediction.

1381 4.2.4. Estimating the QCD background multi-jet background

1382 A negligible background from QCD multi-jet events within the hadronic signal region
1383 is expected due to the selection requirement, and additional cleaning filters applied.
1384 However a conservative approach is still adopted and the likelihood model (see Section
1385 (5.1)), is given the freedom to estimate any potential QCD multi-jet contamination.

1386 Any potential contamination can be identified through the variable R_{α_T} , defined as
1387 the ratio of events above and below the α_T threshold value used in the analysis. This is
1388 modelled by a H_T dependant falling exponential function which takes the form,

$$R_{\alpha_T}(H_T) = A \exp^{-k_{QCD} H_T}, \quad (4.10)$$

1389 where the parameters A and k_{QCD} are the normalisation and exponential decay
1390 constants respectively.

1391 For QCD event topologies this exponential behaviour is expected as a function of H_T
1392 for several reasons. The improvement of jet energy resolution at higher H_T due to higher
1393 p_T jets leads to a narrower peaked distribution, causing R_{α_T} to fall. Similarly at higher
1394 H_T values > 375 GeV, the jet multiplicity rises slowly with H_T . As shown in Figure 4.3,
1395 at higher jet multiplicities, the result of the combinatorics used in the determination of
1396 α_T , also lead to a narrower α_T distribution.

1397 The value of the decay constant k_{QCD} is constrained via measurements within data
1398 sidebands to the signal region. This is also done to validate the falling exponential
1399 assumption for QCD multi-jet topologies. The sidebands are enriched in QCD multi-jet
1400 background and defined as regions where α_T is relaxed or that the R_{miss} cut is inverted.

1401 Figure 4.9 depicts the definition of these data sidebands used to constrain the value of
1402 k_{QCD} .

1403

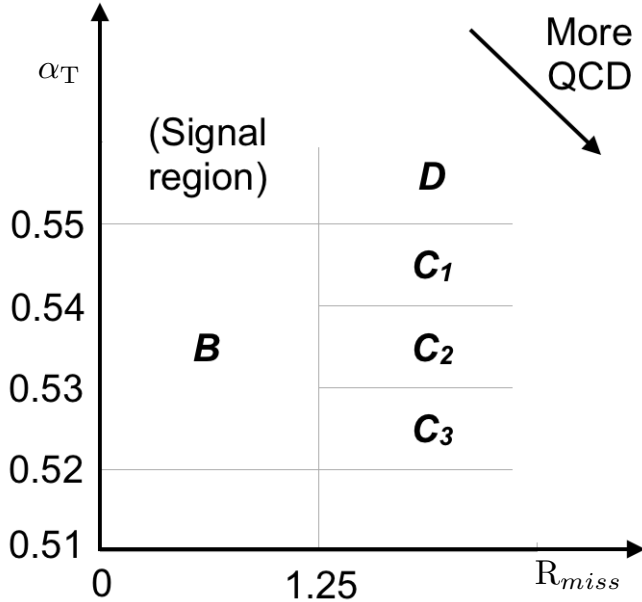


Figure 4.9.: QCD sideband regions, used for determination of k_{QCD} .

1404 The fits to determine the value of k_{QCD} are shown in Appendix (C.1), for which the best
1405 fit value obtained from sideband region B is determined to be $k_{QCD} = 2.96 \pm 0.64 \times 10^{-2}$
1406 GeV^{-1} .

1407 The best fit values of the remaining three C sideband regions are used to estimate
1408 the systematic uncertainty on the central value obtained from sideband region B. The
1409 variation of these measured values is used to determine the error on the determined
1410 central value, and is calculated to be $1.31 \pm 0.26 \times 10^{-2} \text{GeV}^{-1}$. This relative error of \sim
1411 20% gives an estimate of the systematic uncertainty of the measurement to be applied to
1412 k_{QCD} .

1413 Finally the same procedure is performed for sideband region D to establish that the
1414 value of k_{QCD} extracted from a lower α_T slice can be applied to the signal region $\alpha_T >$
1415 0.55. The likelihood fit is performed across all H_T bins within the QCD enriched region
1416 with no constraint applied to k_{QCD} . The resulting best fit value for k_{QCD} shows good
1417 agreement between that and the weighted mean determined from the three C sidebands
1418 regions. This demonstrates that the assumption of using the central value determined
1419 from sideband region B, to provide an unbiased estimator for k_{QCD} in the signal region
1420 ($\alpha_T > 0.55$) is valid.

1421 Table 4.7, summarises the best fit k_{QCD} values determined for each of the sideband
1422 regions to the signal region.

Sideband region	$k_{QCD} (\times 10^{-2} \text{GeV}^{-1})$	p-value
B	2.96 ± 0.64	0.24
C ₁	1.19 ± 0.45	0.93
C ₂	1.47 ± 0.37	0.42
C ₃	1.17 ± 0.55	0.98
C(weighted mean)	1.31 ± 0.26	-
D(likelihood fit)	1.31 ± 0.09	0.57

Table 4.7.: Best fit values for the parameters k_{QCD} obtained from sideband regions B,C₁,C₂,C₃. The weighted mean is determined from the three measurements made within sideband region C. The maximum likelihood value of k_{QCD} given by the simultaneous fit using sideband region D. Quotes errors are statistical only.

1423 4.3. Trigger Strategy

1424 A cross trigger based on the quantities H_T and α_T , labelled is used with varying thresholds
1425 across H_T bins to record the events used in the hadronic signal region. The α_T legs of the
1426 HT_alphaT triggers used in the analysis are chosen to fully suppress QCD multi-jet events,
1427 whilst maintaining a sustainable trigger rate. To further maintain an acceptable rate for
1428 these analysis specific triggers, only calorimeter information is used in the reconstruction
1429 of the H_T sum, leading to the necessity for Calo jets to be used within the analysis.

1430 A single object prescaled H_T trigger is used to collect events for the hadronic control
1431 region described above in Section (4.2.4).

1432 The performance of the α_T and H_T triggers used to collect data for the signal and
1433 hadronic control region is measured with respect to a reference sample collected using the
1434 muon system. This allows measurement of both the Level 1 seed and higher level triggers
1435 simultaneously, as the reference sample is collected independent of any jet requirements.

1436 The selection for the trigger efficiency measurement is identical to that described in
1437 Section (4.2.2), with the requirement of exactly one well identified muon with $p_T > 30$
1438 GeV which is subsequently ignored.

1439 The efficiencies measure for the HT_alphaT triggers in bins individual H_T and α_T legs,
1440 is summarised in Table 4.8.

H_T range (GeV)	ϵ on H_T leg (%)	ϵ on α_T leg (%)
275-325	$87.7^{+1.9}_{-1.9}$	$82.8^{+1.0}_{-1.1}$
325-375	$90.6^{+2.9}_{-2.9}$	$95.9^{+0.7}_{-0.9}$
375-475	$95.7^{+0.1}_{-0.1}$	$98.5^{+0.5}_{-0.9}$
475- ∞	$100.0^{+0.0}_{-0.0}$	$100.0^{+0.0}_{-4.8}$

Table 4.8.: Measured efficiencies of the H_T and α_T legs of the HT and HT_alphaT triggers in independent analysis bins. The product of the two legs gives the total efficiency of the trigger in a given offline H_T bin.

1441 Data for the control samples of the analysis, detailed in Section (4.2.3), are collected
1442 using single object photon trigger for the $\gamma +$ jets sample, and a single object muon
1443 trigger for both the $\mu +$ jets and $\mu\mu +$ jets control samples. The photon trigger is
1444 measured to be full efficient for the threshold $p_T^{photon} > 150 GeV$, whilst the single muon
1445 efficiency satisfying $p_T^{muon} > 30 GeV$ is measured to have an efficiency of 88% that is
1446 independent of H_T .

1447 Dimuon efficiency measurement.

₁₄₄₈ **4.4. A method to determine MC yields with higher
₁₄₄₉ statistical precision**

₁₄₅₀ **4.5. Measuring MC normalisation factors via H_T
₁₄₅₁ sidebands**

₁₄₅₂ **4.6. Systematic Uncertainties on Transfer Factors**

₁₄₅₃ **4.7. Searches for Natural SUSY with B-tag
₁₄₅₄ templates.**

₁₄₅₅ Btag Templates blah blah

Chapter 5.

¹⁴⁵⁶ Results

¹⁴⁵⁷ Results at 12fb 8TeV

¹⁴⁵⁸ 5.1. Statistical Interpretation

¹⁴⁵⁹ Likelihood stuff

¹⁴⁶⁰ 5.2. Interpretation in Simplified Signal Models

¹⁴⁶¹ Result interpretation

¹⁴⁶²

Appendix A.

¹⁴⁶³ Miscellaneous

¹⁴⁶⁴ A.1. Noise Filters

¹⁴⁶⁵ For Calo jets the following criteria were applied:

¹⁴⁶⁶ • N90 hits > 1 ,

¹⁴⁶⁷ • HBHE > 0.01 ,

¹⁴⁶⁸ • fHPD < 0.98 ,

¹⁴⁶⁹ For PF jets the following criteria were applied:

¹⁴⁷⁰ • Neutral hadron fraction < 0.99 ,

¹⁴⁷¹ • Neutral EM fraction < 0.99 ,

¹⁴⁷² • Number of constituents > 1 ,

¹⁴⁷³ • Charged hadron fraction > 0 ,

¹⁴⁷⁴ • Charged multiplicity > 0 ,

¹⁴⁷⁵ • Charged EM fraction < 0.99 .

¹⁴⁷⁶ The following noise filters are applied, to remove events with spurious, non-physical
¹⁴⁷⁷ jets or missing transverse energy.

¹⁴⁷⁸ • CSC tight beam halo filter,

¹⁴⁷⁹ • HBHE noise filter with isolated noise rejection,

- 1480 • HCAL laser filter,
- 1481 • ECAL dead cell trigger primitive (TP) filter,
- 1482 • Tracking failure filter,
- 1483 • Bad EE Supercrystal filter,
- 1484 • ECAL Laser correction filter.

1485 A.2. Primary Vertices

1486 The pileup per event is defined by the number of 'good' reconstructed primary vertices
1487 in the event, with each vertex satisfying the following requirements

- 1488 • $N_{dof} > 4$;
- 1489 • vertex position along the bead direction of $|z_{vtx}| < 24\text{cm}$;
- 1490 • vertex position perpendicular to the beam of $\rho < 2\text{cm}$.

Appendix B.

¹⁴⁹¹ L1 Jets

¹⁴⁹² B.1. Jet matching efficiencies

¹⁴⁹³ The single jet turn-on curves are derived from events independent of whether the leading
¹⁴⁹⁴ jet in an event is matched to a Level 1 jet using ΔR matching detailed in Section (3.4.3)
¹⁴⁹⁵ or not. These turn-ons are produced from events which are not triggered on jet quantities
¹⁴⁹⁶ and therefore it is not guaranteed that the lead jet of an event will be seeded by a Level
¹⁴⁹⁷ 1 jet. Figure B.1 shows the particular matching efficiency of a lead jet to a L1 jet.

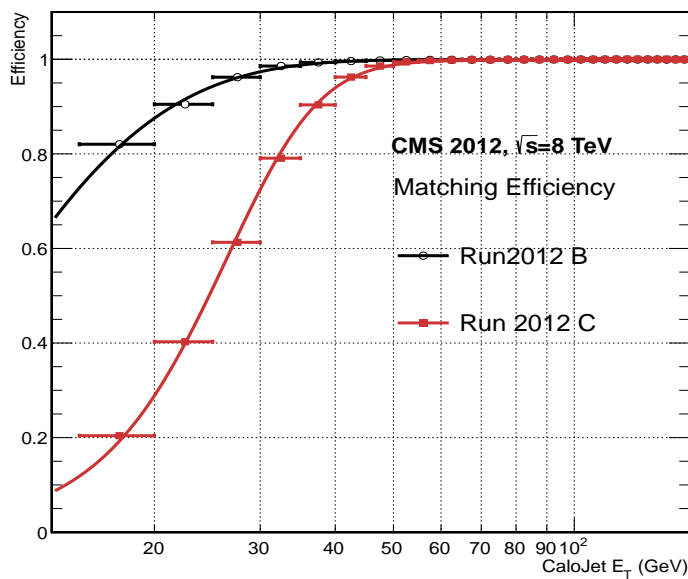


Figure B.1.: Leading jet matching efficiency as a function of the offline CaloJet E_T , measured in an isolated muon triggered dataset in the 2012B and 2012C run periods.

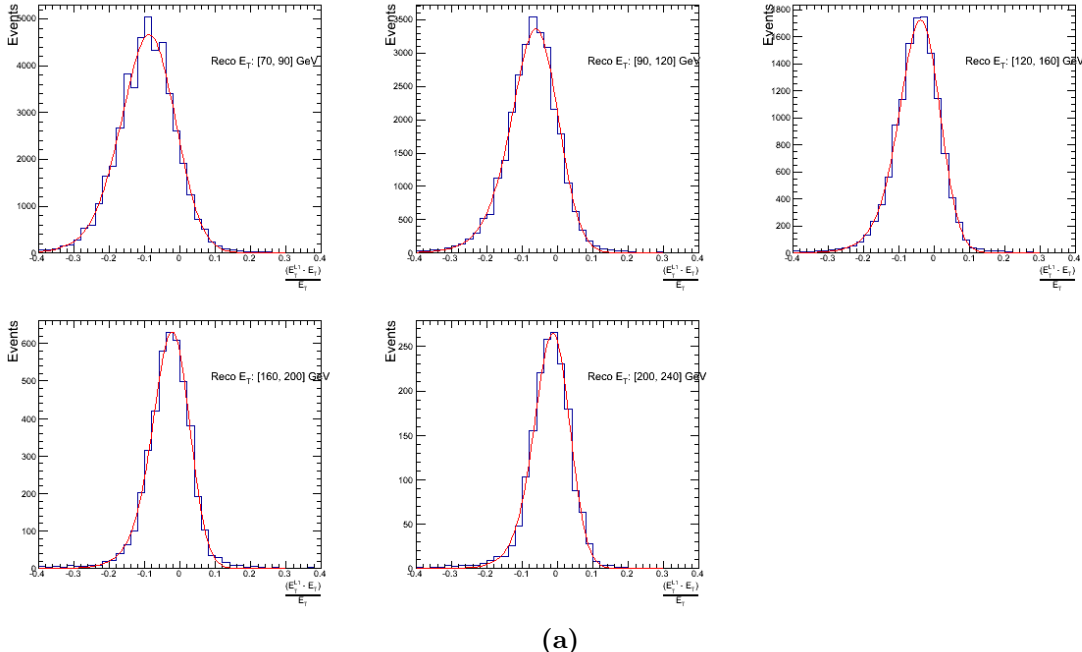
Run Period	μ	σ
2012B	6.62 ± 0.01	0.79 ± 0.03
2012C	19.51 ± 0.03	7.14 ± 0.02

Table B.1.: Results of a cumulative EMG function fit to the turn-on curves for the matching efficiency of the leading jet in an event to a Level-1 jet in run 2012C and 2012B data, measured in an isolated muon triggered sample. The turn-on point, μ , and resolution, σ , are measured with respect to offline Calo Jet E_T .

It can be seen that the turn on is sharper during the 2012B run period. The seed threshold requirement of a 5 GeV jet seed in run 2012C results in more events in which even the lead offline jet does not have an associated L1 jet. For larger jet E_T thresholds, typical of thresholds used in physics analyses, 100% efficiency is observed.

The matching efficiencies have a μ values of 6.62 GeV and 19.51 GeV for Run 2012B and 2012C respectively and is shown in Table B.1.

B.2. Leading Jet Energy Resolution



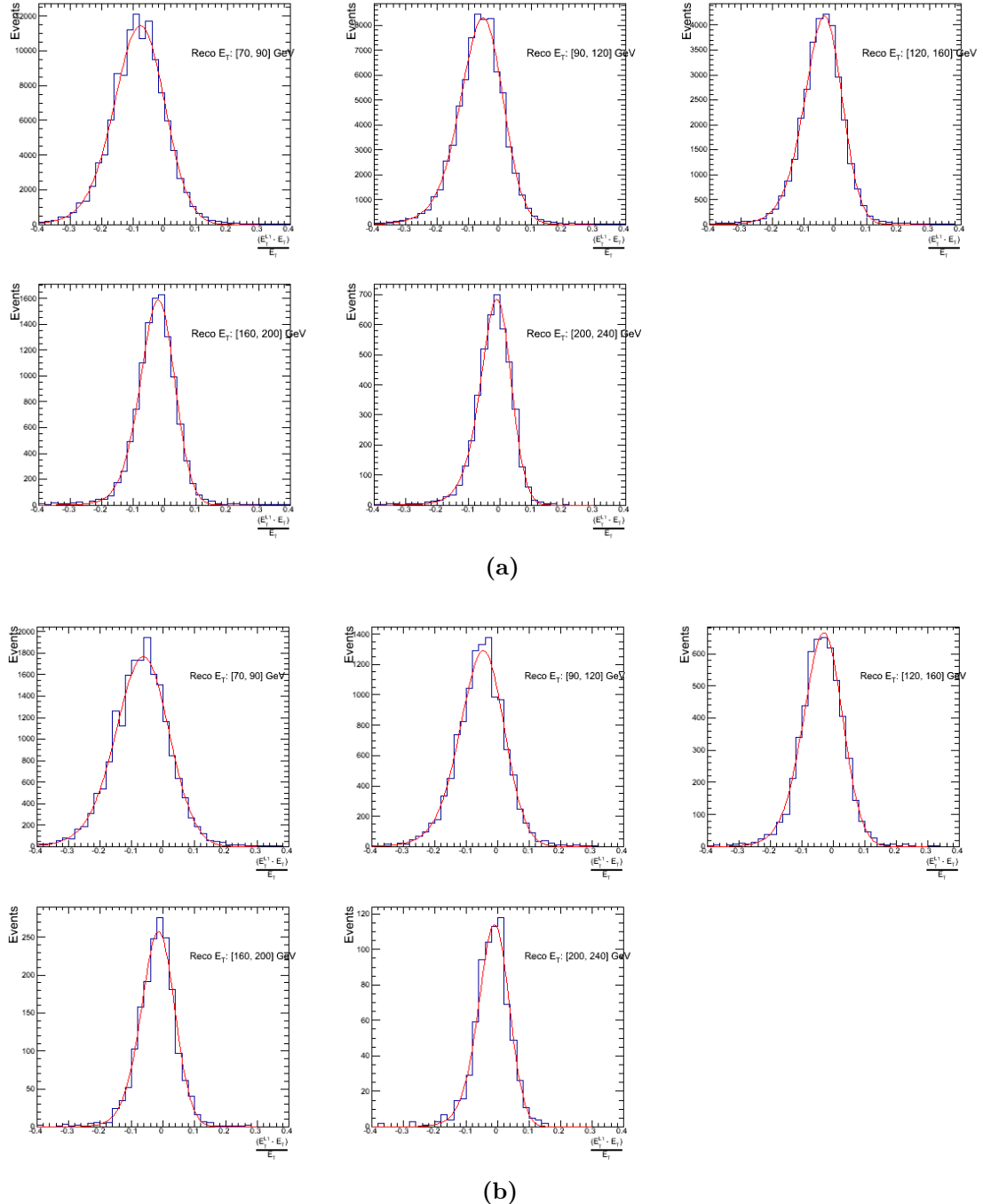
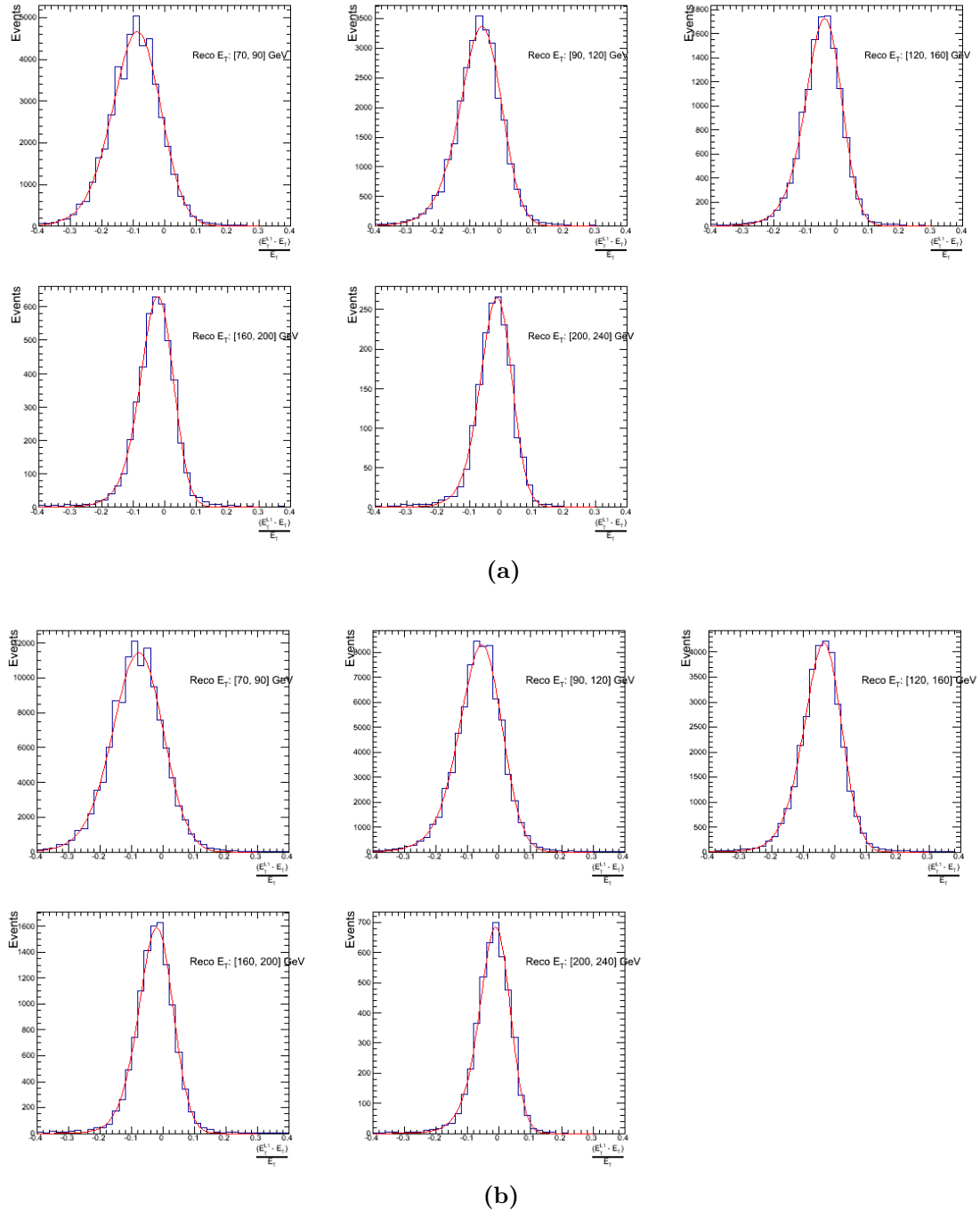


Figure B.2.: Resolution plots of the leading offline jet Calo E_T measured as a function of $\frac{(\text{L1 } E_T - \text{Offline } E_T)}{\text{Offline } E_T}$ for low (a), medium (b) and high (c) pile-up conditions.



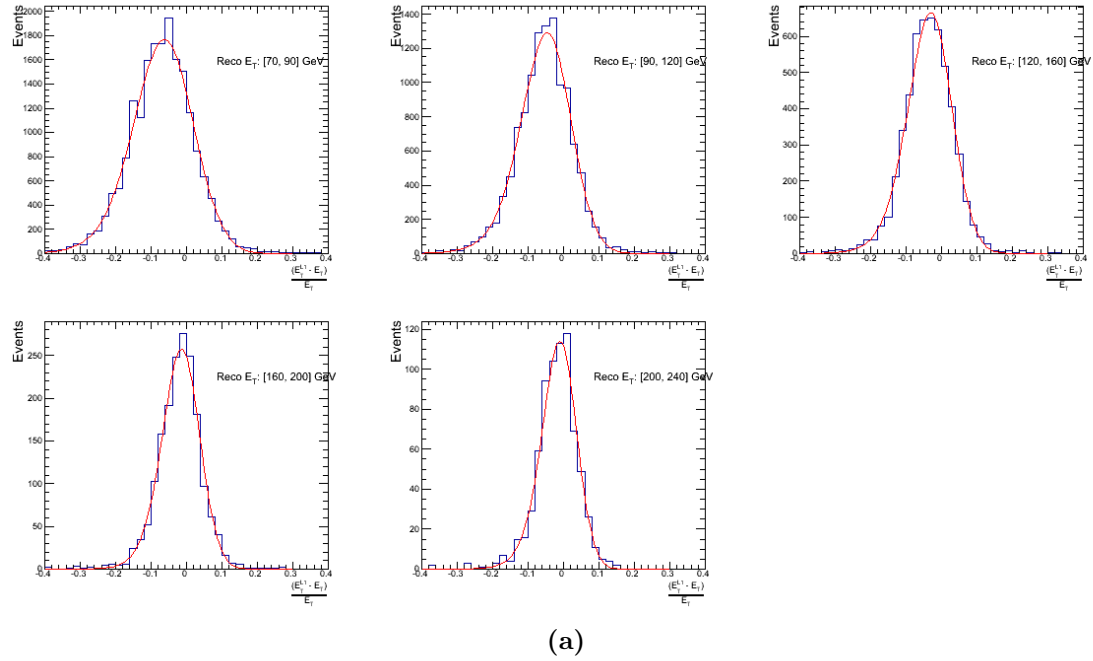


Figure B.3.: Resolution plots of the leading offline jet PF E_T measured as a function of $\frac{(L1 E_T - \text{Offline } E_T)}{\text{Offline } E_T}$ for low (a), medium (b) and high (c) pile-up conditions.

1505 B.3. Resolution for Energy Sum Quantities

1506 The following plots show the resolution parameters for the four energy sum quantities as
 1507 a function of the quantity (q) itself. In this case, The mean and RMS of the individual
 1508 $\frac{(L1 q - \text{Offline } q)}{\text{Offline } q}$ distributions, in bins of the quantity q is displayed.

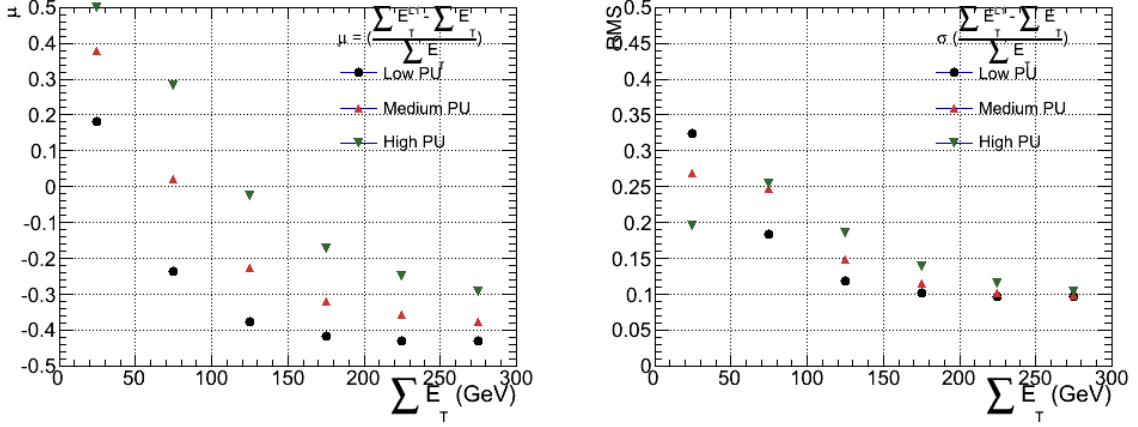


Figure B.4.: $\sum E_T$ resolution parameters in bins of Calo $\sum E_T$ measured for the defined low, medium and high pile up conditions. The plots show the mean μ (left), resolution σ (RMS) of the $\frac{\Delta q}{q}$ distributions.

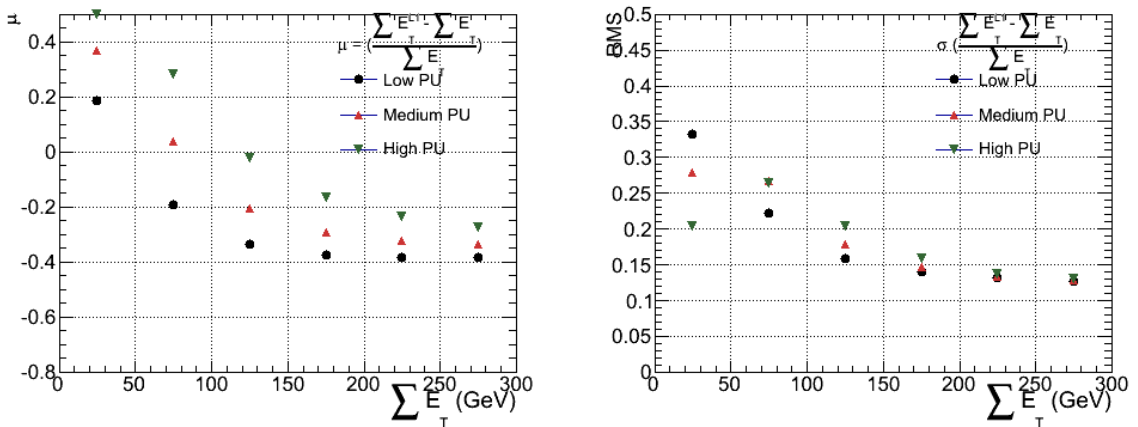


Figure B.5.: $\sum E_T$ resolution parameters in bins of PF $\sum E_T$ measured for the defined low, medium and high pile up conditions. The plots show the mean μ (left), resolution σ (RMS) of the $\frac{\Delta q}{q}$ distributions.

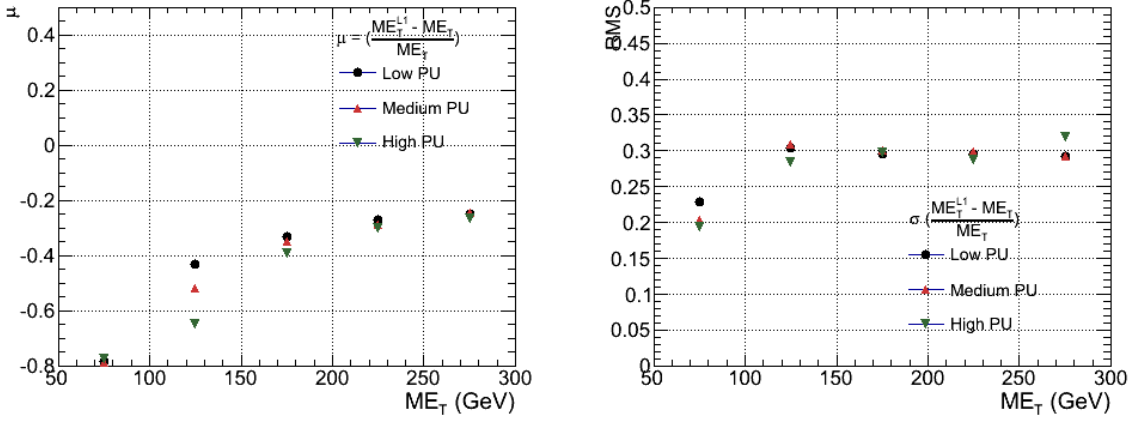


Figure B.6.: \mathcal{E}_T resolution parameters in bins of Calo \mathcal{E}_T measured for the defined low, medium and high pile up conditions. The plots show the mean μ (left), resolution σ (RMS) of the $\frac{\Delta q}{q}$ distributions.

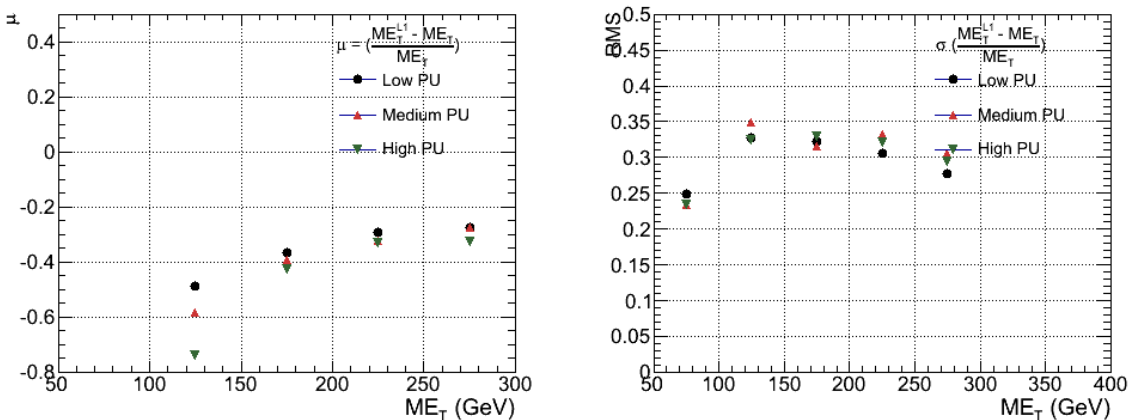


Figure B.7.: \mathcal{E}_T resolution parameters in bins of PF \mathcal{E}_T measured for the defined low, medium and high pile up conditions. The plots show the mean μ (left), resolution σ (RMS) of the $\frac{\Delta q}{q}$ distributions.

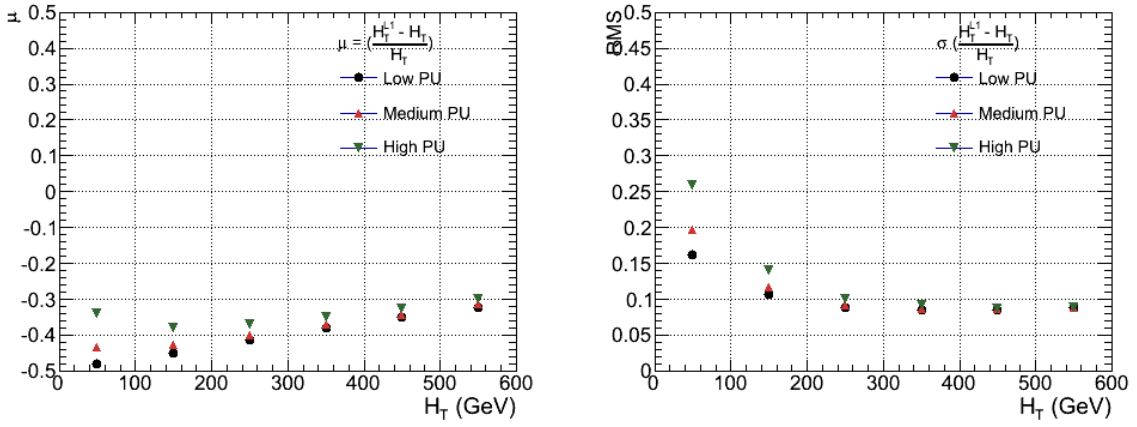


Figure B.8.: H_T resolution parameters in bins of Calo H_T measured for the defined low, medium and high pile up conditions. The plots show the mean μ (left), resolution σ (RMS) of the $\frac{\Delta q}{q}$ distributions.

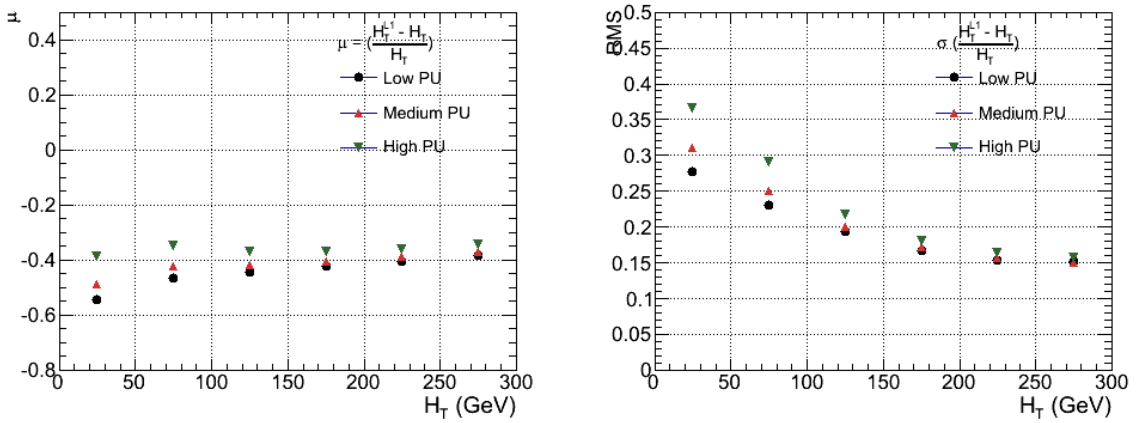


Figure B.9.: H_T resolution parameters in bins of PF H_T measured for the defined low, medium and high pile up conditions. The plots show the mean μ (left), resolution σ (RMS) of the $\frac{\Delta q}{q}$ distributions.

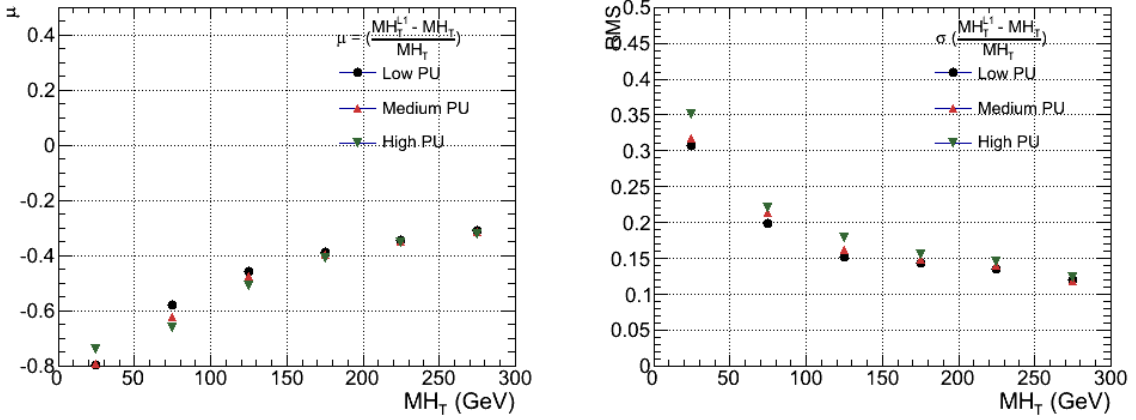


Figure B.10.: H_T resolution parameters in bins of H_T measured for the defined low, medium and high pile up conditions. The plots show the mean μ (left), resolution σ (RMS) of the $\frac{\Delta q}{q}$ distributions.

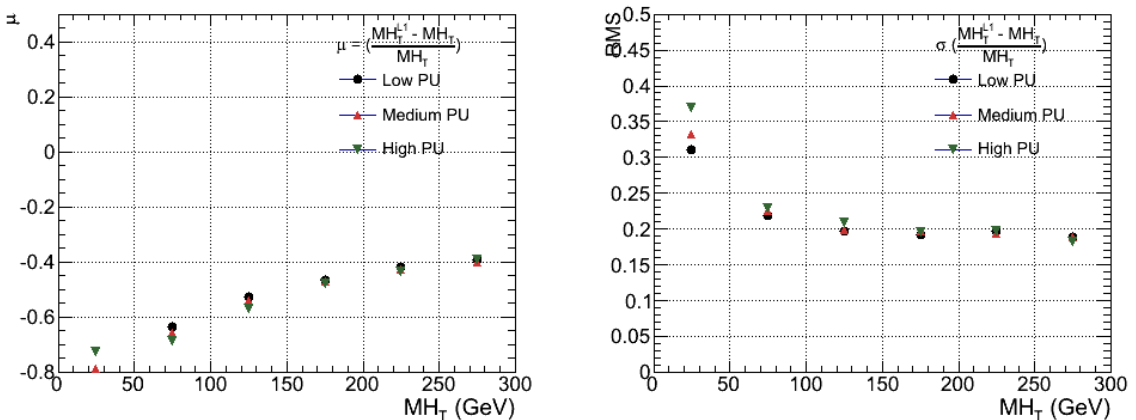


Figure B.11.: H_T resolution parameters in bins of PF H_T measured for the defined low, medium and high pile up conditions. The plots show the mean μ (left), resolution σ (RMS) of the $\frac{\Delta q}{q}$ distributions.

Appendix C.

1509 **Additional material on background
1510 estimation methods**

1511 **C.1. Determination of k_{QCD}**

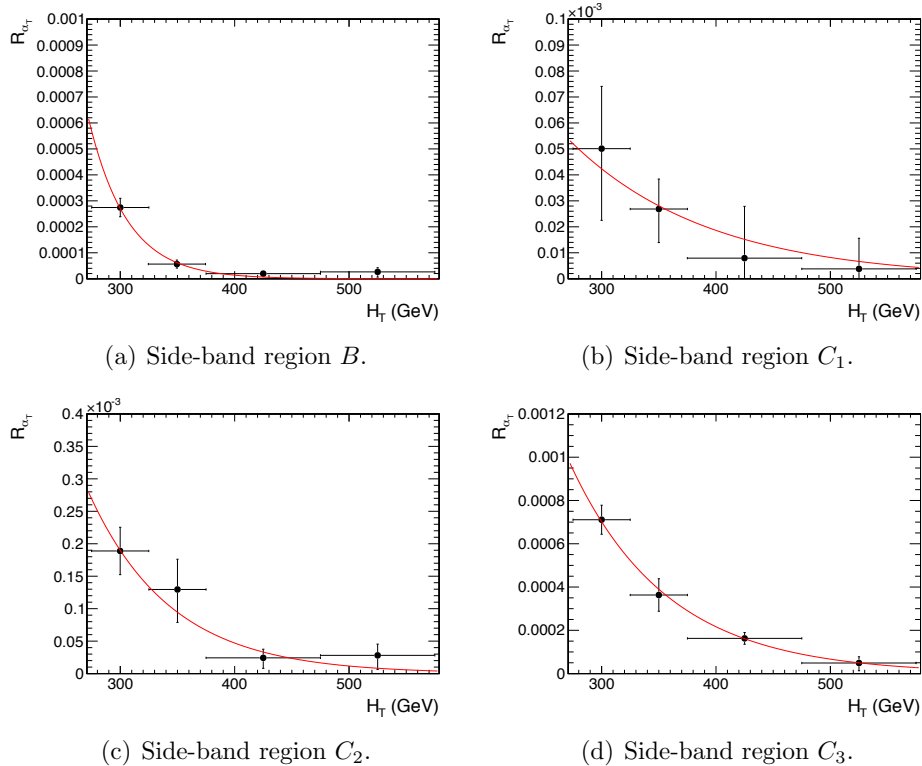


Figure C.1.: $R_{\alpha_T}(H_T)$ and exponential fits for each of the data sideband regions. Fit is conducted between the H_T region $275 < H_T < 575$.

¹⁵¹⁴ Bibliography

- ¹⁵¹⁵ [1] J. Beringer *et al.*, “Review of Particle Physics (RPP),” *Phys.Rev.*, vol. D86, p. 010001, 2012.
- ¹⁵¹⁶ [2] G. H. et al., “Nine-year wilkinson microwave anisotropy probe (wmap) observations: Cosmological parameter results,” *The Astrophysical Journal Supplement Series*, vol. 208, no. 2, p. 19, 2013.
- ¹⁵¹⁷ [3] G. Aad *et al.*, “Observation of a new particle in the search for the Standard Model Higgs boson with the ATLAS detector at the LHC,” *Phys.Lett.*, vol. B716, pp. 1–29, 2012.
- ¹⁵¹⁸ [4] S. Chatrchyan *et al.*, “Observation of a new boson at a mass of 125 GeV with the CMS experiment at the LHC,” *Phys.Lett.*, vol. B716, pp. 30–61, 2012.
- ¹⁵¹⁹ [5] S. Chatrchyan *et al.*, “Search for supersymmetry in hadronic final states with missing transverse energy using the variables AlphaT and b-quark multiplicity in pp collisions at 8 TeV,” *Eur.Phys.J.*, vol. C73, p. 2568, 2013.
- ¹⁵²⁰ [6] S. Weinberg, “A model of leptons,” *Phys. Rev. Lett.*, vol. 19, pp. 1264–1266, Nov 1967.
- ¹⁵²¹ [7] S. Glashow, “Partial Symmetries of Weak Interactions,” *Nucl.Phys.*, vol. 22, pp. 579–588, 1961.
- ¹⁵²² [8] A. Salam, “Weak and Electromagnetic Interactions,” *Conf.Proc.*, vol. C680519, pp. 367–377, 1968.
- ¹⁵²³ [9] G. Hooft, “Renormalizable lagrangians for massive yang-mills fields,” *Nuclear Physics B*, vol. 35, no. 1, pp. 167 – 188, 1971.
- ¹⁵²⁴ [10] F. Hasert *et al.*, “Observation of Neutrino Like Interactions Without Muon Or Electron in the Gargamelle Neutrino Experiment,” *Phys.Lett.*, vol. B46, pp. 138–140, 1973.

- 1539 [11] G. Arnison *et al.*, “Experimental Observation of Lepton Pairs of Invariant Mass
1540 Around 95-GeV/c**2 at the CERN SPS Collider,” *Phys.Lett.*, vol. B126, pp. 398–410,
1541 1983.
- 1542 [12] M. Banner *et al.*, “Observation of Single Isolated Electrons of High Transverse
1543 Momentum in Events with Missing Transverse Energy at the CERN anti-p p
1544 Collider,” *Phys.Lett.*, vol. B122, pp. 476–485, 1983.
- 1545 [13] E. Noether, “Invariante variationsprobleme,” *Nachrichten von der Gesellschaft
1546 der Wissenschaften zu Gttingen, Mathematisch-Physikalische Klasse*, vol. 1918,
1547 pp. 235–257, 1918.
- 1548 [14] F. Halzen and A. D. Martin, “Quarks and leptons.” Wiley, 1985.
- 1549 [15] *Introduction to Elementary Particles*. Wiley-VCH, 2nd ed., Oct. 2008.
- 1550 [16] C. S. Wu, E. Ambler, R. W. Hayward, D. D. Hoppes, and R. P. Hudson, “Ex-
1551 perimental Test of Parity Conservation in Beta Decay,” *Physical Review*, vol. 105,
1552 pp. 1413–1415, Feb. 1957.
- 1553 [17] P. Higgs, “Broken symmetries, massless particles and gauge fields,” *Physics Letters*,
1554 vol. 12, no. 2, pp. 132 – 133, 1964.
- 1555 [18] F. Englert and R. Brout, “Broken symmetry and the mass of gauge vector mesons,”
1556 *Phys. Rev. Lett.*, vol. 13, pp. 321–323, Aug 1964.
- 1557 [19] P. W. Higgs, “Broken symmetries and the masses of gauge bosons,” *Phys. Rev. Lett.*,
1558 vol. 13, pp. 508–509, Oct 1964.
- 1559 [20] G. S. Guralnik, C. R. Hagen, and T. W. B. Kibble, “Global conservation laws and
1560 massless particles,” *Phys. Rev. Lett.*, vol. 13, pp. 585–587, Nov 1964.
- 1561 [21] S. Weinberg, “A model of leptons,” *Phys. Rev. Lett.*, vol. 19, pp. 1264–1266, Nov
1562 1967.
- 1563 [22] H. Yukawa, “On the interaction of elementary particles. i,” *Progress of Theoretical
1564 Physics Supplement*, vol. 1, pp. 1–10, 1955.
- 1565 [23] Y. e. a. Fukuda, “Evidence for oscillation of atmospheric neutrinos,” *Phys. Rev.
1566 Lett.*, vol. 81, pp. 1562–1567, Aug 1998.
- 1567 [24] R. Becker-Szendy, C. Bratton, D. Casper, S. Dye, W. Gajewski, *et al.*, “A Search
1568 for muon-neutrino oscillations with the IMB detector,” *Phys.Rev.Lett.*, vol. 69,

- 1569 pp. 1010–1013, 1992.
- 1570 [25] S. P. Martin, “A Supersymmetry primer,” 1997.
- 1571 [26] H. Nilles, *Supersymmetry, Supergravity and Particle Physics*. Physics reports, North-Holland Physics Publ., 1984.
- 1573 [27] H. E. Haber and G. L. Kane, “The Search for Supersymmetry: Probing Physics
1574 Beyond the Standard Model,” *Phys.Rept.*, vol. 117, pp. 75–263, 1985.
- 1575 [28] E. Witten, “Dynamical Breaking of Supersymmetry,” *Nucl.Phys.*, vol. B188, p. 513,
1576 1981.
- 1577 [29] J. Wess and B. Zumino, “Supergauge transformations in four dimensions,” *Nuclear
1578 Physics B*, vol. 70, no. 1, pp. 39 – 50, 1974.
- 1579 [30] H. Muller-Kirsten and A. Wiedemann, *Introduction to Supersymmetry*. World
1580 Scientific lecture notes in physics, World Scientific, 2010.
- 1581 [31] I. Aitchison, *Supersymmetry in Particle Physics: An Elementary Introduction*.
1582 Cambridge University Press, 2007.
- 1583 [32] K. A. Intriligator and N. Seiberg, “Lectures on Supersymmetry Breaking,”
1584 *Class.Quant.Grav.*, vol. 24, pp. S741–S772, 2007.
- 1585 [33] Y. Shadmi, “Supersymmetry breaking,” pp. 147–180, 2006.
- 1586 [34] C. Burgess, P. G. Camara, S. de Alwis, S. Giddings, A. Maharana, *et al.*, “Warped
1587 Supersymmetry Breaking,” *JHEP*, vol. 0804, p. 053, 2008.
- 1588 [35] H. Murayama, “Supersymmetry breaking made easy, viable, and generic,” 2007.
- 1589 [36] H. Baer and X. Tata, *Weak Scale Supersymmetry: From Superfields to Scattering
1590 Events*. Cambridge University Press, 2006.
- 1591 [37] S. P. Martin, “Implications of supersymmetric models with natural r-parity conser-
1592 vation,” 1996.
- 1593 [38] G. L. Kane, C. F. Kolda, L. Roszkowski, and J. D. Wells, “Study of constrained
1594 minimal supersymmetry,” *Phys.Rev.*, vol. D49, pp. 6173–6210, 1994.
- 1595 [39] C. Stlege, G. Bertone, D. Cerdeno, M. Fornasa, R. Ruiz de Austri, *et al.*, “Updated
1596 global fits of the cmSSM including the latest LHC SUSY and Higgs searches and
1597 XENON100 data,” *JCAP*, vol. 1203, p. 030, 2012.

- 1598 [40] M. Citron, J. Ellis, F. Luo, J. Marrouche, K. Olive, *et al.*, “The End of the CMSSM
1599 Coannihilation Strip is Nigh,” *Phys.Rev.*, vol. D87, p. 036012, 2013.
- 1600 [41] D. Ghosh, M. Guchait, S. Raychaudhuri, and D. Sengupta, “How Constrained is
1601 the cMSSM?,” *Phys.Rev.*, vol. D86, p. 055007, 2012.
- 1602 [42] D. Alves *et al.*, “Simplified Models for LHC New Physics Searches,” *J.Phys.*, vol. G39,
1603 p. 105005, 2012.
- 1604 [43] J. Alwall, P. Schuster, and N. Toro, “Simplified Models for a First Characterization
1605 of New Physics at the LHC,” *Phys.Rev.*, vol. D79, p. 075020, 2009.
- 1606 [44] S. Chatrchyan *et al.*, “Interpretation of Searches for Supersymmetry with simplified
1607 Models,” *Phys.Rev.*, vol. D88, p. 052017, 2013.
- 1608 [45] J. Hisano, K. Kurosawa, and Y. Nomura, “Natural effective supersymmetry,”
1609 *Nucl.Phys.*, vol. B584, pp. 3–45, 2000.
- 1610 [46] M. Papucci, J. T. Ruderman, and A. Weiler, “Natural SUSY Endures,” *JHEP*,
1611 vol. 1209, p. 035, 2012.
- 1612 [47] B. Allanach and B. Gripaios, “Hide and Seek With Natural Supersymmetry at the
1613 LHC,” *JHEP*, vol. 1205, p. 062, 2012.
- 1614 [48] K. Aamodt *et al.*, “The ALICE experiment at the CERN LHC,” *JINST*, vol. 3,
1615 p. S08002, 2008.
- 1616 [49] G. Aad *et al.*, “The ATLAS Experiment at the CERN Large Hadron Collider,”
1617 *JINST*, vol. 3, 2008.
- 1618 [50] R. Adolphi *et al.*, “The cms experiment at the cern lhc,” *JINST*, vol. 0803, p. S08004,
1619 2008.
- 1620 [51] A. A. Alves *et al.*, “The LHCb Detector at the LHC,” *JINST*, vol. 3, p. S08005,
1621 2008.
- 1622 [52] J.-L. Caron, “Lhc layout.. schema general du lhc..” Sep 1997.
- 1623 [53] C. Collaboration, “Cms luminosity - public results.”
1624 twiki.cern.ch/twiki/bin/view/CMSPublic/LumiPublicResults., 2011.
- 1625 [54] CERN, “Cms compact muon solenoid..” <http://public.web.cern.ch/public/Objects/LHC/CMSnc.jpg>
1626 Feb 2010.

- 1627 [55] *The CMS electromagnetic calorimeter project: Technical Design Report*. Technical
1628 Design Report CMS, Geneva: CERN, 1997.
- 1629 [56] *The CMS muon project: Technical Design Report*. Technical Design Report CMS,
1630 Geneva: CERN, 1997.
- 1631 [57] CMS Collaboration, “The cms physics technical design report, volume 1,”
1632 *CERN/LHCC*, vol. 2006-001, 2006.
- 1633 [58] M. Cacciari, G. P. Salam, and G. Soyez, “The anti- k_t jet clustering algorithm,”
1634 *Journal of High Energy Physics*, vol. 2008, no. 04, p. 063, 2008.
- 1635 [59] “Jet performance in pp collisions at 7 tev,” Tech. Rep. CMS-PAS-JME-10-003,
1636 CERN, Geneva, 2010.
- 1637 [60] X. Janssen, “Underlying event and jet reconstruction in cms,” Tech. Rep. CMS-CR-
1638 2011-012, CERN, Geneva, Jan 2011.
- 1639 [61] T. C. collaboration, “Determination of jet energy calibration and transverse mo-
1640 mentum resolution in cms,” *Journal of Instrumentation*, vol. 6, no. 11, p. P11002,
1641 2011.
- 1642 [62] R. Eusebi and on behalf of the CMS collaboration), “Jet energy corrections and
1643 uncertainties in cms: reducing their impact on physics measurements,” *Journal of
1644 Physics: Conference Series*, vol. 404, no. 1, p. 012014, 2012.
- 1645 [63] “Algorithms for b Jet identification in CMS,” Tech. Rep. CMS-PAS-BTV-09-001,
1646 CERN, 2009. Geneva, Jul 2009.
- 1647 [64] “Performance of b tagging at $\sqrt{s}=8$ tev in multijet, ttbar and boosted topology
1648 events,” no. CMS-PAS-BTV-13-001, 2013.
- 1649 [65] T. C. collaboration, “Identification of b-quark jets with the cms experiment,” *Journal
1650 of Instrumentation*, vol. 8, no. 04, p. P04013, 2013.
- 1651 [66] S. Dasu *et al.*, “CMS. The TriDAS project. Technical design report, vol. 1: The
1652 trigger systems,” 2000.
- 1653 [67] P. Sphicas, “CMS: The TriDAS project. Technical design report, Vol. 2: Data
1654 acquisition and high-level trigger,” 2002.
- 1655 [68] J. B. et al., “Calibration and Performance of the Jets and Energy Sums in the
1656 Level-1 Trigger ,” no. CMS IN 2013/006 (2013), 2013.

- 1657 [69] B. et al., “Study of Level-1 Trigger Jet Performance in High Pile-up Running
1658 Conditions,” no. CMS IN 2013/007 (2013), 2013.
- 1659 [70] J. J. Brooke, “Performance of the cms level-1 trigger,” Tech. Rep. CMS-CR-2012-322.
1660 CERN-CMS-CR-2012-322, CERN, Geneva, Nov 2012.
- 1661 [71] L. Randall and D. Tucker-Smith, “Dijet searches for supersymmetry at the large
1662 hadron collider,” *Phys. Rev. Lett.*, vol. 101, p. 221803, Nov 2008.
- 1663 [72] “SUSY searches with dijet events,” 2008.
- 1664 [73] “Search strategy for exclusive multi-jet events from supersymmetry at CMS,” Tech.
1665 Rep. CMS-PAS-SUS-09-001, CERN, 2009. Geneva, Jul 2009.
- 1666 [74] “Calorimeter Jet Quality Criteria for the First CMS Collision Data,” Tech. Rep.
1667 CMS-PAS-JME-09-008, CERN, 2010. Geneva, Apr 2010.
- 1668 [75] T. C. collaboration, “Performance of cms muon reconstruction in pp collision events
1669 at $\sqrt{s} = 7$ tev,” *Journal of Instrumentation*, vol. 7, no. 10, p. P10002, 2012.
- 1670 [76] “Search for supersymmetry in events with photons and missing energy,” Tech. Rep.
1671 CMS-PAS-SUS-12-018, CERN, Geneva, 2012.
- 1672 [77] M. Cacciari and G. P. Salam, “Pileup subtraction using jet areas,” *Phys.Lett.*,
1673 vol. B659, pp. 119–126, 2008.
- 1674 [78] Z. Bern, G. Diana, L. J. Dixon, F. Febres Cordero, S. Hoche, H. Ita, D. A. Kosower,
1675 D. Maitre, and K. J. Ozeren, “Driving missing data at next-to-leading order,” *Phys.
1676 Rev. D*, vol. 84, p. 114002, Dec 2011.
- 1677 [79] “Data-Driven Estimation of the Invisible Z Background to the SUSY MET Plus
1678 Jets Search,” Tech. Rep. CMS-PAS-SUS-08-002, CERN, 2009. Geneva, Jan 2009.